Sedimentary analysis of the deep-water (Pliocene) Pellini Member,

Corinth Rift, Greece

Thesis of Master degree in sedimentology/Petroleum Geology

Marthe Førland

Department of Earth Science

University of Bergen

2016

ABSTRACT

This sedimentological study focuses on the architectural elements distinguished within the deep-water Pellini Member. The Pellini Member is located south of the active Corinth rift, within the uplifted and incised Pliocene-Pleistocene rift basin of the northern Peloponnese Peninsula, Greece. This syn-rift succession is exposed in a small area along the western side of the northeast oriented Sythas valley, 7 km south of the Xylocastro village. The coarse-grained Pellini member belongs to the turbiditic/hemipelagic Rethio-Dendro Formation, Lower Group. The northeast dipping Amphithea fault separates the Pellini Member from the relatively younger parts of the Rethio-Dendro Formation.

The identification of the palaeoenvironmental and palaeogeographic depositional setting, and mechanisms controlling the evolution of the Pellini Member was achieved by integrating traditional fieldwork techniques with LiDAR-based digital outcrop modelling, combined with literary research. This combination allowed the identification of 11 architectural elements, distinguished as channelized and non-channelized elements. Channelized elements are described as Large-scale complex sheets (AE1), Large-scale complex ribbons (AE2), Large-scale complex U-shaped elements (AE3), Large-scale simple ribbons (AE4), Small-scale simple U-shaped elements (AE5), Small-scale simple ribbons, (AE6), and Small-scale simple ribbon-sheets (AE7). Non-channelized elements are described as Deformed large-scale complex sheets (AE8), Thin-to thick-bedded sandstone sheets (AE9), Sandy heterolithics (AE10), and Mudstone with thin-bedded sandstone sheets (AE11). These architectural elements represent meandering (AE1, 2 and 4), non-meandering (AE3), and crevassing channels and splays (AE5, 6, and 7), alternating with interchannel deposits (AE8, 9, 10, and 11).

The orientation, geometry and stratigraphic distribution of the large- and small-scale channelized elements, points towards a branched channel system. This system is dominated by sinuous distributives and crevassing channels, alternating with interchannel deposits. Multi-storey channels comprise vertically and/or laterally stacked channel bodies which indicate their planform development to have been controlled by the degree of aggradation, avulsion and lateral confinement. Laterally stacked channels indicate modest lateral confinement and a relatively low rate of overbank aggradation. Vertically stacked channels reflect lateral confinement and/or high rates of sediment aggradation. Meandering single-storey channels are unilateral, indicating a low degree of lateral confinement, combined with relatively low rates of aggradation. Crevassing channels and splays exhibits the highest variations in planform geometry; rapidly changing in thickness and width in the transition from being confined to unconfined. The sedimentary system reflects relatively high rates of sediment aggradation overall, combined with high rates of channel avulsion and bifurcation, which are the main processes controlling the channels' planform development and the creation of thickening and thinning upwards sandstone sheets. High rates of aggradation are caused by the high frequency of coarse-grained turbidity flows, which is the main transport mechanism of sediments to the deep-water fan-channel system. Despite the significant degree of overbank sedimentation, no levees are recognized within the study area. The Pellini channels record an average southeast transport direction, which combined with the relatively coarse-grained interior, suggest the Pellini Member to have been sourced from the west by the Killini fan delta. This is also supported by the Pellini Members clast composition, which is similar to the those recorded within the Gilbert-type delta. The stratigraphic upwards relocation of the palaeocurrent transport direction, suggests the northeast dipping Amphiathea fault to have been active, causing the overall transport direction to change from east to south. The Pliocene-Pleistocene rift configuration suggests tectonic activity to be the main control mechanism during the deposition of the Pellini member.

ACKNOWLEDGEMENT

This thesis is part of a master`s degree in Petroleum Geoscience at the Department of Earth Science at the University of Bergen and is a result of several contributors. First I will like to thank my main supervisor Prof. Rob Gawthorpe for selecting out such a highly interesting study area. I am thankful for all the guidance and feedback throughout this project. A special thanks to my co-supervisor Martin Muravchik for guidance, helpful discussions both during and after field work in Greece, computer support and literary feedback. Tullow and VNG for economical support, making it possible to carry out the field work. I would also like to thank Emmanuel Skourtsos and Haralambos Kranis for helpful discussions and guidance during field work.

Special thanks need to be directed to Stine Hemnes Sletten and Sturla Vatne Meling for helpful discussions and support during and after field. Karen Tellefsen, Tor Helge Storstein, Gijs Allard Henstra, Christian Haug Eide, Vilde Dimmen, and Maria Ordemann Erichsen for constructive reviews. Sebastian Wolf and Kristoffer Igland for aiding me in MATLAB, Øystein Spinnangr for helping me in Microsoft Excel and Synne Skaar Ågotnes for aiding me in Microsoft Word.

I would also like to express my gratitude to the one and only, Prof. Wojciech Nemec. His passion for geology is deeply inspiring and has encouraged me throughout the master studies. Thank you for always answering my questions and for providing me with invaluable and generous help.

Last, but not least, I would like to thank my field assistant Olav Aleksander Naurstad for being an excellent companion in Greece, for learning me Adobe Illustrator and for constantly encouraging me throughout this project. Thank you for always cheering me up.

Marthe Førland

Marthe Førland

Bergen, August 2016

CONTENT

1. INTRODUCTION

1.1 Background and rationale

The Gulf of Corinth is located between the northern Peloponnese Peninsula and mainland Greece, defined as a N-S extensional strain-band, interpreted to have initiated during Early Pliocene times (Doutsos and Piper, 1990; Billiris *et al.*, 1991; Collier and Dart, 1991; Armijo *et al.*, 1996). As such, the Gulf of Corinth comprise some of the most accessible and youngest examples of active continental rifting on Earth, providing excellent exposures for the study of tectono-stratigraphic relations and processes related to intracontinental rifting. Extensive research both on the onshore (*e.g*. Ori, 1989; Collier and Dart, 1991; Poulimenos *et al.*, 1993; Dart *et al.*, 1994; Ford *et al.*, 2007; Rohais *et al.*, 2007a; Rohais *et al.*, 2007b; Rohais *et al.*, 2008; Leeder *et al.*, 2012; Ford *et al.*, 2013) and offshore (Moretti *et al.*, 2003; McNeill *et al.*, 2005; Bell *et al.*, 2008; Bell *et al.*, 2009; Taylor *et al.*, 2011) has been conducted during the last decades which has provided a broad understanding of the various structural and stratigraphic components comprising the Corinth rift system.

From oldest to youngest, the syn-rift stratigraphy is separated into the Lower, Middle and Upper Group (Rohais *et al.*, 2007a). These syn-sedimentary successions provide information regarding external controlling factors such as tectonics, climate, sediment supply, accommodation space, antecedent drainage pathways and bedrock lithology (*e.g.* Gawthorpe and Colella, 1990; Leeder and Jackson, 1993; Gawthorpe *et al.*, 1994; Cowie *et al.*, 2000; Gawthorpe and Leeder, 2000; Rohais *et al.*, 2007a; Ford *et al.*, 2013). They also display the relative chronology of fault activity in the region; elucidating timing and duration of the geodynamic development that has affected the region since Miocene times (*e.g.* Billiris *et al.*, 1991; Jolivet *et al.*, 1994; Armijo *et al.*, 1999; Rohais *et al.*, 2007a; Taylor *et al.*, 2011; Ford *et al.*, 2013). Most of the onshore studies concerning the syn-rift stratigraphy have been related to the uplifted and deeply incised central and western part of the northern Peloponnese Peninsula (*e.g.* Doutsos *et al.*, 1988; Ori, 1989; Flotté *et al.*, 2005; Ford *et al.*, 2007; Rohais *et al.*, 2007a; Rohais *et al.*, 2007b; Ford *et al.*, 2013), however, relatively little is known regarding the present inactive, east-central part of the onshore Corinth rift (Leeder *et al.*, 2012).

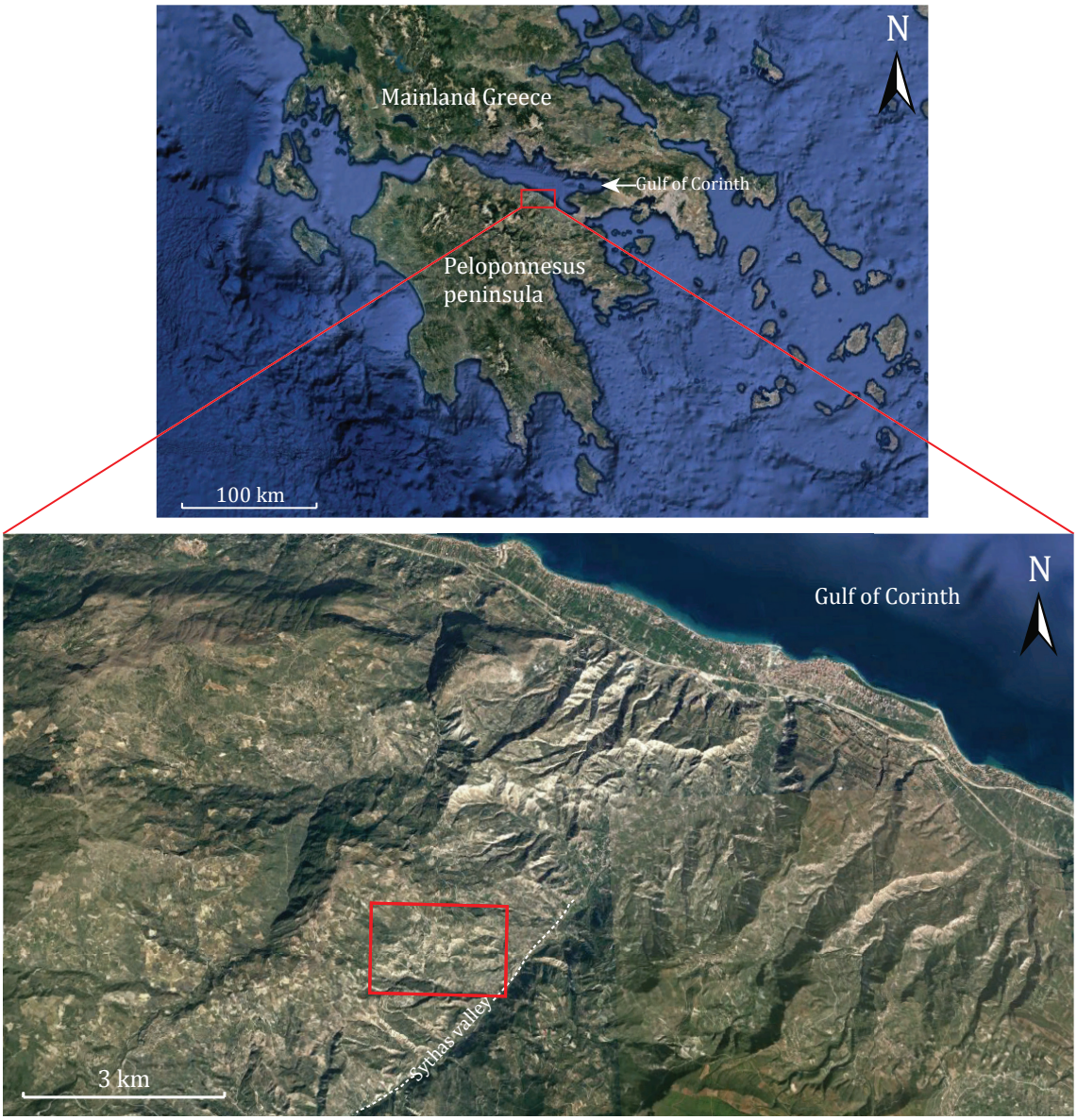

Figure 1.1: Location of the study area in central Peloponnese Peninsula, indicated by red boxes. Modified from Google Earth.

The coarse-grained Pellini Member belongs to the Pliocene-Pleistocene Rethio-Dendro Formation (Koutsouveli *et al.*, 1989; Leeder *et al.*, 2012) of the Lower Group, exposed along the southern coast of the Gulf of Corinth (Figure 1.1). The Pellini Member is interpreted as one of the oldest units found within the turbiditic/hemipelagic Rethio-Dendro Formation (*sensu* Koutsouveli *et al.*, 1989), which is a deep-water depositional system sourced by major Gilbert-type deltas (Leeder *et al.*, 2012).

A process that could explain the occurrence of coarse-grained sediments in distal deep-water environments was first described by Johnson (1938). Turbidity currents concerns the main transport mechanism of sediments (i.e. turbidites) to deep-water depositional systems, however, due to their remote and unpredictable occurrences these processes are difficult to monitor within a deep-water setting. This makes the study of outcrop analogues important in order to understand the various transportation and depositional properties creating architectural elements which form the building blocks within deep-water systems. Ancient deep-water channel-fan systems have been extensively studied by various authors during the past decades (*e.g.* Walker, 1975; Mutti and Normark, 1987; Mutti *et al.*, 1999; Wynn *et al.*, 2002; Abreu *et al.*, 2003; Lien *et al.*, 2003; Janbu *et al.*, 2007; Kane *et al.*, 2009; Di Celma *et al.*, 2010; Jobe *et al.*, 2010; Di Celma, 2011; Janocko *et al.*, 2011; Kane and Hodgson, 2011; Macdonald *et al.*, 2011; McHargue *et al.*, 2011; Grundvåg *et al.*, 2014). This has lead to a greater understanding in regards to the dynamic nature of deep-water sedimentation in response to various control mechanisms such as tectonics, climate, eustatic sea level changes and hinterland geology (Stow *et al.*, 1985; Bouma, 2004).

The focus of this study is to perform a detailed sedimentological analysis of the architectural elements found within the syn-rift Pellini Member. This was achieved by traditional sedimentological research and digital outcrop analysis. Terrestrial LiDAR scanning is a relatively new field-data collecting technique which enables close inspection of otherwise inaccessible terrain. Rock body geometries could easily be traced and measured with a high degree of spatial accuracy after processing. Based on the combination of these approaches eleven architectural elements are distinguished, divided into channelized and non-channelized elements. Channelized elements are either isolated or stacked, whereby the latter is referred to as channel complexes. Channelized elements are broadly sinuous in origin, encased in non-channelized units, referred to as interchannel deposits. The majority of these architectural elements are coarse-grained, known to be of good reservoir quality in hydrocarbon rich basins and are a key exploration target for the petroleum industry.

1.2 Aims and objectives

The principal aim of this study is to identify the palaeoenvironmental and palaeogeographic depositional setting and mechanisms controlling the evolution of the Pellini Member. This was achieved by integrating terrestrial fieldwork techniques and LiDAR-based digital outcrop data, combined with literary research. The specific objectives for this study are:

i. Create a field-based facies analysis of the Pellini Member deposits.
ii. Differentiate between various architectural elements.
iii. Perform an analysis focusing on the channels' orientation, dimension and spatial distribution within the study area.

1.3 Previous work

Little geological research has been conducted on the deep- water Pellini Member, compared to the western laterally adjacent and overlying alluvial, deltaic and shallow to deep-water counterparts of the Lower, Middle and Upper Group (Ford *et al.*, 2007; Rohais *et al.*, 2007a; Rohais *et al.*, 2007b; Rohais *et al.*, 2008; Leeder *et al.*, 2012; Ford *et al.*, 2013; Gobo *et al.*, 2014a; Gobo *et al.*, 2014b; Gobo *et al.*, 2015).

Ori (1989) was the first to propose a three-fold initial division of the syn-rift stratigraphy along the south western margin of the Gulf of Corinth. This division has later been revised and is now known as the (I) Lower, (II) Middle and (III) Upper Group(*e.g.* Ghisetti and Vezzani, 2005; Rohais *et al.*, 2007a; Rohais *et al.*, 2007b; Rohais *et al.*, 2008; Backert *et al.*, 2010; Ford *et al.*, 2013).

2 REGIONAL GEOLOGICAL SETTING

2.1 Introduction

The actively subsiding Gulf of Corinth is a 115 km long and 30 km wide asymmetric basin (Figure 2.1B), bounded by active faults which constitutes one of the Earths most rapidly extending new plate boundary *(e.g.* Ford *et al.*, 2013). The present day N-S extension rates range from 4 mm/yr in the east to 11-16 mm/yr in the central and western region (*e.g.* Billiris *et al.*, 1991; Briole *et al.*, 2000; McClusky *et al.*, 2000; Stefatos *et al.*, 2002; Moretti *et al.*, 2003; Bernard *et al.*, 2006).

The northern part of the Peloponnese Peninsula comprises rotated and elevated fault blocks, uplifted at a rate of 1 to 1.5 mm/yr, with a higher rate of uplift in the west, gradually decreasing towards the east (*e.g.* Billiris *et al.*, 1991; Dart *et al.*, 1994; Davies *et al.*, 1997; Briole *et al.*, 2000; McNeill and Collier, 2004; Rohais *et al.*, 2007a). Uplift and rotation of fault blocks, combined with subsequent northward directed fluvial incision, have resulted in deeply incised NNE to SSW trending valleys, which provide a greater insight of the syn-rift stratigraphy and structural geology (Backert *et al.*, 2010). This region is thus considered a natural laboratory where early rift history can be studied, in particular the effects of sedimentary and geomorphological processes.

2.2 Regional tectonic setting of the Gulf of Corinth

The Gulf of Corinth is situated within the Aegean region (Figure 2.1A), which is interacting with the Eurasian, African, and Arabian plates, and Anatolian microplate. This configuration has resulted in various tectonic processes such as extensional deformation, subduction and strike-slip faulting (*e.g.* McKenzie, 1972; McKenzie, 1978; Dewey and Şengôr, 1979; Le Pichon and Angelier, 1979). Extensional deformation occurs between the Aegean and Anatolian microplates in western Turkey, and within central Greece (Le Pichon and Angelier, 1979; Armijo *et al.*, 1996). Subduction occurs within the Hellenic arc and trench system as a result of the African plate being subducted beneath the Aegean microplate (McKenzie, 1970; Jackson and McKenzie, 1984, 1988). Strike-slip faulting is

established along the dextral North Anatolian fault and the sinistral East Anatolian, and Dead Sea faults (Armijo *et al.*, 1996; Armijo *et al.*, 1999).

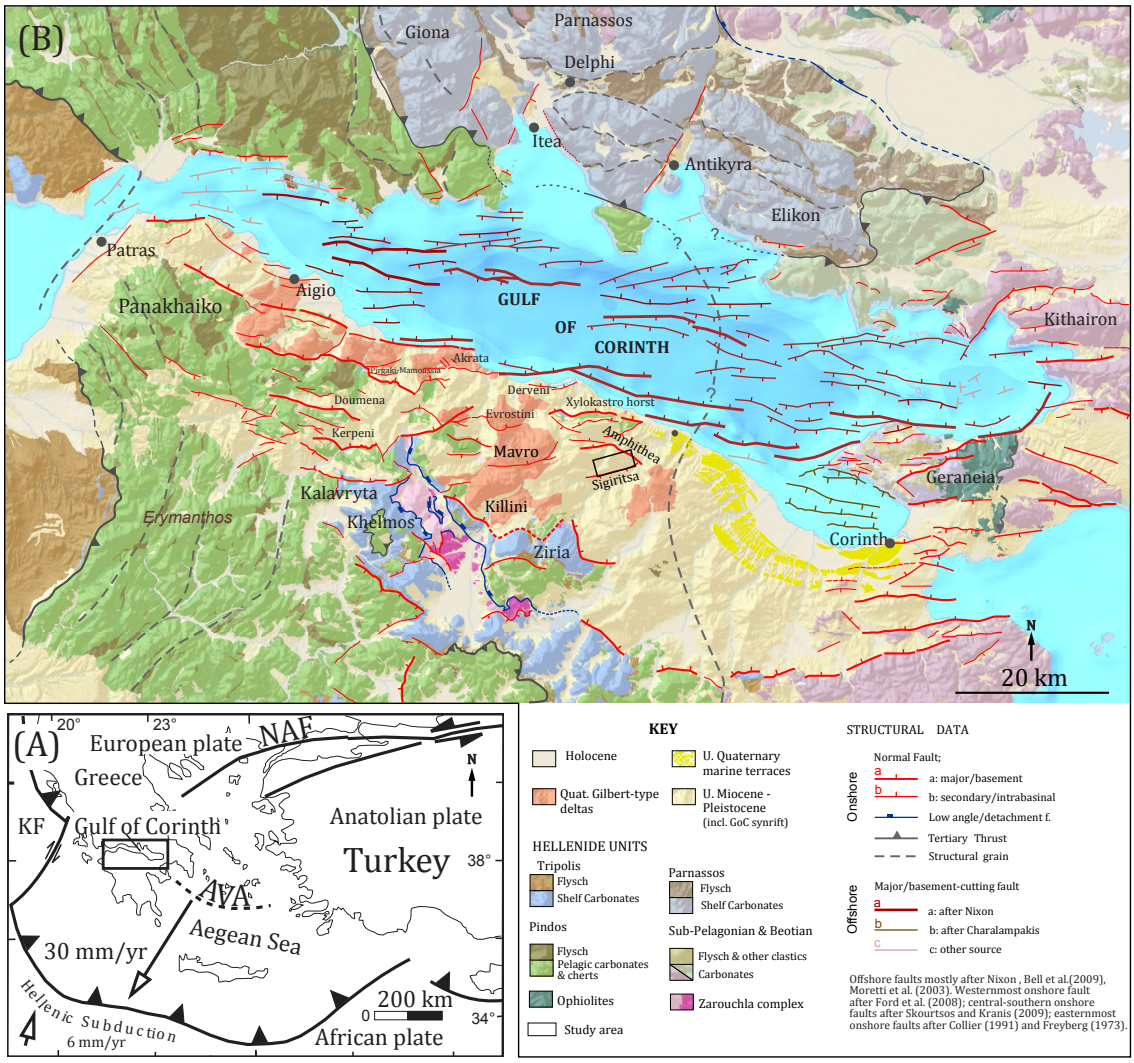

*Figure 2.1: Tectonic map of the Aegean region (**A**) and the Corinth rift (**B**). NAF = The North Anatolian Fault system, KF= The Kefalonial Fault, AVA = The Aegean volcanic arc. **A** modified from Ford et al. (2013), **B** modified from Kranis et al. (2015).*

Three main tectonic mechanisms are interpreted to be related to the initiation and ongoing rifting within the actively diverging central Greece: Back-arc extension, crustal thickening and subsequent gravitational collapse during the Hellenic Orogeny, and the transform north Anatolian fault system (*e.g.* Rohais *et al.*, 2007a; Bell *et al.*, 2008; Ford *et al.*, 2013). The present Aegean back-arc extension initiated during Late Eocene/Early Oligocene (Jolivet *et al.*, 2013). This is argued to have been caused by rollback of the

African slab (Le Pichon and Angelier, 1979; Jolivet and Faccenna, 2000), combined with the gravitational collapse of the thickened lithosphere in the Hellenide orogeny (McKenzie, 1972, 1978; Le Pichon and Angelier, 1979; Doutsos *et al.*, 1988; Jolivet *et al.*, 1994; Armijo *et al.*, 1996; Jolivet, 2001). An additional driving force is the westward propagation the North Anatolian Fault, which initiated during Miocene times, due to the collision between Arabia and Eurasia (Dewey and Şengôr, 1979). This transverse fault system splays into a northern and southern branch, whereby the southern branch affects the motion of the Aegean microplate (Armijo *et al.*, 1996; Armijo *et al.*, 1999).

2.3 Structural background

The Gulf of Corinth is a WNW-ESE striking asymmetric half-graben basin which stretches from the western Rion Straits to the eastern Alkyonides Gulf, and the Corinth Canal (Figure 2.1; *e.g.* McKenzie, 1972, 1978; Armijo *et al.*, 1996; Ford *et al.*, 2013). Major active faults with displacements exceeding 500 m exist in the offshore part of the Corinth rift. These faults have a general E-W to WNW-ESE orientation comprising a segmentation length ranging between 15 and 25 km (Figure 2.1B; Bell *et al.*, 2008). The Gulf of Corinth is bounded to the north by south dipping normal faults, whereas the southern coast is dominated by north dipping normal fault blocks segmented along strike, filled by Pliocene-Quaternary syn-rift deposits (*e.g.* Ori, 1989; Armijo *et al.*, 1996; Moretti *et al.*, 2003; Ford *et al.*, 2013).

The northern coast of the Peloponnese Peninsula is divided into series of tilted fault blocks which are spaced every 5 to 8 km (Rohais *et al.*, 2007a). These fault blocks are separated into three principal north dipping fault segments. From west to east these segments are known as the Aigion, Xylocastro and South Alkyonides faults (Figure 2.1B; *e.g.* Duffy *et al.*, 2015). Tilted fault blocks exhibit a maximum displacement of 300 m, creating a 20 km wide stepped terrain from the inland Peloponnese to the coast (Figure 2.1B). The southern fault blocks are the widest, progressively narrowing towards the north (*e.g.* Rohais *et al.*, 2007a; Skourtsos and Kranis, 2009).

2.4 Stratigraphic background

The stratigraphy of the Northern Peloponnese Peninsula consist of Mesozoic pre-rift units and a Pliocene to present day syn-rift succession. The pre-and syn-rift successions are separated by an unconformity representing approximately 15 to 20 Myr (*e.g*. Ford *et al.*, 2013). These successions are internally separated into three tectonostratigraphical groups described in the following sections.

2.4.1 Pre-rift stratigraphy

Pre-rift Corinth was dominated by a well established drainage network among the mountainous topography of the N-S oriented Hellenide orogeny (Ford *et al.*, 2013). From Cretaceous to Miocene times, allochtonous units were progressively emplaced towards the W-WSW during the Alpine Orogeny. These units are known as the Hellenide thrust sheets, mainly composed of deposits from the Mesozoic Era *(e.g*. Doutsos *et al.,* 1993; Trotet *et al*., 2006; Rohais *et al*., 2007a; Ford *et al*., 2013). The stacked pre-rift accretions are separated into the Zarouchla, Gavrovo-Tripolitza and Pindos thrust sheet units *(e.g.* Rohais et al., 2007a; Ford et al., 2013; *and references therein*). The basal Alpine Zarouchla complex, is a 1.5 to 2 km thick unit constituting high pressure-low temperature metamorphosed phyllites, schist, and quartzites (Trotet *et al.*, 2006). The 2 to 3 km thick Gavrovo-Tripolitza nappe, overlays the Zarouchla complex and is composed of Mesozoic carbonates. The upper Pindos unit comprises a series of highly deformed and imbricated thrust sheets, overlaying the Gavrovo-Tripolitza carbonate platform. The 1 km thick Pindos unit is composed of Upper Triassic-Jurassic pelagic limestone, intercalated with minor red and green radiolarites and sicilic micrites and Upper Cretaceous to Tertiary lacustrine turbidites (Degnan and Robertson, 1998; Skourlis and Doutsos, 2003; Trotet *et al.*, 2006).

2.4.2 Onshore Syn-rift stratigraphy

Whereas the mountainous northern coast comprises little or no syn-rift sediments, the southern region exhibits a well preserved syn-rift succession that have been uplifted and subsequently incised by north flowing rivers (Rohais *et al.*, 2007a; Ford *et al.*, 2013). The local stratigraphic thickness of the syn-rift succession varies across a series of E-W trending normal fault blocks, and can locally reach thicknesses of up to 2800 m (Rohais

et al., 2007a). From the oldest to the youngest the syn-rift succession is divided into the Lower, Middle, and Upper Group (Figure. 2.2).

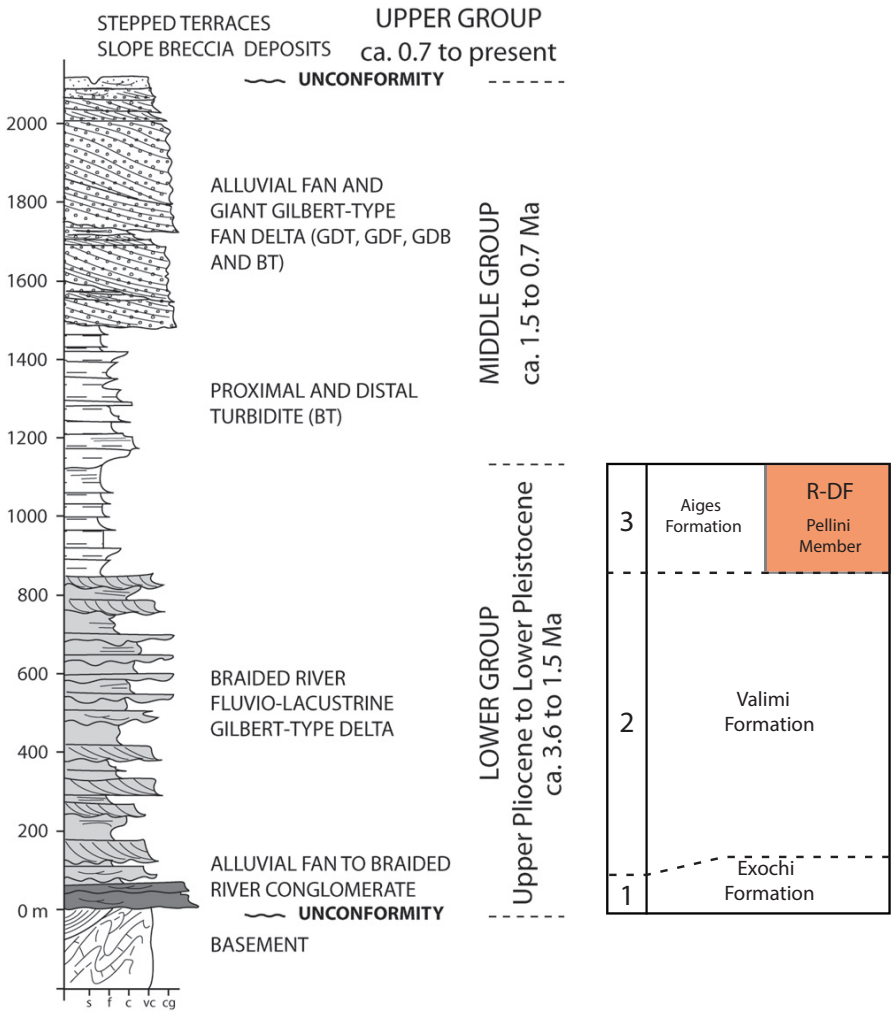

Figure 2.2: Composite stratigraphic section from the Derveni to Evrostini area (see location in Figure 2.1). In red: Rethio-Dendro Formation (R-DF) and the Pellini Member. Modified from Rohais et al. (2007a); Rohais et al. (2008).

I) The Lower Group

The earliest known syn-rift sediments belong to the onshore Lower Group and are estimated to be around 3.6 to 4 Ma (*e.g.* Collier and Dart, 1991; Rohais *et al.*, 2007a). The Lower Group represents a broad spectrum of facies deposited in terrestrial to deep-water settings that record the initial stage of rifting from Lower to Upper Pleistocene, *ca.* 5 to 1.8 Ma (*e.g*. Ford *et al.*, 2013). This Group lies unconformably over karstified limestone of the Pindos unit. The lowermost Exochi Formation consists of coarse-grained alluvial fan

deposits (Figure 2.2), overlain by the Valimi Formation comprising fluvial to shallow lacustrine sandstone and conglomerate (Figure 2.2; Rohais *et al.* 2007a). The uppermost Aiges Formation represent deep-water deposits of interbedded fine- to coarse-grained sandstone with shaly-siltstone and marlstone, interpreted as turbidite deposits within a distal fan system (Rohais *et al.*, 2007a). The lower part of the Aiges Formation is interpreted to correspond to the distal equivalents of the Valimi Formation, whereas the upper part is interpreted to be the prodelta deposits of large-scale Gilbert-type deltas (Rohais *et al.*, 2007a; Rohais *et al.*, 2008; Leeder *et al.*, 2012). The Aiges Formation is laterally equivalent to the Rethio-Dendro Formation (R-DF) which constitutes deep-water, fine- to coarse-grained deposits sourced from the west by the Killini and/or Mavro fan-deltas (Leeder *et al.*, 2012). The Pellini Member of the Lower Rethio-Dendro Formation is the focus of this study. It is only exposed in a small locality in the Sythas valley, separated from the upper part of Rethio-Dendro Formation by the NE dipping Amphithea fault. The Pellini Member is located in the north-central part of the Peloponnese Peninsula, 7 km south of the village of Xylokastro (Figure 1.1).

The Lower Group is exposed from the present-day shoreline to 20 km south of the northwestern part of the Peloponnese Peninsula (Ford *et al.*, 2013). The progressive north and eastward fining of the deposits was interpreted to indicate a north-northeast to northeast palaeotransport direction (Ford *et al.*, 2013). In the northeastern region, deep-water deposits are more prominent than the alluvial plain deposits which are more prominent in the west (*e.g*. Ford *et al.*, 2013).

II) Middle Group

The Early to Middle Pleistocene Middle Group comprises alluvial fan systems in the south, to conglomeratic Gilbert-type fan deltas and deep-water turbidite systems in the north (Figures 2.2 and 2.3B; *e.g.* Rohais et al., 2007a). Large-scale Gilbert-type fan deltas are interpreted to prograde northwards into brackish and/or marine waters, supplying the deep-waters with fine-grained turbidites and hemipelagic sediments (*e.g*. Rohais *et al*., 2007a). The unconformity that separates the Middle Group from the Lower Group is interpreted to be a result of extensive erosion due to regional uplift events (*e.g*. Rohais et al., 2007a; Ford et al., 2013). The Gilbert-type fan deltas can have a total radius of up to 4 km, a thickness ranging from 400-1000 m, and delta forests inclined 28^{o} (Rohais *et al.*,

2007a; Ford *et al.*, 2013). The Killini and Mavro fan delta complexes are developed adjacent to the Killini and Mavro faults (Figure 2.1), and are interpreted as the main source areas for the Aiges and Rethio-Dendro Formation (Rohais *et al.*, 2007a; Leeder *et al.*, 2012). These large scale fan deltas differ in terms of their lithological clast composition, whereas Mavro fan delta conglomerates comprise clasts from the deeply eroded Phyllite-Quartzite pre-rift Zarouchla complex, which are absent in the older Killini fan delta (Rohais *et al.*, 2007a). This imply that the Middle group record erosion of the upper tectonic nappes, whereby progressive erosion is firstly recorded within the Mavro and the younger Everostini fan deltas (Rohais *et al.*, 2007a).

III) Upper Group

The Upper Group is mainly recorded within the offshore Gulf of Corinth comprising micritic limestone, and green and red radiolites, derived from the Pindos thrust sheet (Ford *et al.*, 2013). Onshore deposits are dominated by small Gilbert-type fan deltas (radii < 1 km), limestone notches and marine terraces that reflect progressive tectonic uplift along the southeastern coastline (*e.g.* Rohais *et al.,* 2007a; Bell *et al.*, 2008; *Ford et al.,* 2013).These deposits have been uplifted to altitudes of up to 500 m since 0.7 Ma to present day configuration (Ford *et al.*, 2013).

2.4.3 Offshore Syn-rift stratigraphy

The offshore syn-rift stratigraphy of the present-day Gulf of Corinth has an average thickness of 2200 m, with a maximum thickness of up to 2500 m in the central and eastern parts of the basin (Bell *et al.*, 2008; Taylor *et al.*, 2011) . The syn-rift succession are divided in two main units based on their seismic character (Moretti *et al.*, 2003; Bell *et al.*, 2009). These units are known as unit A and B and separated by an unconformity of *ca.* 0.4 to 0.5 Myr (Sachpazi *et al.*, 2003; Bell *et al.*, 2008; Bell *et al.*, 2009). Unit B comprises the oldest successions and is characterised as a non-reflective unit, equivalent to the onshore Gilbert-type deltas of the Middle Group (Figure 2.3B and C, defined in blue). Unit A exhibits continuous parallel reflections and is interpreted as equivalent to the onshore Upper Group (Figure 2.3 C, defined in pink). The uppermost strata within the present-day Gulf of Corinth are characterised by hemipelagic and gravity flow deposits sourced along the northern, southern and western margin (*e.g*. Ford et al., 2013). Fan deltas are

displayed along the southern margin, in contrast to the sediment starved northern margin (*e.g.* Bell, *et al*., 2008). The Gulf is surrounded by relatively steep-dipping flanks, which are prone to experience gravity flow processes due to sediment instability along over steep fan-delta foresets and seismic activity.

2.5 Structural and Stratigraphic evolution

The structural and stratigraphic evolution of the Corinth rift system has been divided into three main stages, separated by distinct episodes of extension rate acceleration, accompanied by northwards fault- and depocentre migration (Figure 2.3; Rohais *et al*., 2007a; Ford *et al*., 2013). The routing pathways have not only been affected by faulting, but also by well developed antecedent drainage pathways within the inherited relief of the Hellenic nappes (Ford *et al*., 2013).

Phase 1

The initial N-S extension started onshore (5 to 1.8 Ma), cross cutting the N-S oriented pre-rift substratum of the Hellenic orogeny (Figure. 2.3A). As such, the depositional pattern was controlled by the newly evolving normal fault system, combined with the well established pre-rift topography and antecedent drainage pathways (Ford *et al.*, 2013). The faulting was concomitant with high rates of sedimentation within alluvial fan to deep-water settings, supplied by antecedent north flowing rivers (Ford *et al.*, 2013). The sediment filled considerably high palaeo-reliefs, which suggests the sedimentation rate was higher than the rate of accommodation space creation (Ford et al., 2013). The Lower Group was deposited during a sea-level lowstand stage and progressive flooding during the subsequent transgressive stage (Rohais *et al*.,2007a). During a period of 0.3 Myr (*ca*. 1.8 to 1.5 Ma), a 15 km northward migration of fault and depocentres occurred along the southern margin, configuring a new, narrower and deeper basin (Ford *et al.*, 2013). Subsequent uplift and erosion created an unconformity, separating the Lower and Middle Group (Ford et al., 2013).

Phase 2

Extensional rates doubled *ca*. 1.5 to 0.5 Ma, however, this did not affect the aspect ratio and dimensions of the main fault system (Figure 2.3B). The southern faults were no longer active during this phase, and the faults and surrounding areas became uplifted. This resulted in high volumes of sediments being supplied and transported by transverse, north-flowing rivers (Ford *et al.*, 2013). The large-scale Gilbert-type fan deltas of the Middle Group were deposited along the southern rift margin, whereas deep-water sediments were deposited in the graben centre. Extension rate increased between 0.7 and 0.5 Ma, leading to a 5 km northward fault migration (Ford *et al*., 2013).

Phase 3

Phase 3 represents a further doubling of the extension rate with respect to Phase 2, combined with an increase in accommodation space in the eastern fault system (Figure 2.3C). Antecedent north flowing rivers in the west incised into rapidly uplifting coastal footwall blocks, experiencing rapid uplift, whereby small Gilbert-type deltas started to prograde across the newly created hangingwalls. Coastal terraces were formed in the eastern region. Eastern rivers were re-directed to flow south, forming endorheic basins (Ford *et al.*, 2013). Extension rate increased from Holocene to present day values (Ford *et al.*, 2013).

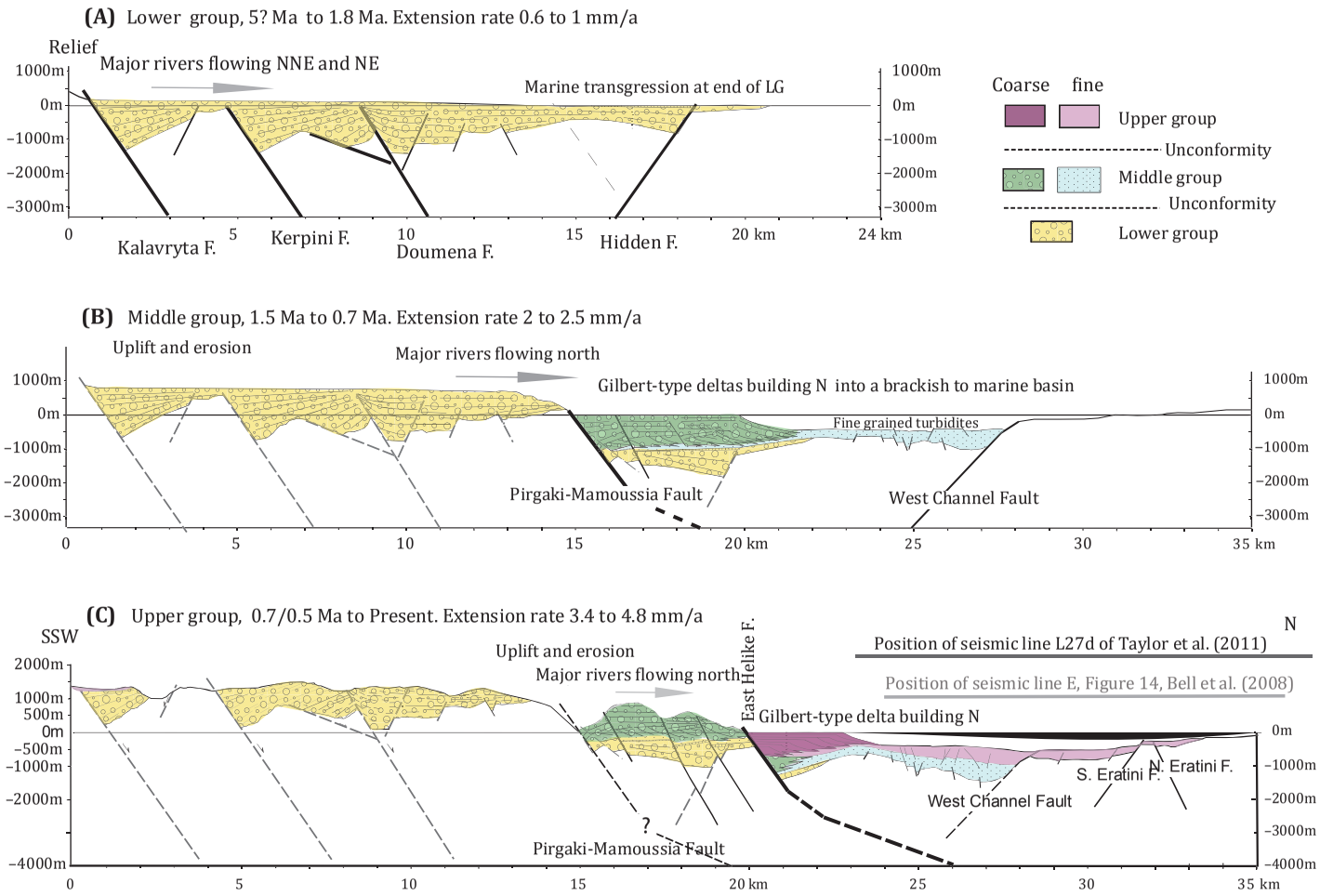

Figure 2.3: Cross-section of the northwestern part of the Peloponnese Peninsula into present day Gulf of Corinth from the Kalavryta Fault to the Eratini Fault. Phase 1,2 and 3 are represented (from 5 Ma to present day configuration). The syn-rift stratigraphy is simplified, presented with various colours and patterns as the Lower, Middle and Upper Group. ***A)*** *Rift configuration during deposition of continental facies comprising the Lower Group from Kalavrita Fault to Hidden Fault.* ***B)*** *Northward migration of the rift system with subsequent deposition of large-scale Gilbert-type deltas, migrating northwards into a lacustrine to marine basin.* ***C)*** *Structural configuration from the Kalavryta Fault in the south to the offshore North Eratini Fault. (see location in Figure 2.1). Modified from Ford et al. (2013)*

2.6 Study area

The Pliocene deep-water Pellini Member is one of the oldest members of the Pliocene-Pleistocene Rethio-Dendro Formation (R-DF), of the Lower Group. The Pellini Member is exposed ~7 km south of the of the Gulf of Corinth, along the northwestern side of the NE trending Sythas valley (Figure 1.1). The succession is only exposed in a small area (~2.5 km^2) bounded by the major normal NE dipping Amphithea Fault, and the SE dipping Sigiritsa Fault, combined with minor northwest and southeast dipping normal faults (Figure 2.4). The study area comprises multiple small-scale faults with throws rarely exceeding 10 m.

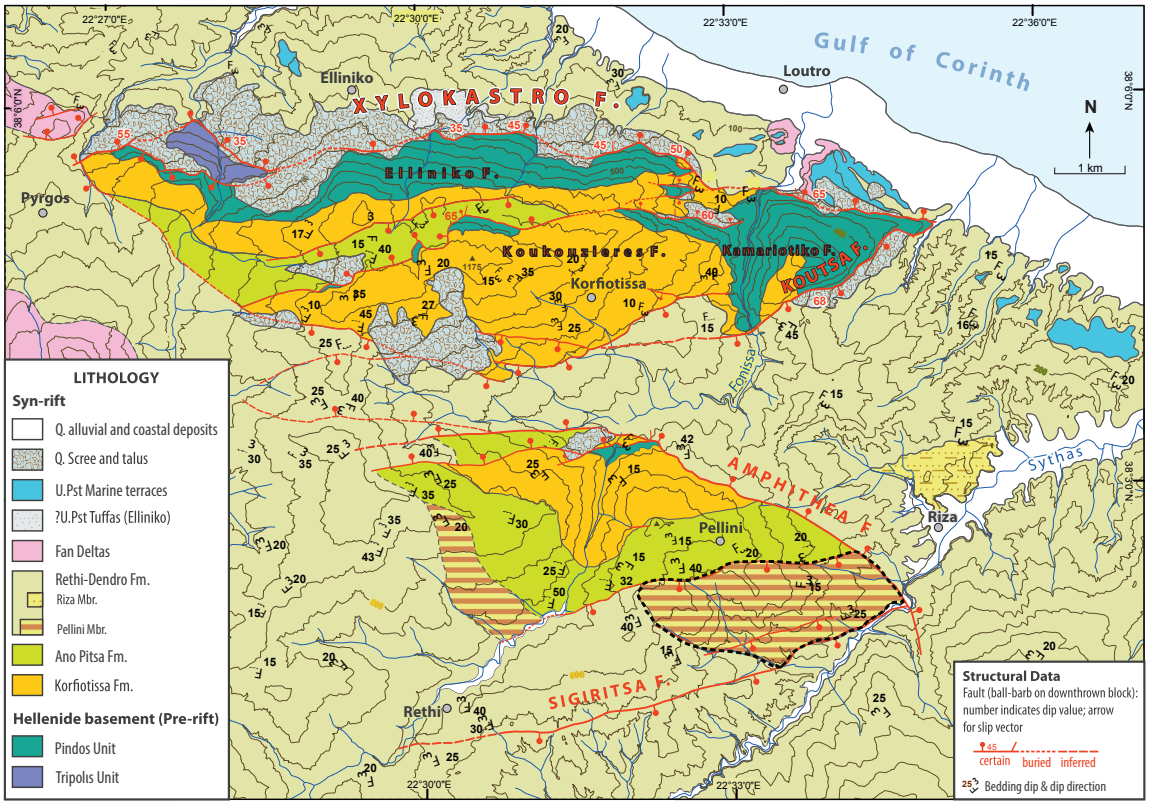

Figure 2.4: Geological map of the north central part of Peloponnese Peninsula. The black dashed line marks the study area. Modified from Skourtsos (2016) unpublished.

3. METHODS

3.1 Introduction

This study is based on data collected and interpreted during two field seasons and combines traditional field work techniques with digital analogue analysis.

3.2 Data collection

3.2.1 Traditional sedimentological techniques

The study area comprises SSE oriented gullies providing an exceptional three-dimensional aspect of the outcrops (Figure 3.1). The outcrops were accessed by car and hiking during the spring and fall 2015. Data was obtained through detailed sedimentological logging (scale 1:50), focusing on lithologies, textures, structures, boundaries, colours, bioturbation, and palaeocurrent directions. Tools such as a geological hammer, compass, measuring stick, grain size chart, magnifying glass, and acid were used. The final data set includes 21 logs (Appendix), comprising 226 meters of vertical logs. The maximum vertical extent of the study area is around 350 m, located within the middle part of the study area (Figure 3.1B, area C). Due to local variations in dip and dip-direction, the study area has been divided into areas A, B, C, D, and E for convenience (Figure 3.1). Even though area D and E display the same stratigraphic tilt and orientation (Figure 5.2B), these areas are distinguished due to correlative limitations such as faults, vegetation and scree cover.

3.2.2 Terrestrial LiDAR

Terrestrial LiDAR (Light Detection And Ranging) is a laser scanning device which digitally captures geological outcrops with high degree of accuracy, and is defined as a quantitative data collection approach (Hodgetts, 2009). A single LiDAR scan can comprise a point cloud of several million data points. These datapoints are distributed within a 3D coordinate system, individually separated with unique X, Y and Z values (Bellian *et al.*, 2005; Buckley *et al.*, 2008). However, to create a representative 3D outcrop model, high-resolution scanning has to be obtained from multiple perspectives to gain a complete coverage of the exposures of interest. This approach should be combined with traditional

field techniques (Bellian *et al.*, 2005; Hodgetts, 2009). The Digital outcrop model is generated from triangulated irregular networks of points, also referred to as TIN (Bellian *et al.*, 2005). These meshes are created in CloudCompare ,which is a 3D point cloud process software. These triangular mesh files have explicit points defined by X, Y, and Z coordinates, whereby attributes like colour can be added (Bellian *et al.*, 2005). High-resolution photographs are simultaneously obtained during surveying, which are referenced to the LiDAR scans to add qualitative colour values to the points, by draping them on to the 3D surfaces (Buckley *et al.*, 2008). The resulting photorealistic 3D model is suitable for interpretation.

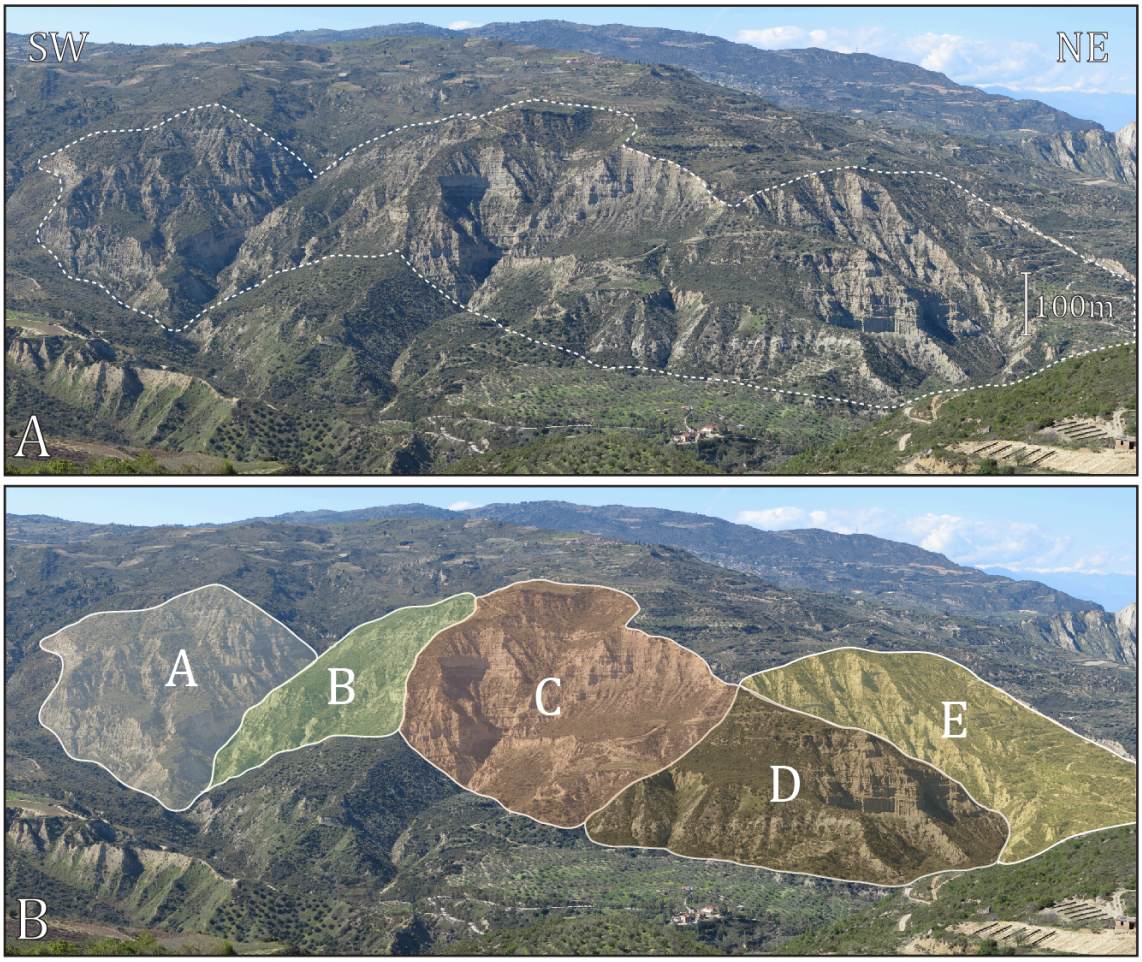

Figure 3.1: ***A****) Dashed line marking the Study area.* ***B****) Areas A to E.*

3.3 Fieldwork analysis

3.3.1 Digitizing of sedimentary logs and figures

The sedimentary logs were digitized in a 1:75 scale in Adobe Illustrator (CS6). Figures were created and photo-panels were interpreted using the same software, as well as Adobe Photoshop (CS6).

3.3.2 Processing of terrestrial LiDAR data

The acquisition and processing of the LiDAR data was done by co-supervisor Martin Muravchik, enabling analysis of the digital analogue model. For detailed outlines regarding data acquisition, processing techniques, and accuracy see Hodgetts (2009) and Rarity *et al.* (2014).

3.3.3 Digital analogue model analysis

Virtual Reality Geological Studio (VRGS) is a 3D data visualisation and interpretation software used for digital analogue models. The collected digitalized point data was manually collected on the boundaries of interest, and carefully traced while editing. Each collected point is defined by individual X, Y, Z values, automatically connected to create 3D polylines and planes.

- Polylines were manually picked along sub-horizons and planar beds to estimate tectonic tilt and dip-directions. These measurements were imported into CloudCompare after tracing. This software enabled calculations of the average dip and dip-direction of areas A, B, C, D, and E. However, area B displayed relatively high variations in dip and dip direction, which complicated the calculation.
- Planes were exclusively obtained along the lateral bounding margins of individual erosive features with the purpose to collect dip and dip direction values. These measurements were used to calculate the palaeocurrent orientation of the erosive feature, which were calculated within Stereoplot 9.5. However, orientation of the erosive features had to be corrected according to the bedding tilt and dip direction of the area the measurements were obtained from. The correction implies rotation of the obtained measurements to restore the original orientation (dip and dip direction) of the rock bodies before any tilting and folding occurred. How much

individual measurements were rotated depended exclusively on the orientation (dip and dip-direction) from which the measurements were obtained.

- Channel width and thickness measurements were collected along the channels' lateral and vertical bounding margins, by the use of vertical and lateral measuring tools in VRGS. As for the palaeocurrent corrections, width and thickness values had to be corrected according to the areas bedding orientation (dip and dip-direction).

3.3.4 Architectural elements

The interpreted rock bodies were grouped in terms of their external geometry, aspect ratio, scale and internal and facies assemblage into 11 architectural elements, grouped into channelized (7) and non-channelized elements (4) (Table 4.2 and Figure 4.2). However, not every architectural element has been logged in the field. Some elements are thus interpreted based on field observation combined with photopanels and LiDAR data analysis.

3.3.5 Channelized bodies

According to the channels' external and internal geometry, aspect ratio, bounding surfaces, facies assemblage, seven channelized bodies are distinguished within the study area: Large-scale complex sheets (Architectural Element 1), Large-scale complex ribbons (Architectural Element 2), Large-scale complex U-shaped elements (Architectural Element 3), Large-scale simple ribbons (Architectural Element 4), Small-scale U- shaped elements (Architectural Element 5), Small-scale simple ribbons (Architectural Element 6), and Small-scale ribbon-sheets (Architectural Element 7) (Table 4.2 and Figure 4.2).

3.3.6 Bounding erosive features

Each channelized entity contains one or several erosive features along its lower surface. These features are distinguished in terms of their external geometry, aspect ratio, and their erosive relief, characterized as channelized base, concave base, and scoured base for convenience (Figure 3.2). Erosive features could also occur as a single erosive step, thus referred to as a true isolated channel or as a channelized base (Figure 3.2C). The term multi-erosive channels are applied to the bodies displaying more than one erosive feature in its base. Concave and scoured features are only recorded within multi-erosive channels.

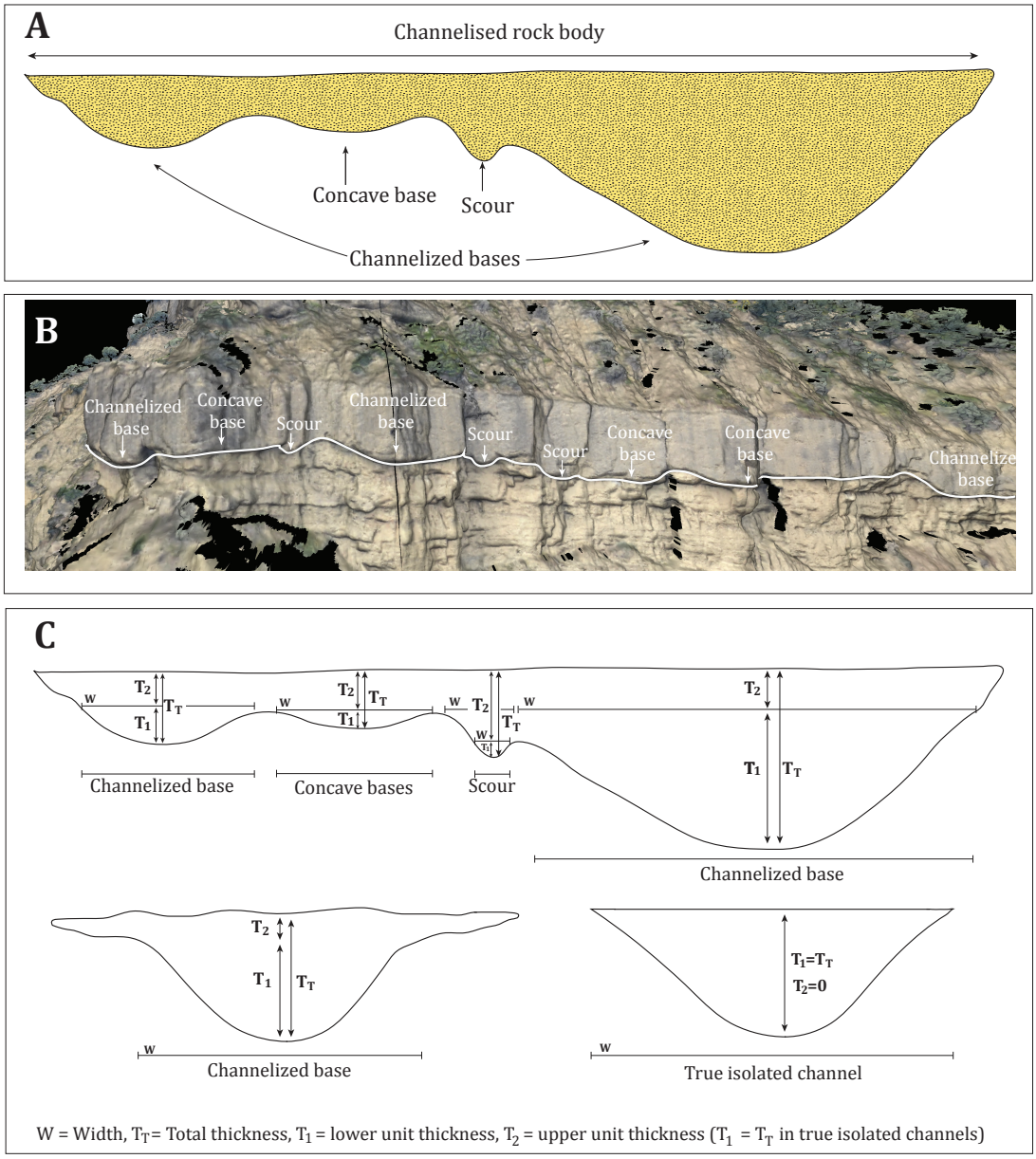

Figure 3.1: Schematic illustration or various erosive features along the lower surface of individual channels. ***A)*** *A channelized body with channelized, concave and scoured base.* ***B)*** *Digital outcrop model view of a Large-scale complex sheet (Architectural Element 1), with multiple erosive features.* ***C)*** *Illustration of how thickness and width were defined for channelized, concave and scoured bases, and true isolated channel.*

3.3.7 Correcting channel thickness and width

The apparent width and thickness dimensions of individual channel bodies is defined by its lateral and vertical bounding surfaces. Measurements were obtained in VRGS followed by subsequent correction according to the channels' position in the study area A to E.

Individual rock body orientations are seldom oriented perpendicular to its palaoecurrent direction within the outcrop section. Width measurements obtained in the digital outcrop model present the apparent width, wider than the real channel width. The real width was calculated by the use of Fabuel-Perez *et al.* (2009) trigonometric approach (Figure 3.3). However, the width of lateral extensive sheets and ribbon-shaped channels were hard to determine due to the lack of exposure within the outcrop section, scree and vegetation cover, combined with the lack of LiDAR data covering the entire length of the channelized body.

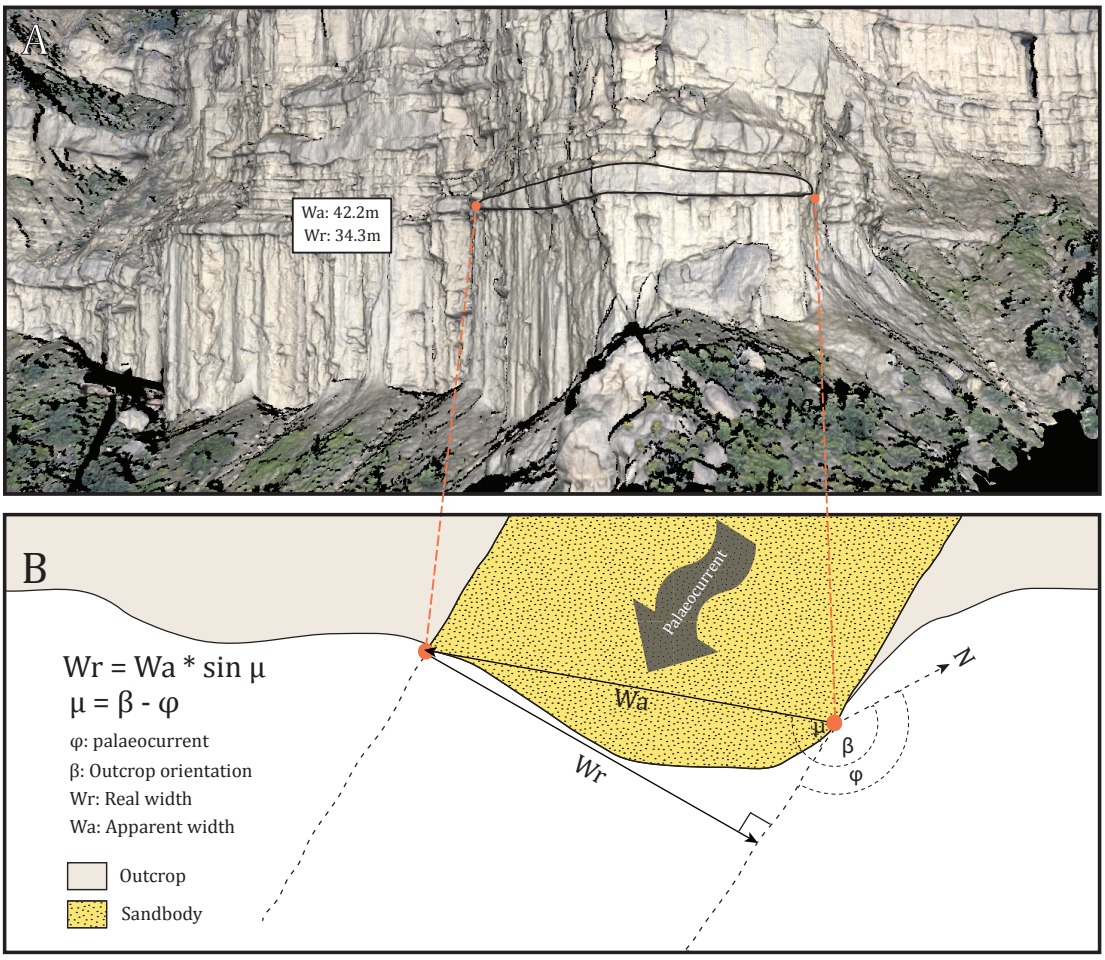

Figure 3.3: ***A)*** *Digital outcrop model view of a channelized body marked by black contour line. The white box contains the apparent width and real width values.* ***B)*** *Plan-view illustration of* ***A.*** *Method for calculating the true width from the apparent width value (Fabuel-Perez et al., 2009).*

3.3.8 Palaeocurrent analysis

Palaeocurrent data was obtained from the digital analogue model, explicitly collected from the erosive features of the channels' lower surface. The two lateral bounding margins of a single erosive feature was measured to get the dip and dip direction. These measurements were imported into Stereonet 9.5. This program enables the user to calculate the orientation of the thalweg for individual erosive features. However, the majority of the large-scale channels comprise a multi-erosive base. These channel bodies frequently contain concave and scoured features. In contrast to channelized and scoured bases, concave bases display a low-erosive step, and do not reflect a clear channelized thalweg. As such concave bases have a tendency to display a lower dip than the laterally adjacent channelized and scoured features within a multi-erosive channel base. When correcting the measurements according to the dip and dip direction of the area measurements were obtained, these features are occasionally dipping opposed to the direction of the channelized bases. Scoured bases are however, naturally dipping up-current which suggest them to be flute-marks. To calculate the mean palaeocurrent direction, these opposed palaeocurrent directions were assessed to their opposed directions relative to their orientation. Mean palaeocurrent direction could then be calculated. This was achieved by adding and dividing the palaeocurrents values by the number of measurements obtained from a multi-erosive channel.

Palaeocurrent data is presented in rose diagrams, created in Stereonet 9.5 (Allmendinger *et al.*, 2012; Cardozo and Allmendinger, 2013). The length of individual columns within a rose diagram is proportional to the number of measurements within each 15° sector at a linear scale. The columns do not display a given percentage of the total sample population, but the relative proportions, where the the longest column represent the column of highest frequency (Nemec, 1988). The coloured contours fill illustrates the density frequency of the measurements, whereby red is indicating the highest frequency of occurrence, whereas white indicate the lowest. Statistical analysis was conducted on the bulk palaeocurrent dataset by the use of Kuiper, Watson and Rayleigh tests to verify whether the palaeocurent measurements display a preferential orientation (Nemec, 2005). Referring to the method outline by Baas (2000) for a more detailed description of the Kuiper, Watson and Rayleigh tests.

3.3.9 Linear-log, semi-log, log-log, 3D scatterplots and Bar charts

Linear-log, semi-log and log-log plots were created using Microsoft Excel 14.6.1, whereas 3D scatterplots were created in MATLAB. Linear-log and log-log plots are used to analyse the *W/T* ratio of 80 channelized bodies. 3D scatter plots were created for illustration purposes, to display the channel distribution within the study area. Bar charts were created with the purpose of identifying any vertical trends of the channel body thickness, width, *W/T* ratio, and orientations against the topographic height. The stratigraphic height is not used due to the absence of both the lower and upper boundary of the Pellini Member. Nevertheless, bar charts allow recognition of apparent trends by extracting the scattered data appearance found in linear-log, semi-log and log-log scatterplots. Scattered data appearance is produced due to the wide range of channels' thickness, width, *W/T* ratio and palaeocurrent orientation at any given interval of the Pellini succession.

3.3.10 Sources of error

- The Facies assemblage within certain architectural elements are hard to distinguish in the digital analogue model.
- Some of the channelized architectural elements were not logged in the field due to their occurrences in steep and inaccessible terrain. The descriptions are thus based on LiDAR data and photo-panel interpretation.
- The tectonic tilt and dip directions were used to correct the thickness, width, dip and dip direction measurements of individual channel. However, area B comprise some variations in tectonic tilt and dip direction due to local folds within the area. This may have caused erroneous measurements, whereby the dip and dip direction is skewed relative to the true orientation.
- Mean palaeocurrent measurements are used when calculating the true width of individual channel bodies. However, individual channels are frequently comprising more than one erosive feature, whereby some features were oriented opposed to the mean apparent direction. This creates a bimodal distribution. This phenomenon is further described in chapter 5.2.1

4. LITHOFACIES AND ARCHITECTURAL ELEMENTS

4.1 Lithofacies

On the basis of macroscopic sedimentological investigation, 15 sedimentary lithofacies have been identified within the study area. Each facies is distinguished in terms of lithology, textures, sedimentary structures, degree of bioturbation, thickness, and bounding surfaces. These facies have been interpreted based on the mechanisms of transportation and deposition, following the terminology used by Lowe (1982), Kneller (1995), and Kneller and Branney (1995). The lithofacies are described and compared with other facies schemes (Bouma, 1962; Lowe, 1982) found in table 4.1.

Table 4.1: Lithofacies

Facies	Facies name	Lithology and Texture	Structures	Bioturbation	Thickness (m)	Geometry	Depositional process
A1	Marlstone (Figure 4.1 A-C)	Light yellow marlstone with occasional very fine-grained sandstone domains intercalated with the overall marlstone. Organic detritus occur	Planar parallel lamination or structureless	Moderate to high degree of bioturbation	0.01 to 0.30 m, up to 0.60 m thick beds	Tabular. Planar to irregular base. Planar, irregular or eroded top	Lime-rich mudstone precipitated directly from the water column or transported by low-density gravity flow and/or bottom current. Settles from suspension in low-energy environments (*e.g.* Pickering & Hiscott, 2015).
B1	Structureless Mudstone (Figure 4.1: D-E)	Light to dark grey and red clay and silt occasional very fine-grained sandstone domains in upper bed section. Marl, organic detritus and coal can occur	Structureless	Varying degree of bioturbation	0.01 to 0.65 m, up to 1.50 m thick beds	Tabular or wedge shaped. Irregular base. Planar, irregular or eroded top	Structureless mudstone (B1) indicate pelagic or hemipelagic suspension settling in a low-energy environment or deposition from dilute turbidity currents. Laminated mudstone (B2) suggests deposition from dilute unconfined turbidity currents such as deltaic hyperpycnal plumes (*e.g.* Pickering et al., 1986; Stow et al., 1990; Nemec, 1995; Janbu et al., 2007; Grundvåg et al., 2014; Pickering & Hiscott, 2015). Bioturbation suggest oxic environment and favourable biogenic conditions. B1 and B2 are similar to T_e and T_d division of Bouma (1962)
B2	Laminated Mudstone (Figure 4.1: F-G)	Light to dark grey mudstone and silt intercalations. Slight colour and/or textural variations. Very fine-grained sandstone, marl drapes, organic detritus and coal fragments occur	Planar parallel lamination	Low to medium degree of bioturbation	0.01 to 0.34 m up to 0.70 m thick beds	Tabular or wedge shaped. Planar to irregular base. Planar, irregular or eroded top	
C1	Laminated Heterolithics (Figure 4.1: H-J)	Laminar silt and mud alternating with very fine-grained sandstone and marlstone laminae and beds. Organic detritus and leaf imprints occur	Structureless or planar parallel stratified laminae, current ripple cross lamination frequently occur	Varying degree of bioturbation	0.008 to 0.01 m thick lamina, up to 1.10 m thick beds	Fine-grained lenses within an tabular unit. Planar or irregular base. Planar, irregular or eroded top	Products of depletive and waning turbidity flow or weak bottom currents alternating with suspension fallout material (*e.g.* Kneller, 1995; Kane et al., 2009; Jobe et al., 2010; Pickering & Hiscott, 2015). Similar to alternating division T^{cde} of Bouma (1962)

D1	Ripple cross-laminated sandstone (Figure 4.1: K-L)	Very fine- to coarse-grained sandstone. Mudstone drapes and organic detritus occur	Normal graded or ungraded asymmetrical ripples, single or stacked sets	Low to moderate degree of biortubation	0.03 to 0.07 m thick sets. 0.07 m to 0.65 m thick beds	Tabular. Planar, irregular or erosive base. Planar, irregular or eroded top	Deposition from low-density, quasi steady to waning turbidity currents (*e.g.* Janbu *et al.*, 2007; Kane et al., 2009; Grundvåg *et al.*, 2014). Similar to T^c divisions of Bouma (1962)
D2	Planar parallel laminated sandstone (Figure 4.1: L)	Very fine- to medium- grained sandstone. Pebble lags, mudstone, marl drapes and organic detritus occur	Normal graded or ungraded planar parallel-stratified sandstone.	Low degree of bioturbation.	0.005 to 0.01 m thick lamina, up to 0.60 m thick beds	Tabular. Planar or erosive base. Planar, irregular or eroded top	Deposition from a tractive low-density and down-slope decelerating turbidity currents in upper flow regime (*e.g.* Backert *et al.*, 2010; Grundvåg *et al.*, 2014). Similar to T^b divisions of Bouma (1962)
D3	Low-angle planar cross stratified sandstone (Figure 4.1 M)	Medium- to coarse-grained sandstone. Granule-to pebble lags and organic detritus occur	Normal graded or ungraded low-angle planar cross-stratified sandstone	Low degree of bioturbation	0.10 to 0.35 m, up to 0.80 m thick beds.	Tabular or wedge-shaped. Planar, irregular or erosive base. Planar, irregular or eroded top	Deposited from a tractional low-density turbidity current (*e.g.* Lowe, 1982; Kneller,1995; Pickering & Hiscott, 2015). Similar to facies T^t of Lowe (1982)
D4	Trough cross-stratified sandstone (Figure 4.1: N)	Fine- to coarse-grained sandstone with lags and domains enriched in granules and pebbles. Marl drapes, organic detritus and coal fragments occur	Normal graded or ungraded trough cross-stratified sandstone.	Bioturbation is not observed	0.30 to 0.90 m up to 1.30 m thick beds	Lenticular. Irregular or erosive concave-base. Planar or irregular top	Transported as traction bed-load , below low or high-density turbidity flow, (*e.g.* Pickering *et al.*, 1986; Mastalerz, 1995). Stratification and varying grain size suggest deposition from quasi-steady and sustained flows (*e.g.* Janbu *et al.*, 2009). Similar to a combination of facies T^t and S^1 of Lowe (1982)
D5	Crude plane parallel stratified sandstone (Figure 4.1: O-P)	Very fine- to very-coarse -grained sandstone. Granule to pebble domains, mudstone, marl drapes, organic detritus and coal fragments occur	Normal graded or ungraded planar parallel stratified to massive sandstone.	Varying degree of bioturbation	0.08 to 0.60 m thick beds	Tabular. Planar or erosive base. Planar, irregular or eroded top	Deposited from a semi-tractional surge-type, waning, high or low-density turbidity current, (*e.g.* Mastalerz, 1995; Kane *et al.*, 2009; Pickering & Hiscott, 2015) or aggradational sedimentation under depletive steady flow (*e.g.* Kneller and Branney, 1995). Similar to a combination of T^a and T^b divisions of Bouma (1962)

D6	Structureless sandstone (figure 4.1: Q-R)	Very fine- to medium-grained sandstone. Granules- cobble domains, marl, mud, organic detritus, and coal fragments occur	ungraded sandstone occasional crude normal grading	Moderate to high degree of bioturbation	0.10 to 1 m, up to 1.15 m thick beds	Tabular. Planar or erosive base. Irregular, planar or eroded top	Transported by decelerating surge-type high-density turbidity current, high suspension fall-out rate (*e.g.* Kane *et al.,* 2009; Talling *et al.,* 2012; Janocko et al., 2013; Pickering & Hiscott, 2015) or aggradational deposition by sustained steady turbidity flow (e.g. Kneller and Branney, 1995). Similar to T^a division of Bouma (1962) and S^3 of Lowe (1982)
E1	Low-angle planar cross-stratified pebbly sandstone (figure 4.1: S and V)	Moderate to poorly sorted fine- to coarse-grained sandstone with granule and pebble sized clasts (mean size 1.2 cm). Sub-rounded- to well rounded polymict, extra-formational clasts. Moderate-to low sphericity of the clasts. Internal fine to coarse grained sandstone lenses and shell fragments occur	Coarse tail normal graded (rarely ungraded) low angle planar cross stratified pebbly sandstone. Bed-aligned clast orientation. Internal isolated planar stratified sandstone lenses occur	Bioturbation is not observed	0.50 to 1.25 m, up to 1.90 m thick beds	Tabular or lenticular Irregular or erosive base. Irregular top. Irregular top with a dcm to m scale relief. Planar or Irregular top	Transported as gravel sheets in a tractional high-density turbidity current. Sharp based sandstone lenses indicate late stage deposition under rapid suspension fallout rate (*e.g.* Di Celma et al., 2010; Pickering & Hiscott, 2015). Similar to facies S^1 of Lowe (1982)
E2	Planar cross-stratified conglomerate (figure 4.1: T-U)	Moderate to poorly sorted matrix-supported conglomerate, occasional clast-supported (base). Often matrix rich in top. Sub-rounded to well rounded polymict, extraformational granules to cobble sized clasts. Moderate to low sphericity. Mean size 2.5-4 cm. Well to poorly sorted fine to very coarse-grained sandstone matrix, frequently overlain by . sandstone lenses with occasional pebble lags (Facies D2 and D3) . Organic detritus and coal fragments occur	Normal or ungraded planar (E2) or trough (E3) cross-stratified conglomerate. Bed-aligned clast orientation.	Bioturbation is not observed	0.20 to 1.50 m, up to 1.95 m thick beds	Tabular, wedge or lenticular. Irregular or erosive base with a dcm to m scale relief. Planar or Irregular top	Normal and ungraded matrix supported and stratified conglomerate suggest deposition from a tractive, high-density waning or quasi-steady turbidity current (*e.g.* Lowe, 1982; Kneller, 1995; Di Celma *et al.,* 2010). Erosion based sandstone lenses suggest late stage deposited under rapid suspension fallout rate (*e.g.* Di Celma *et al.,* 2010) Clast supported conglomerate suggest rapid deposition by turbulent flow influenced by dispersive pressure below high-concentration tractional turbidity flows creaing 2D and 3D gravel dunes (*e.g* Walker, 1975; Pickering *et al.,* 1986; Backert *et al.,* 2010; Di Celma *et al.,* 2010). E2 and E3 are similar to division R^1 and R^3 of Lowe (1982)
E3	Trough cross-stratified conglomerate						

E4	Structureless conglomerate (Figure 4.1: V-W)	Poorly sorted clasts (base) and matrix supported conglomerate. Sub-rounded to angular extra-formational granule- to pebble-size clasts. Mean grain-size 0.5–2 cm. Medium- to very coarse-grained sandstone matrix	structureless conglomerate. Randomly Oriented clasts	Bioturbation is not observed	0.10 to 0.30 m thick beds	Lenticular. Irregular or erosive base. Irregular top	Transported as bedload by quasi-steady, high-density turbidity currents. Rapid deposition results in poorly organized clast fabric and the absence of internal structures (*e.g.* Kneller, 1995; Pickering and Hiscott, 2015). Similar to facies R^3 of Lowe (1982)
F1	Folded and contorted strata (Figure 4.1: X-Z)	Massive, poorly sorted matrix-rich conglomerate, medium coarse-grained sandstone and mudstone. Rounded to sub-rounded granule to cobbles-sized clast. Mean size 3-4 cm. Organic detritus, coal fragments occur	Chaotic, highly deformed, contorted sediments, folded and rotated deposits.	Bioturbation is not observed	Locally 8 m thick unit but up to 25 m in most of the area it is exposed	Tabular. Irregular top. Base covered by debris, not exposed	Gravity-induced mass movements initiate when the sediments internal shear-strength is exceeded(*e.g.* Postma, 1984; Nemec, 1990). Slumps are emplaced when internal friction overcome gravitational forces (*e.g.* Pickering and Hiscott, 2015).

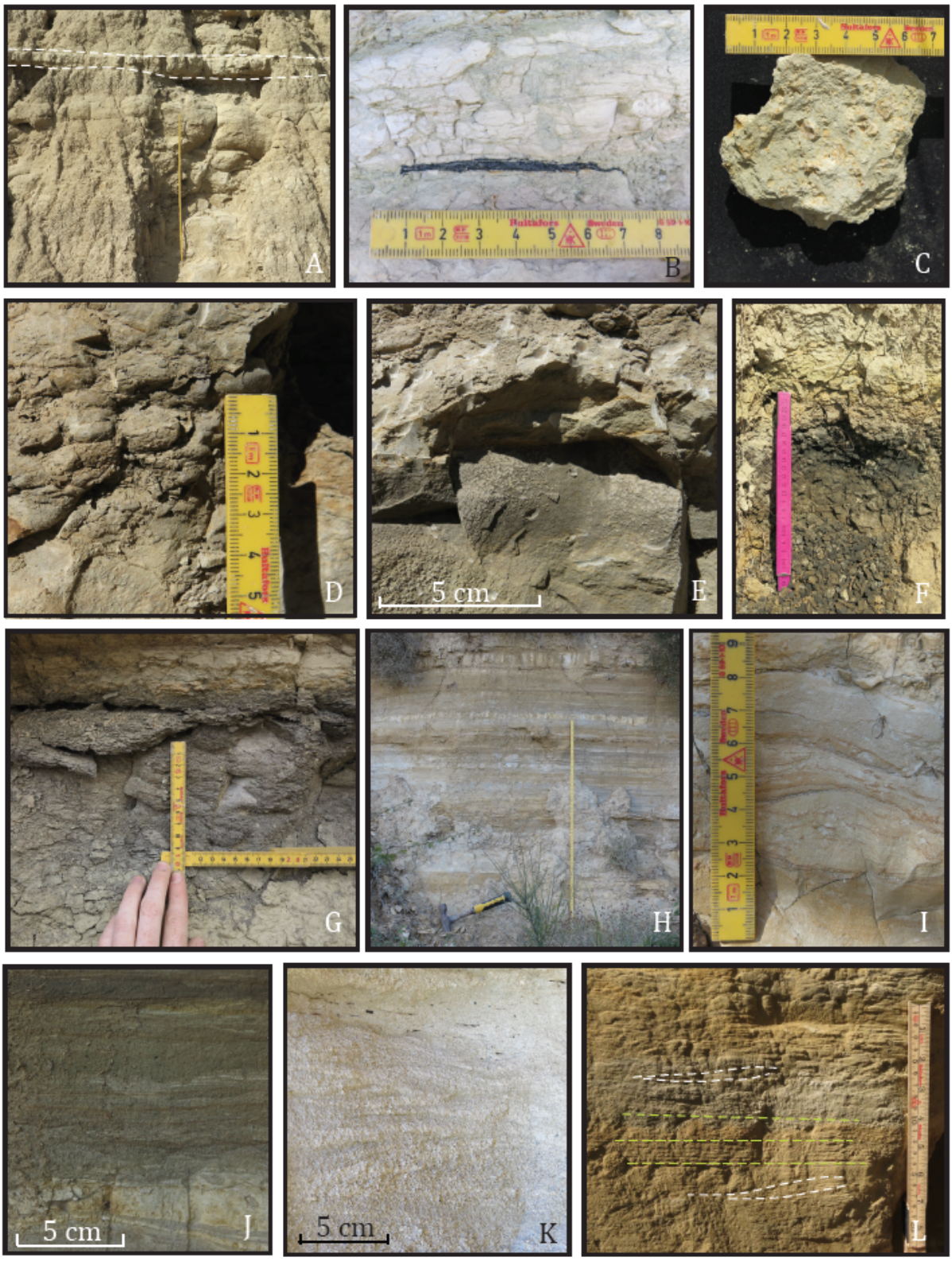
A
B
C
D
5 cm
E
F
G
H
I
5 cm
J
5 cm
K
L

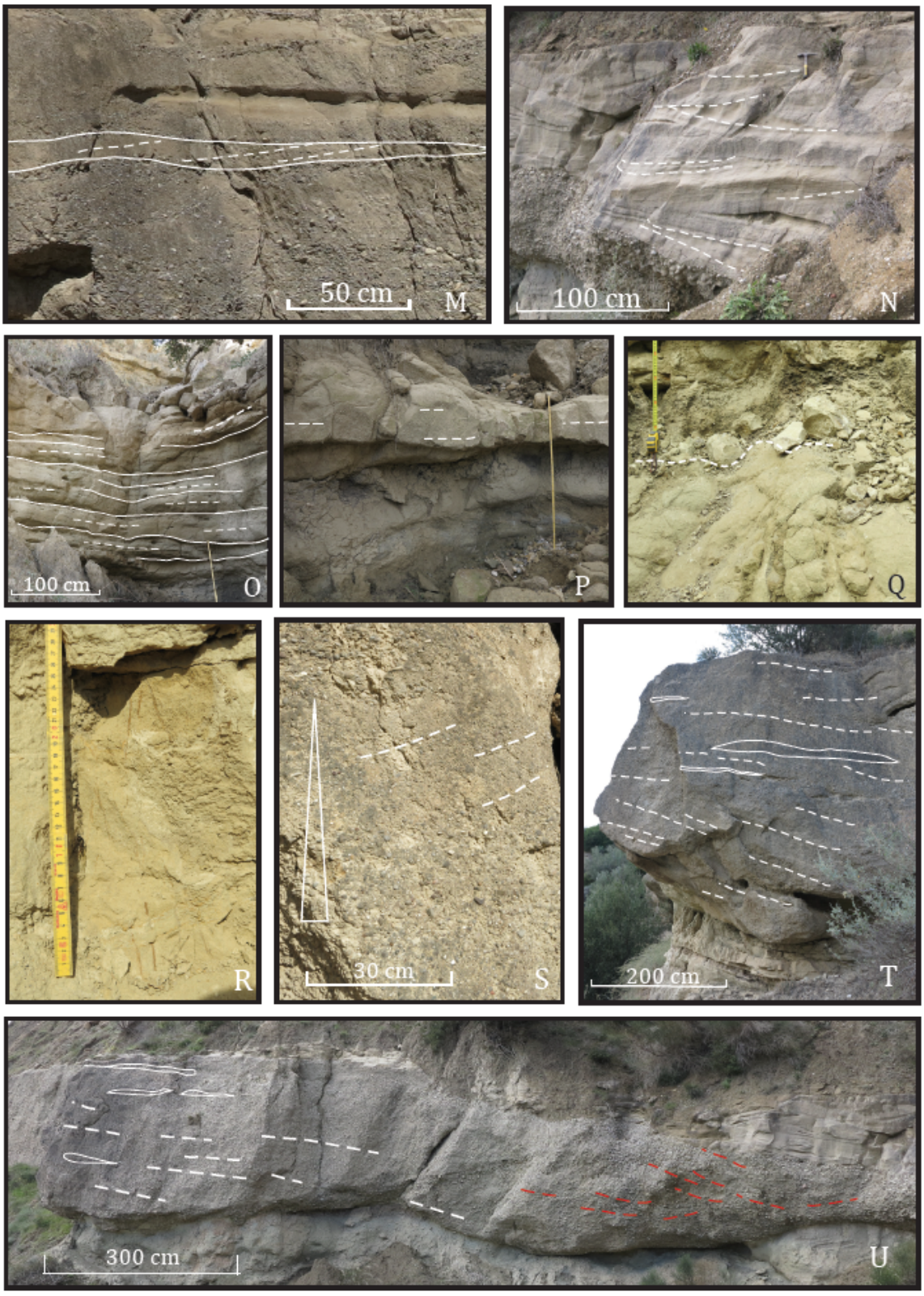
50 cm
M
100 cm
N
100 cm
O
P
Q
R
30 cm
S
200 cm
T
300 cm
U

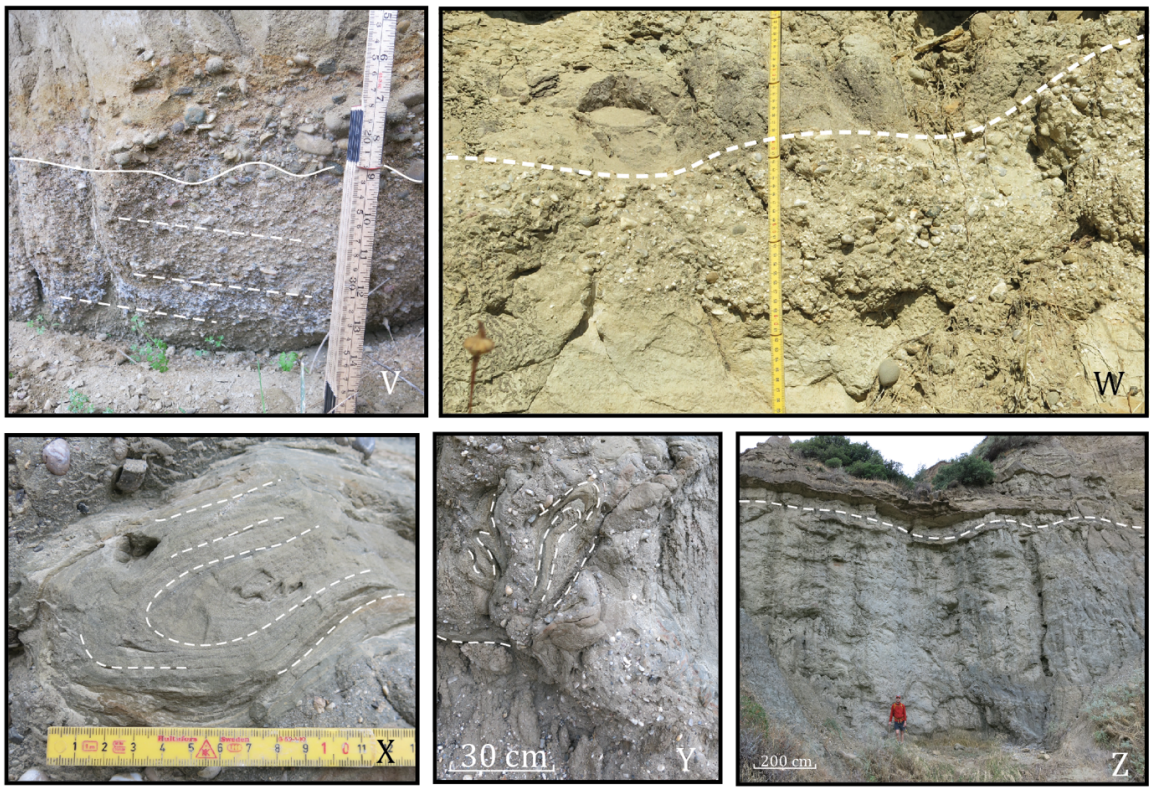

Figure 4.1: Lithofacies field photographs: ***A-B)*** *Planar parallel laminated marlstone bed (A1).* ***C)*** *Structureless marlstone (A1).* ***D-E)*** *Structureless mudstone (B1).* ***F-G)*** *Laminated mudstone (B2).* ***H-J)*** *Laminated heterolithics, alternating marlstone, mudstone and very fine-grained sandstone (C1).* ***K-L)*** *Ripple cross-laminated sandstone (D1), marked by white dashed lines.* ***L)*** *Planar parallel laminated sandstone (D2), marked by green dashed lines.* ***M)*** *Low-angle planar cross-stratified sandstone (D3) in upper parts of channelized conglomerate.* ***N)*** *Trough cross-stratified sandstones (D4) in upper part of channelized conglomerate.* ***O)*** *Succession of crude planar parallel stratified sandstone sheets (D5) in an unconfined interchannel setting.* ***P)*** *Single bed of crude planar parallel stratified sandstone (D5).* ***Q)*** *Structureless interchannel sandstone beds (D6), below white dashed line.* ***R)*** *Structureless interchannel sandstone bed (D6).* ***S)*** *Low-angle planar cross-stratified pebbly sandstone (E1) in a channelized body.* ***T-U)*** *Planar cross-stratified conglomerate (E2) in channelized bodies.* ***U)*** *Planar (E2), (white dashed lines), and trough (E3), (red dashed lines) cross-stratified conglomerate in a channelized body.* ***V)*** *Low-angle planar cross-stratified pebbly sandstone (E1), overlain by structureless conglomerate (E4) in a channelized body, marked by a dashed line.* ***(W)*** *Structureless conglomerate (E4), in channelized bodies.* ***W-Z)*** *Chaotic distorted and folded successions of mudstone, sandstone, and conglomerate within a slumped element (F1).*

4.2 Architectural elements

The marlstone, mudstone, sandstone, and conglomerate deposits of the Pellini Member display a high variety of architectural elements, distributed along the lateral and vertical extent of the study area. An architectural element is defined as a rock body classified according its external and internal geometry, aspect ratio, scale and internal facies assemblage (Miall, 1985). Eleven architectural elements are identified, based on parameters for the classification of fluvial deposits, proposed by Miall (1985), which have been subsequently applied to depositional units within various deep-water systems (*e.g.* Mutti and Normark, 1987; Clark and Pickering, 1996; Prèlat *et al.*, 2009; Janocko *et al.*, 2011; McHargue *et al.*, 2011).

The architectural elements are grouped into (1) channelized elements and (2) non-channelized elements (Table 4.2 and Figure 4.2), described according to the terminology used by various authors (*e.g.* Potter, 1967; Friend *et al.*, 1979; Miall, 1985; Gibling, 2006; Veiga *et al.*, 2009). Architectural element characterizations provide useful information regarding the dynamics of sediment transport mechanisms, energy conditions and depositional processes. The lack of terrestrial indicators such as trace fossils, plant imprints and coal horizons, combined with the occurrence of lime rich mudstone and a large-scale slump complex suggest deposition in a subaqueous environment.

For the purpose of this study an outcrop-based hierarchical scheme proposed by Ghosh and Lowe (1993) is used to analyse the 11 architectural elements. This approach has proven to be successful when applied to other ancient deep-water deposits (*e.g.* Hickson and Lowe, 2002; Di Celma, 2011). By applying this hierarchical stratigraphic framework, architectural elements within the Pellini Member can be characterized in the order of 4 hierarchical divisions (Figure 4.3). First-order architectural elements represent the smallest-scale lithologic elements (*i.e.* single sedimentary structures within a depositional element; Figure 4.3A and B). Second-order architectural elements are distinguished as elements deposited by single events of gravity flows (*e.g.* the bouma sequence; Figure 4.3A). Third-order architectural elements are composed of stacked first- and second-order elements, typically defining a single-storey channel and alternating sandstone and mudstone sheets (Figure 4.3A and B).

Table 4.2: Architectural elements:

Group	Architectural Element		Lithofacies	Interpretation
Channelized Elements:	AE1	Large-scale complex sheets	D3 ,D5, E1, E2	Sinuous, meandering channel complex
	AE2	Large-scale complex ribbons	A1*, B1*, D3, D4, D5, D6*, E1, E2, E3	Sinuous, low to moderately meandering channel complex
	AE3	Large-scale complex U-shaped elements	D3, D5, E2	Non-meandering channel complex
	AE4	Large-scale simple ribbons	D3, D4, D5, D6*, E1, E2	Sinuous, meandering channel
	AE5	Small-scale simple U-shaped elements	D4, D5, E1	Proximal crevasse channel
	AE6	Small-scale simple ribbons	D4, E2, D6*	Medial crevasse channel
	AE7	Small-scale simple ribbon-sheets	Facies group D	Distal crevasse channel to crevasse splay
Non-channelized Elements:	AE8	Deformed large-scale complex sheets	F1	Slump complex
	AE9	Thin- to thick-bedded sandstone sheets	A1, B1, B2, C1*, D1, D2, D3, D4, D5, D6, E1*, E2, E4	Sandy interchannel
	AE10	Sandy heterolithics	C1, D5	Heterolithic interchannel
	AE11	Mudstone with thin-bedded sandstone sheets	A1, B1, B2, C1*, D6*	Muddy interchannel

* = lithofacies occurring less frequently. AE = Architectural Element

Fourth-order architectural elements are composed of vertically and laterally stacked third-order elements and are distinguished as large-scale channels within the Pellini Member (Figure 4.3A and B).

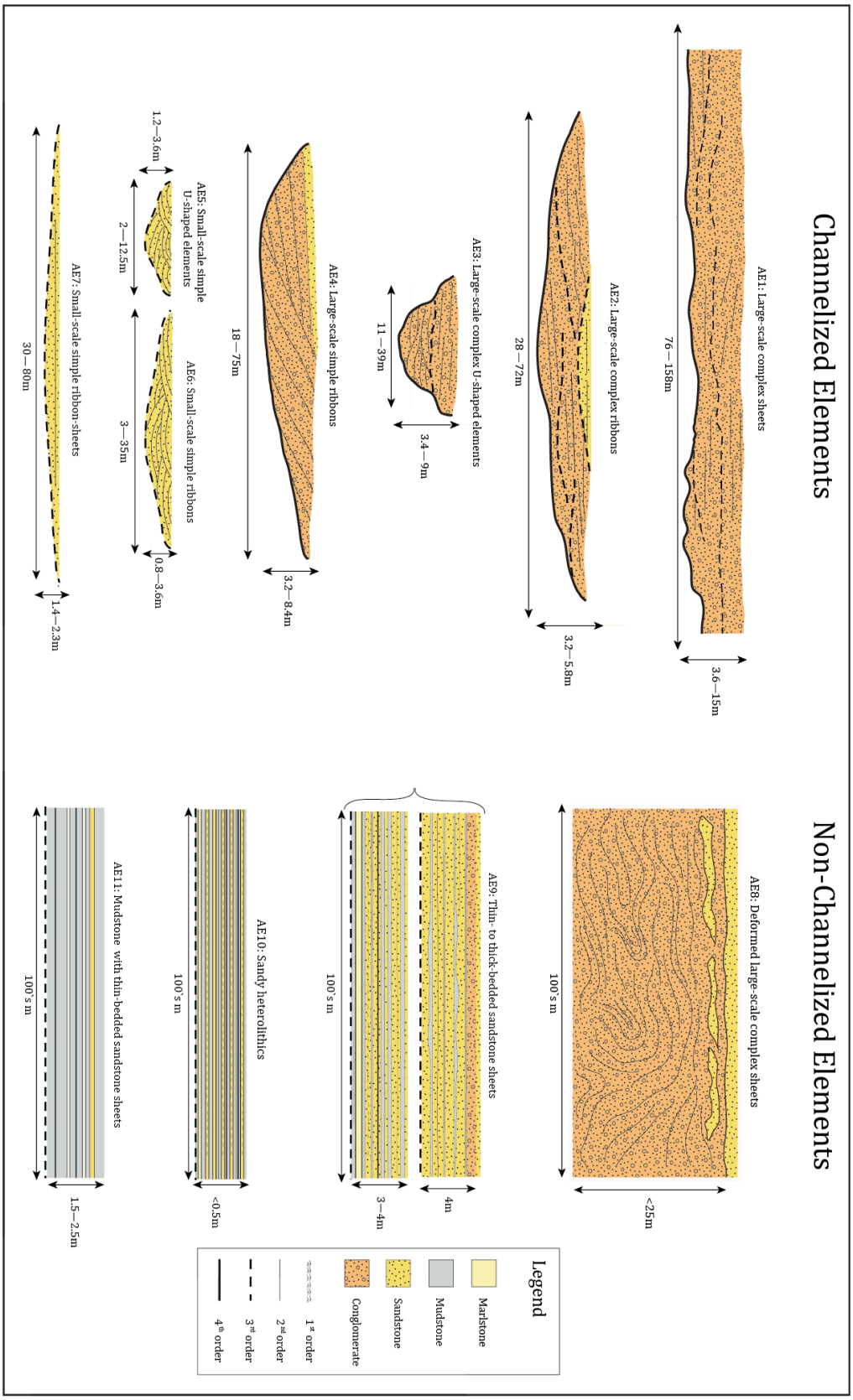

Figure 4.2: Architectural elements identified within the Pellini Member, seven channelized elements and four non-channelized elements. Stratal surfaces are defined according to the hierarchy classification scheme of Ghosh and Lowe (1993).

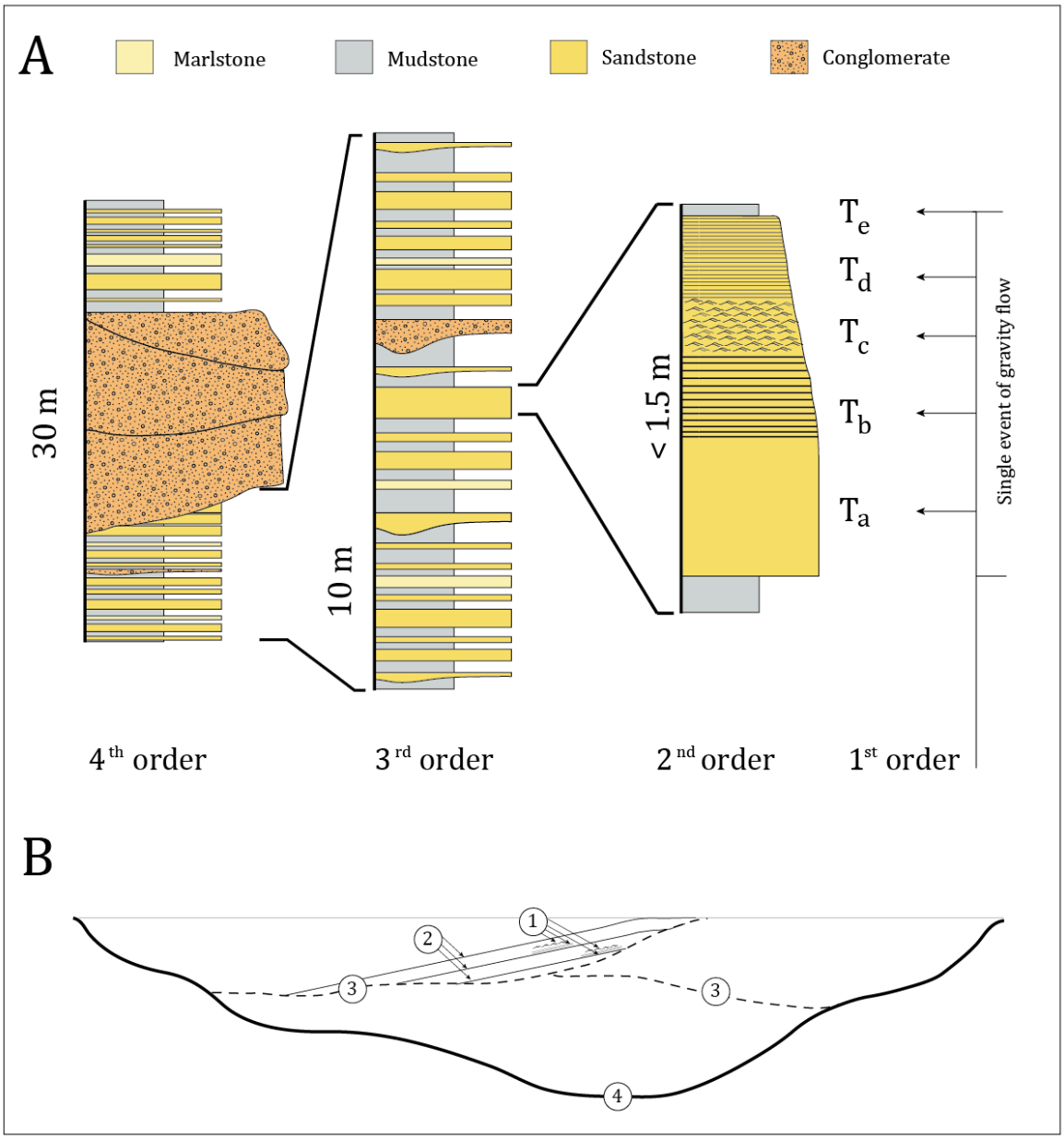

Figure 4.3: A) Illustration of the hierarchical classification of 1st to 4th order architectural elements within the Pellini Member. First order architectural elements displayed as T_a to T_e refer to the sequence division of Bouma (1962). This scheme is similar to that of Ghosh and Lowe (1993) and Hickson and Lowe (2002). ***B)*** *Illustration of the hierarchical levels within a channel complex, modified from Miall (1985). Numbers refer to the hierarchical levels from 1st to 4th order.*

4.3 Channelized elements

A total of 97 channels and channel complexes have been identified in the field, 25 of which were logged, while 80 were analysed from the digital outcrop model, which includes six of the logged entities. Channels range in thickness from 0.8 to 15 m, and vary between 2.4 and 158 m in width, with a *W/T* ratio spanning from 1.6 to 35. The apparent channel width was not possible to collect from every channel body due to limited outcrop exposure. Nevertheless, it provided information on the minimum width value. Channel width and thickness measurements were obtained in Virtual Reality Geological Studio (VRGS). These channels were classified according to their thickness, width and aspect ratio following a modified scheme from Gibling (2006; Table 4.3 and Figure 4.2), combined with other factors such as internal organization, lithofacies assemblage, and the channels' spatial relation to other architectural elements.

Table 4.3: Criteria used for the description of width, thickness and aspect ratio of deep-water channel bodies.

Width (m)		**Thickness (m)**		**Width/Thickness**	
Wide	> 100	Thick	> 6	Sheets	> 15
Medium	> 50	Medium	> 3	Ribbon sheets	> 10
Narrow	> 10	Thin	> 1.5	Ribbons	> 4.4
Very narrow	< 10	Very thin	< 1.5	U-shaped	< 5.5

Seven types of channelized rock bodies were distinguished within the Pellini Member: 1) Large-scale complex sheets, 2) Large-scale complex ribbons, 3) Large-scale complex U-shaped elements, 4) Large-scale simple ribbons, 5) Small-scale simple U-shaped elements, 6) Small-scale simple ribbons and 7) Small-scale simple ribbon-sheets (Figure 4.2). These channelized units occur relatively closely spaced within the Pellini succession, either as stacked or isolated bodies encased within non-channelized deposits. Large-scale channels are frequently exhibiting a complex internal organization, with multiple erosion surfaces, defined as multi-storey channels or channel complexes. In contrast, the small-scale channels are most frequently single-storey or simple channels (Potter, 1967; Friend *et al.*, 1979). Channel bases comprise single or multiple erosive features, characterized as channelized, concave or scoured, according to the erosive character, aspect ratio and the erosive step (Figure 4.4). Laterally extensive large-scale channels frequently comprise multiple erosive features in comparison to small-scale narrow channels. Channels with a

single erosive feature are either defined as true isolated channels or as a channel with a channelized base (Figure 4.4). The channel orientation was calculated by the use of measurements obtained in the digital outcrop model from the lateral bounding margins of individual erosive features. Scoured bases were frequently displaying an opposed direction, relative to the main direction of the majority of concave and channelized bases. There is thus a possibility that the scoured bases, dipping opposed to the main channel direction are flute marks (Figure 4.4C). Flute marks are discontinuous, elongated and asymmetrical in cross section, aligned parallel to the sediment transport direction, whereby its steepest and deepest division is directed down-current, opposite to its tapered edge which is oriented up-current (*e.g.* Reineck and Singh, 1980; Nichols, 2009; Boggs, 2011).

Table 4.4: Definitions of criterias used to defining erosive features within a multi-erosional channel body according to aspect ratio, width and thickness dimensions.

Erosive feature	**Width/T1**	**Width (m)**	**T1 (m)**	**T1/T2**
Channelized base	2 – 29	2.5 – 72	0.7 – 4.6	0.2 – 4.8
Concave base	2.5 – 59	1.2 – 77	< 1.6	0.7 – 15
Scoured base	< 4.8	< 3.2	< 2	0.3 – 17

The majority of the investigated channelized bodies of the Pellini Member comprises conglomerate and sandstone-dominated deposits. The channel fill varies from being entirely sand-filled, to display a complex conglomeratic fill with high or low matrix content. However, most of the larger scale channels are dominated by matrix-supported lithic conglomerates. The mineralogical composition includes a large range of lithologies: white/grey pelagic limestone, red, green or black chert, white quartz and yellow/brown or grey metamorphic sandstone clasts. These clasts derive from the pre-rift units of the Hellenic thrust sheets, and reflect a siliceous rich feeder system. The majority of the clasts are prolate to sub-spherical and sub-rounded to well rounded. Grain size spans from granule to cobble-grade, seldom exceeding 100 mm in its longest axes, and between 0.5 and 40 mm in diameter.

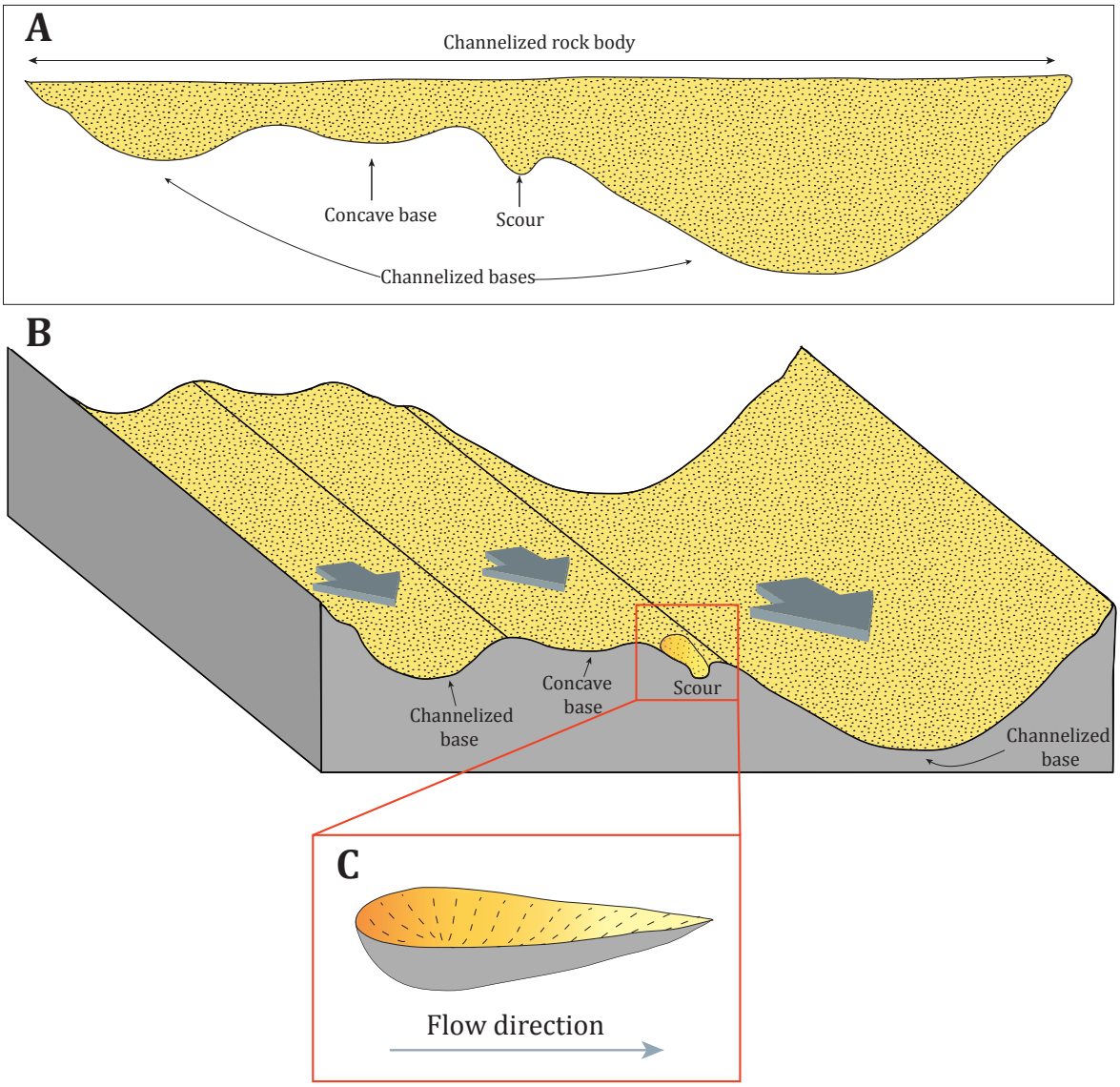

Figure 4.4: ***A)*** *Various erosive features are found in the base of channel bodies. Channelized, concave and scoured bases are terms used for convenience to illustrate the erosive characteristics.* ***B)*** *Block diagram of a channel with various erosive features. Blue arrows represent the flow direction.* ***C)*** *Close-up illustration of a scoured base in* ***B****.*

4.3.1 AE1: Large-scale complex sheets

Description

Large-scale complex sheets (Architectural Element 1) are characterized as the thickest and most laterally extensive channel complexes observed within the study area, with a *W/T* ratio of 15 to 30. These channels display a high degree of internal complexity, which increases progressively upwards within the Pellini succession. The width of the channels are in the range of 76 to 156 m, and the thickness varies from 3.6 to 15 m. Large-scale complex sheets are defined as 4th order elements, frequently bounded by an irregular base, and a planar or irregular top, defining a sheet-shaped geometry. However, occasional local high-erosive steps are recorded with an erosive relief of up to 3 m.

Architectural element 1 is a multi-storey channel complex, comprising amalgamated and juxtaposed channel entities(Potter, 1967). Large-scale complex sheets comprise up to 4 laterally and vertically stacked tabular, ribbon and/or wedge-shaped channel bodies, defined as 3rd order elements (Ghosh and Lowe, 1993; Figure 4.5). These 3rd order elements are up to 8 m thick and are bounded by multi-erosive bases, and planar, irregular or eroded tops. Individual storeys comprise channelized, concave, and scoured bases (Figure 4.4), which rarely exceed 1.5 m of vertical relief. Scoured bases frequently display an opposed dip, relative to the dip direction recorded from the laterally adjacent concave and channelized bases.

Individual channel storeys are filled by amalgamated, large-scale, inclined beds or planar to subhorizontal beds. Large-scale inclined beds range in dip between 4° and 25°, formed in low angle planar cross-stratified sandstone (Facies D3) and planar cross-stratified conglomerates (Facies E1 and E2), whereas planar to subhorizontal beds are formed in crude planar parallel stratified sandstone (Facies D5). The internal strata of individual channel storeys display either a unidirectional dip direction or diverging dip directions. The diverging dip directions display juxtaposed bedsets with an opposed inclination (Figure 4.5C). Planar to subhorizontal beds predominate in the upper section of the channel fill.

Individual beds are between 0.3 and 2 m thick, and can form up to 5 m thick amalgamated bedsets. They are occasionally overlain by <0.5 m thick sandstone lenses, displaying low-angle planar cross-stratification (Facies D3). These sandstone lenses are frequently distributed within the middle and upper part of the channel fill, overlain by erosive conglomerate bedsets, which gradually become more sand-prone towards the top.

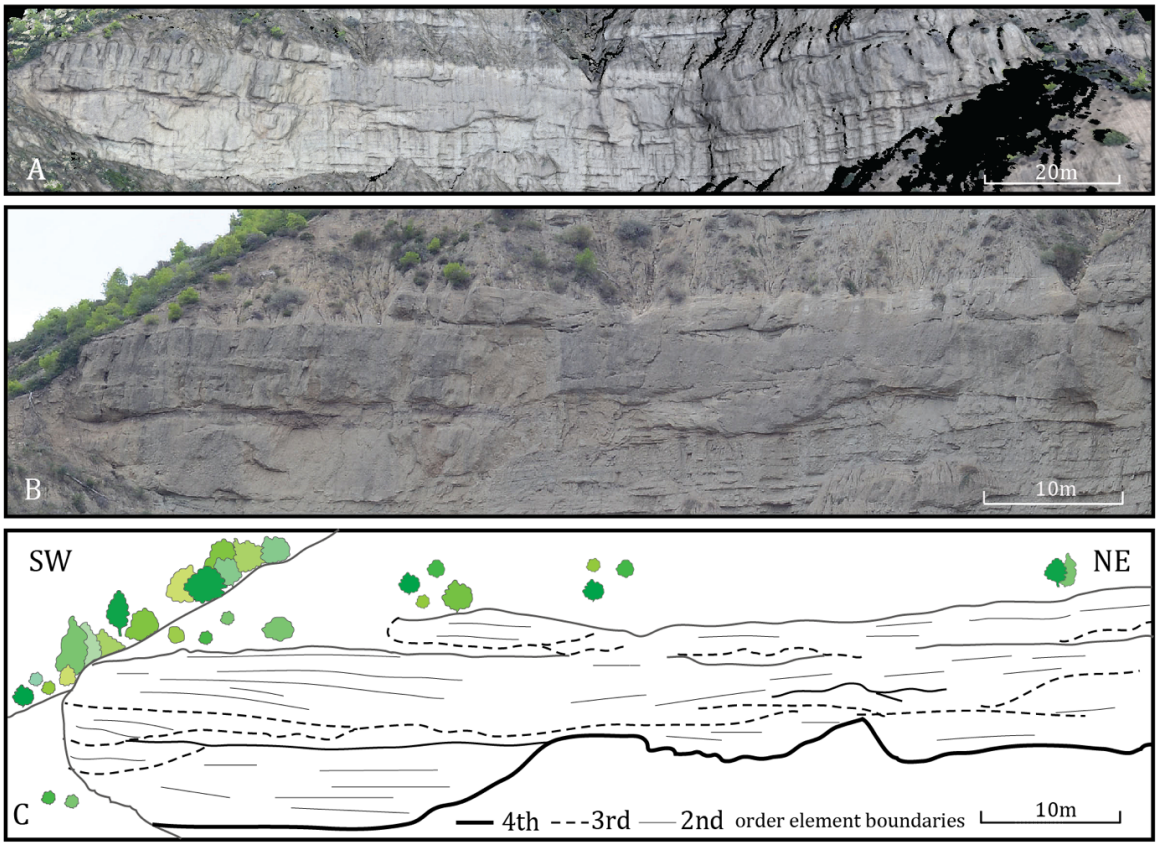

Figure 4.5: Large-scale complex sheets (Architectural Element 1). ***A)*** *Digital outcrop model view of a Large-scale complex sheet.* ***B)*** *Field photograph of the same body shown in* ***A****.* ***C)*** *Overlay drawing and interpretation of 2nd, 3rd and 4th order element boundaries observed in the rock body shown in* ***A*** *and* ***B****.*

Large-scale complex sheets are distributed laterally adjacent to Large-scale complex U-shaped elements (Architectural Element 3), Small-scale simple U-shaped elements (Architectural Element 5), and Small-scale simple ribbons (Architectural Element 6) with a lateral distance under 100m. The uppermost deposits are planar to subhorizontal, frequently covered by scree or vegetation, which suggest a fine-grained nature for the overlaying deposits (Figure 4.5B, 4.6A). These multi-storey channels erode down into underlying successions of sandstone sheet (Architectural element 9; Figure 4.5B and 4.6A), and fine-grained mudstone deposits (Architectural Element 11). No signs of bioturbation are observed in Architectural Element 1.

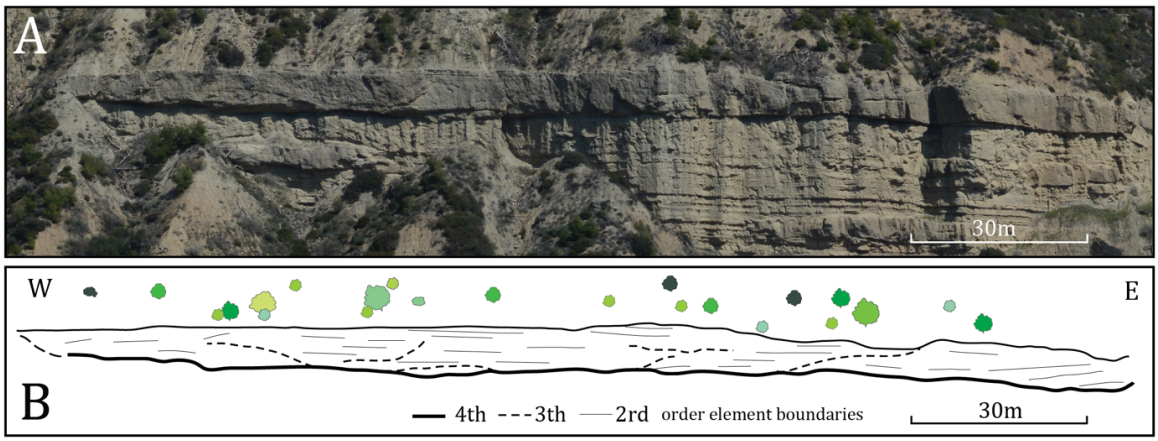

Figure 4.6: Large-scale complex sheet (Architectural Element 1). ***A)*** *Outcrop photography.* ***B)*** *Overlay drawing and interpretation of 2nd, 3rd, and 4th order elements observed in the channel complex shown in* ***A****.*

Interpretation

Based on the large-scale sheet-shaped geometry, the abundance of internal erosional surfaces and amalgamated large-scale inclined bedsets, combined with the absence of levee deposits, suggests Large-scale complex sheets to have a non-leveed, sinuous and meandering channel origin. (*e.g.* Abreu *et al.*, 2003). The juxtaposed internal storeys may have been generated by the same subaqueous channel over a relatively short period of time, or it may reflect overbank emplacement of a different channel over a relatively long period of time (Ghosh and Lowe, 1993). The internal palaeochannels contain various basal erosive features, which could indicate diversity in the flow shear stress exerted on the channel base, creating channelized, concave, and scoured bases. It is also indicative of the degree of erosional resistance of the underlying substratum and channel bank materials *(e.g.* Amy *et al.*, 2004). Stepped erosive surfaces suggest significant phases of erosion during a relatively short time-lag between scouring and deposition, which presumably would have been smoothened by trespassing currents if sufficient time was provided (Hickson and Lowe, 2002; Kane *et al.*, 2009).

Scoured bases, oriented opposed to the concave and channelized bases suggest them to be flute marks (Figure 4.4). Such features are generated by turbulent eddies within a flow, which erode the underlying substratum and generate asymmetric elongated features parallel to flow direction (Nichols, 2009).

Large-scale amalgamated inclined surfaces are interpreted as lateral accretion packages (*sensu* Abreu *et al.*, 2003), which suggests development of point bars generate during lateral migration of the channels (*e.g.* Janbu *et al.*, 2007; Janocko *et al.*, 2011). Diverging lateral accretion packages within one single channel storey, suggest meander bend evolution by lateral expansion and downstream translation (Figure 4.7). This phenomenon causes a marked widening of the channel planform, which could explain the relative high *W/T* ratios (*e.g.* Janbu *et al.*, 2007).

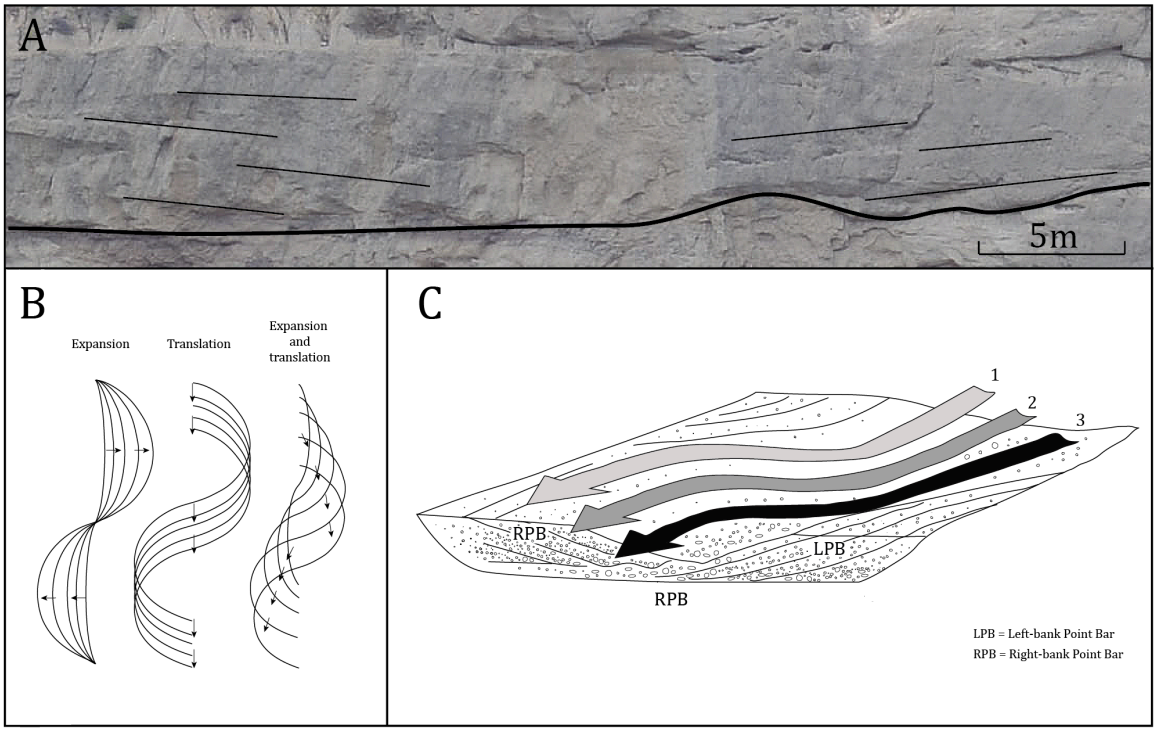

Figure 4.7: Large-scale complex sheet (Architectural Element 1). ***A)*** *Detailed photography of the channel complex presented in Figure 4.5, showing diverging lateral accretion packages formed in conglomerates and sandstone (Facies group D and E). The measured palaeocurrent direction is directed away from the viewer.* ***B)*** *Meander bend evolution by expansion, translation, and expansion and translation. The arrows illustrate the mean vector direction.* ***C)*** *Simplified illustration of the meander bend evolution, resulting in point bar stacking due to combined expansion and translation. Modified from Janbu et al. (2007).*

The presence of normal graded planar parallel cross-stratified conglomerates (Facies E2) suggests deposition from sustained to quasi-steady tractive high-density turbidity currents (Lowe, 1982; Kneller, 1995). These accretion packages represent layer by layer deposition through multiple flow events of long lived non-cohesive flows, whereby large quantities of finer-grained sediments were bypassing as suspended sediment load (*e.g.*

Kane *et al.*, 2009). The amalgamated upper planar to subhorizontal beds represent the last stage channel fill. These beds suggest that the channel became gradually abandoned during mid to late stage channel infilling, when channel erosion was oversome by sedimentation. The planar top immediately overlaid by mudstone deposits suggests abrupt abandonment of the channel system due to upstream avulsion or abandonment when the channel system was filled up (Janbu *et al.*, 2007; Prèlat *et al.*, 2009; Prélat and Hodgson, 2013). When meandering channel systems become abandoned, sedimentation of relatively finer grained material becomes more dominant.

According to the numerical and laboratory experiments of Janocko and Nemec (2011); Janocko *et al.* (2011), turbiditic channels are only meandering when close to their state of equilibrium, suggesting Architectural Element 1 to have reached, or was close to reaching its equilibrium state. The state of equilibrium is characterized by the balance of erosion and sedimentation, whereby the amount of sediment being removed by erosion is balanced by the sediment deposited as lateral accretion packages. This balance causes channel meandering and point bar migration (Janocko and Nemec, 2011; and references therein).

4.3.2 AE2: Large-scale complex ribbons

Description

Large-scale complex ribbons (Architectural Element 2) are some of the most frequently occurring channelized elements of the Pellini Member. Large-scale complex ribbons are characterized by their complex cross cutting internal organization of laterally and vertically amalgamated 3rd order elements, and coarse-grained winged margins, defining a ribbon-shaped body. Architectural Element 2 differ from Large-scale complex sheets (Architectural Element 1) by being less laterally and vertically extensive, frequently displaying a main channel thalweg. Large-scale complex ribbons range in thickness between 3.2 and 5.8 m, in width from 28 to 72 m, displaying a *W/T* ratio varying from 5 to 14. They can accommodate up to 4 vertically stacked ribbon-shaped 3rd order elements. The external margins are mainly symmetrical, inclined at 25° to 40°. The basal surface frequently displays locally stepped erosive reliefs, expressed by channelized, concave and scoured erosive features.

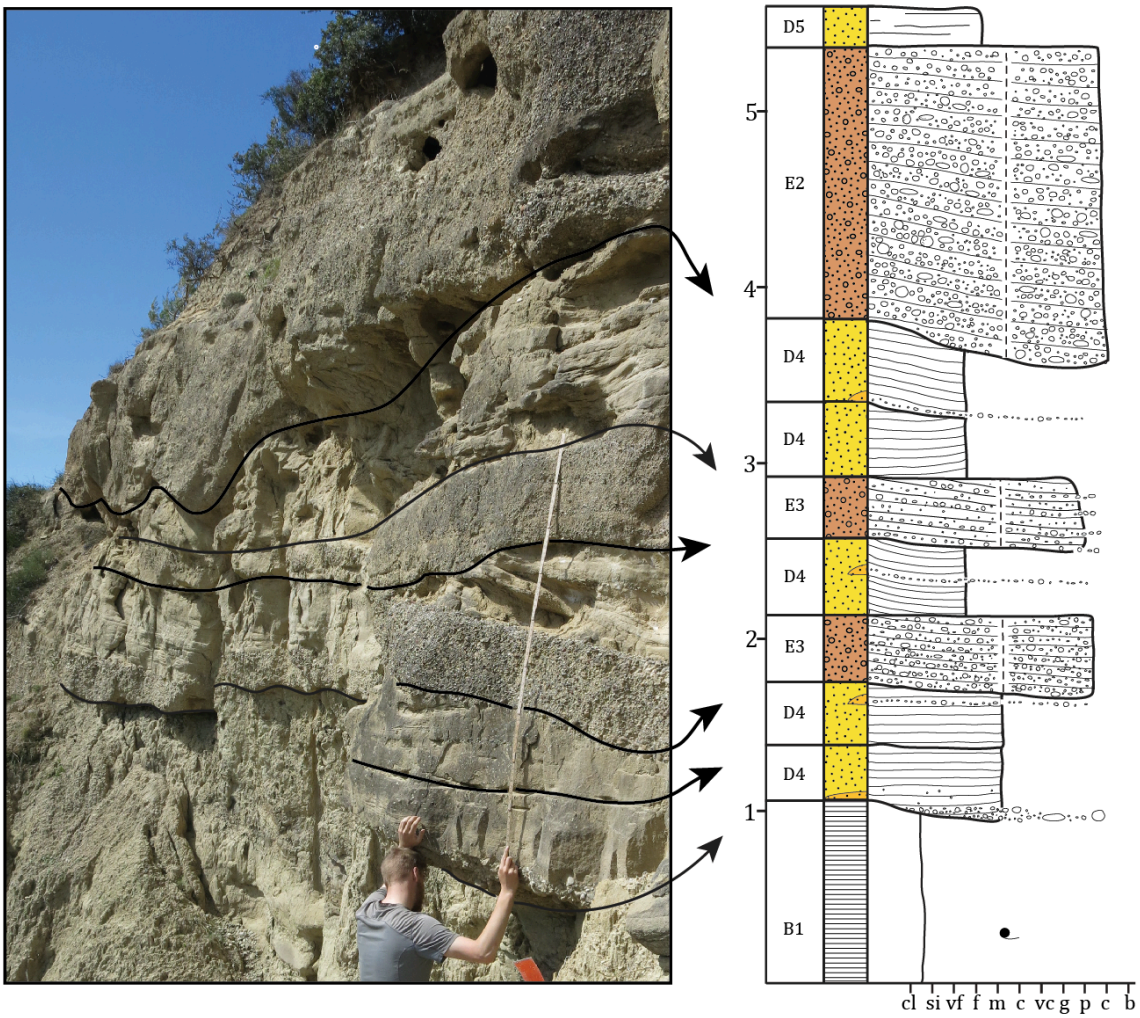

Figure 4.8: Large-scale complex ribbons (Architectural Element 2). Internal 3rd order elements are filled by alternating trough cross-stratified sandstone and conglomerate bedsets (Facies D4 and E3), overlain by planar cross-stratified matrix-supported conglomerates (Facies E2) and crude planar parallel stratified sandstone (Facies D5).

The juxtaposed 3rd order elements are amalgamated and range in thickness between 0.70 and 2.5 m. Internal channel storeys are individually bounded by channelized, concave and scoured bases (Figure 4.4), which range in relief between 0.3 m and 1.2 m. Individual storeys are filled with sandstone and/or conglomerates with occasional sandstone lenses (Figures 4.8 and 4.9). The lowest segments are often filled with conglomerates and occasional sandstone, subsequently overlain by sandstone or conglomerate storeys (Figure 4.7 and 4.8). The internal 2nd order elements are predominantly filled with amalgamated coarse-tail normal graded or ungraded conglomerates with various internal structures: low-angle planar cross stratification (Facies E1), planar-cross stratification

(Facies E2) and trough cross-stratification (Facies E3). Sand-prone deposits are frequently found in the uppermost 3rd order elements (Figure 4.9A and B).

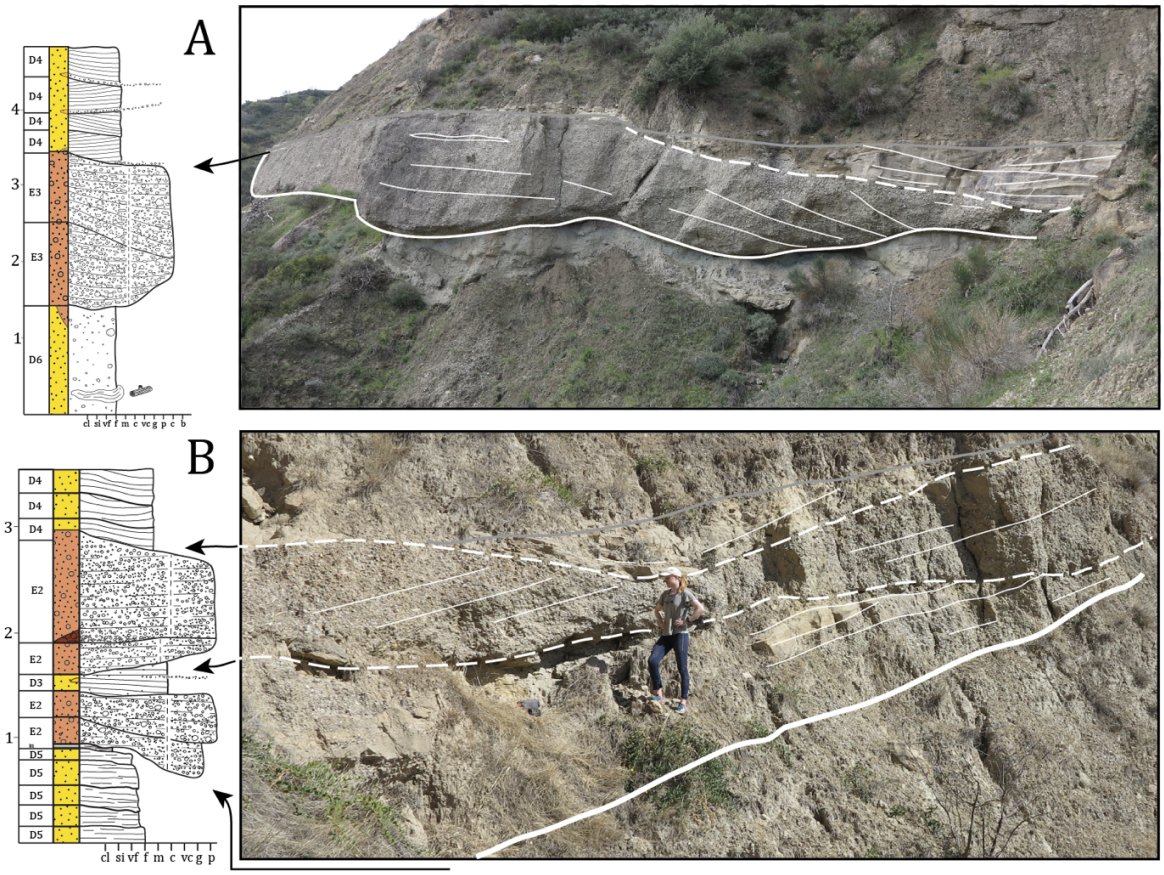

Figure 4.9: Large-scale complex ribbons (Architectural Element 2). ***A)*** *Trough cross-stratified conglomerates (Facies E3) eroding down into thick beds of structureless sandstone (Facies D6), and overlain by trough cross-stratified sandstone (Facies D4).* ***B)*** *Field photography with complex cross cutting planar cross-stratified conglomerates (Facies E2), overlain by trough cross-stratified sandstone beds (Facies D4).*

Large-scale inclined surfaces developed in Facies D3, E1, E2 and E3 dip between 4° and 25°, and are crudely shallowing upwards within individual channel storeys. Individual conglomerate beds are up to 1.3 m thick and consist of matrix- and occasional clast-supported conglomerates The conglomerate beds contain bed aligned, rounded to subrounded granule- to cobble-sized clasts, with the longest axes seldom exceeding 10 cm. The largest clasts can be randomly distributed, but are predominantly found in the lower part of each conglomerate storey. Both matrix- and clast-supported conglomerates display coarse-tail normal grading combined with an upwards increase in matrix volume.

Fine- to coarse-grained sandstone beds range between 0.15 and 0.6 m in thickness and occasionally contain shell and coal fragments. These beds are either structureless with occasional normal grading (Facies D6), or display internal structures such as low-angle planar cross stratification (Facies D3), trough cross stratification (Facies D4) and crude planar parallel stratification (Facies D5). The thickest sand-prone storeys are commonly filled by trough cross-stratified (Facies D4) or alternating crude planar parallel stratified sandstones (Facies D5), with granule- to pebble-lags. Sand-prone storeys are frequently occurring as the middle- or uppermost 3rd order elements, which reach a thickness of 1.5 m. The sand-prone storeys are frequently filled with planar to subhorizontal beds. Internal medium- to fine-grained planar cross-stratified sandstone lenses (Facies D3) are frequently alternating with conglomerate beds in the upper part of individual channel-storeys. These beds range in thickness from 0.05 to 0.30 m. The sandstone lenses extend laterally for less than 15 m, and are bounded by a grain size transitional or planar base, and a planar or eroded top.

Marlstone (Facies A1) and structureless mudstone (Facies B1) beds of 0.1 to 0.2 m are occasionally present between channel storeys, or capping the Large-scale complex ribbons. Large-scale complex ribbons are scouring down into thick successions of planar parallel stratified or structureless sandstone sheets (Architectural Element 9), sandy heterolithics (Architectural Element 10) and mudstone deposits (Architectural Element 11). Large-scale complex ribbons are distributed laterally adjacent to Large-scale complex U-shaped elements (Architectural Element 3), Large-scale simple ribbons (Architectural Element 4), Small-scale simple U-shaped elements (Architectural Element 5), and Small-scale simple ribbons (Architectural Element 6). No signs of bioturbation are observed in Architectural Element 2.

Interpretation

The external ribbon-shaped geometry, large-scale inclined surfaces, combined with the absence of levee deposits, suggest the Large-scale complex ribbons to be of non-levéed, sinuous, and meandering channel origin. Similar facies assemblages were found within the Large-scale complex sheets (Architectural Element 1), however, Large-scale complex ribbons differ by i) having winged, relatively steep dipping margins, ii) dominated by

vertically stacked channels, iii) displaying a main basal erosion surface, and iv) having a lower *W/T* ratio. These factors suggest Large-scale complex ribbons to be generated by multiple events of high-energy turbidity flows, that were laterally restricted, filled by constrained sinuous channels which delevoped lateral accretion packages.

The erosive features bounded to the 4th and 3rd order elements are indicative for the flow velocity scouring the channel bases, as well as the substratum's degree of resistance to erosion (*e.g.* Amy *et al.*, 2004; Hubbard *et al.*, 2014). The local stepped erosive profiles of the Large-scale complex ribbons suggest significant phases of erosion and insufficient time for channel smoothening, indicating rapid deposition after scouring (*e.g.* Hickson and Lowe, 2002; Kane *et al.*, 2009; Janocko *et al.*, 2011). Stacked internal channels reflect several phases of incision and deposition, including times of channel shutdown. Marlstone (A1) and mudstone (B1) are found enclosed by channel bodies, suggesting periods of channel shutdown, dominated by dilute low-density turbidity currents combined with hemipelagic and pelagic suspension settling.

Stratified normal graded conglomerate and sandstone beds suggests layer by layer deposition from sustained, to quasi-steady high- and low-density turbidity currents (*e.g.* Dykstra and Kneller, 2009; Di Celma, 2011; Janocko and Nemec, 2011; Janocko *et al.*, 2011). Bed aligned conglomerate clasts, combined with the general absence of fine-grained material, suggest tractional bedload transport and reworking, whereby high quantities of finer-grained material was bypassing at the time of deposition (*e.g.* Kane *et al.*, 2009). Ungraded sandstone and conglomerate deposits suggest rapid deposition caused by high rates of sedimentation (Lowe, 1982).

4.3.3 AE3: Large-scale complex U-shaped elements

Description

Architectural Element 3 comprise some of the less frequently occurring channelized features within the study area. They are distributed randomly, but are more abundant towards the upper 150 m of the Pellini Member. Large-scale complex U-shaped elements are defined as symmetrical and occasionally asymmetrical 4th order elements, bounded by steeply dipping margins of 35° to 60° (Figure 4.10). These asymmetrical and symmetrical channel complexes comprise coarse-grained winged margins. Large-scale complex U-shaped elements are ranging in thickness from 3.4 to 9 m, in width from 11 to 39 m, displaying a *W/T* ratio seldom exceeding 4. Large-scale complex U-shaped elements are bounded by an erosive base, ranging in relief between 1.5 and 4 m. The top of the U-shaped channel complex is frequently displaying a crude convex appearance.

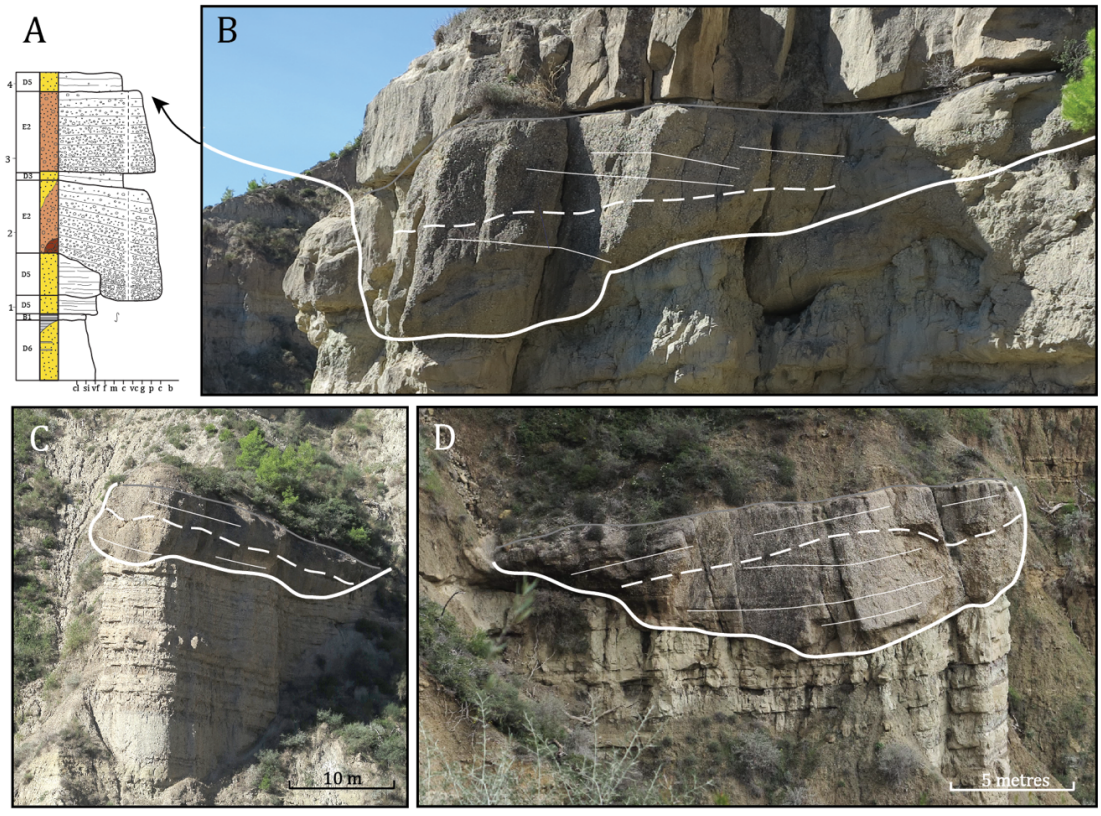

Figure 4.10: Large-scale complex U-shaped elements (Architectural Element 3). ***A)*** *Logged section of the channel body depicted in field photograph* ***B.*** ***B)*** *Normal graded large-scale planar cross-stratified matrix-supported conglomerates (Facies E2) and low-angle planar cross-stratified sandstone lenses (Facies D3) overlain by crude planar parallel stratified sandstone (Facies D5).* ***C)*** *Seven m thick Large-scale complex U-shaped channel filled by planar cross-stratified conglomerates (Facies E2).* ***D)*** *Six m thick Large-scale complex*

U-shaped channel filled with planar cross-stratified conglomerates (Facies E2) and trough cross-stratified conglomerates (Facies E3). Dashed lines represent the erosive surface between internal channel storeys.

Large-scale complex U-shaped elements comprise two vertically stacked internal segments, separated by an erosive surface (Figure 4.10). Individual 3rd order storeys range between 1.1 and 5 m in thickness, and are filled by coarse-tail normal graded clast- and matrix-supported conglomerates, with structures like planar cross-stratification (Facies E2), and trough cross-stratification (Facies E3). The conglomerate beds are amalgamated and dominated by rounded to subrounded clasts with a diametre ranging from 2.5 to 3.5 cm. Larger clasts, up to 7 cm, are abundant in the basal region of the individual channel storeys. The matrix-supported conglomerate beds display bed aligned clasts. Conglomerate beds are frequently alternating with grain size transitional low-angle planar cross-stratified sandstone lenses (Facies D3). The upper part of individual channel storeys comprise a sand-prone section of crude planar parallel stratification (Facies D5; Figure 4.10A and B). Clast-supported conglomerates are restricted to the lowermost beds within internal channel storeys (Figure 4.10A).

Large-scale complex U-shaped elements, cut down into successions of thickening-upwards sandstone sheets (Architectural Element 9) and fine-grained mudstone deposits (Architectural Element 11), immediately overlain by thin- to medium-bedded sandstone sheets (Architectural Element 9), and mudstone deposits (Architectural Element 11). Architectural Element 5 is frequently recorded laterally adjacent to Large- and small-scale channels (Architectural Elements (1, 2, 4, 6, and 7) Organic material and bioturbation was not found in Architectural Element 3 deposits.

Interpretation

Based on the external U-shaped geometry, steeply dipping symmetrical channel banks, internal facies assemblage, combined with the absence of lateral accretion packages, Architectural Element 3 is interpreted to be of a non-meandering channel origin (*sensu* Gibling, 2006). The large-scale complex U-shaped channels suggest its planform geometry to be generated by extensive incision of multiple or pulsating high-energy turbidity currents. Cohesive channel banks are more resistant to erosion relative to cohesionless sandstone and conglomerates, which limits lateral erosion of the bypassing turbidity flows. The degree of channel bank confinement is an important factor controlling the channels' planform development (Janocko and Nemec, 2011; *and references therein*). An alternative interpretation suggests initial vertical incision creating a narrow and deep channel, which failed to get progressively wider due to rapid abandonment caused by high sedimentation rate, combined with high bank strength, generating channel aggradation and subsequent avulsion.

Vertically stacked internal storeys reflect multiple events of incision and deposition of stratified sandstone and conglomerates (Facies D3, D5, E2 and E3), suggesting deposition from multiple and/or pulsating events of high and low-density turbidity currents (*e.g.* Lowe, 1982; Kane *et al.*, 2009). Conglomerate bed grading into a sand-prone upper division, suggests deposition by a tractive and waning high-density turbidity current (Lowe, 1982; Kneller, 1995). The absence of lateral accretion packages and the occurrence of convex tops suggests the channel fill to be dominated by vertical accretion of dunes and bars, creating mounded morphologies.

4.3.4 AE4: Large-scale simple ribbons

Description

Architectural Element 4 is characterized as a single-storey channel element with a cross-sectional asymmetrical geometry bounded by a coarse-grained winged margin. These bodies are defined as 4th order elements, bounded by an irregular or planar top and an erosive stepped relief between 0.3 and 4 m. The main basal erosion surface ranges between 3.2 and 8.4 m in thickness and between 18 and 75 m in width, expressing a *W/T* ratio of 5 to 10, occasionally up to 24. The ribbons' internal geometry comprises a simple channel fill, dominated by amalgamated large-scale inclined beds dipping 6° to 19° perpendicular to the channel thalweg. The large-scale inclined surfaces are similar to those in Architectural Element 1 and 2. Large-scale inclined surfaces are developed in 0.2 to 1.5 m thick beds of normal graded or ungraded fine to coarse-grained clast and matrix-supported conglomerate, pebbly sandstone and sandstone (Figures 11B and 12B). These beds are stacked, forming up to 2.3 m thick amalgamated bedsets which display an overall grain size fining- and thinning-upwards trend (Figure 4.11).

Large-scale inclined conglomerate and sandstone beds display various internal structures: low-angle planar cross-stratification (Facies D3 and E1), crude planar and planar cross-stratification (Facies D5 and E2), and structureless sandstone (Facies D6). The upper section is commonly filled by less than 1 m thick subhorizontal beds of low-angle planar cross-stratified medium sandstone (Facies D3), trough cross-stratified fine-grained sandstone with pebble-lags (Facies D4) and crude planar parallel stratified sandstone (Facies D5; Figures 4.11B and 4.12B).

Clast-supported conglomerates are concentrated at the basal portion of the ribbons, exhibiting planar parallel stratification, grading upwards into matrix-supported conglomerate with an upper sand-prone region, similar to the ones found within Architectural Elements 2 and 3 (Figure 4.11B). The conglomerates are dominated by rounded to subrounded clasts with a diameter of 3 to 4 cm. Larger clasts up to 8 cm are abundant in the basal part of the succession. The matrix-supported conglomerate beds are coarse tail normal graded and display bed aligned clasts parallel to the inclined surfaces.

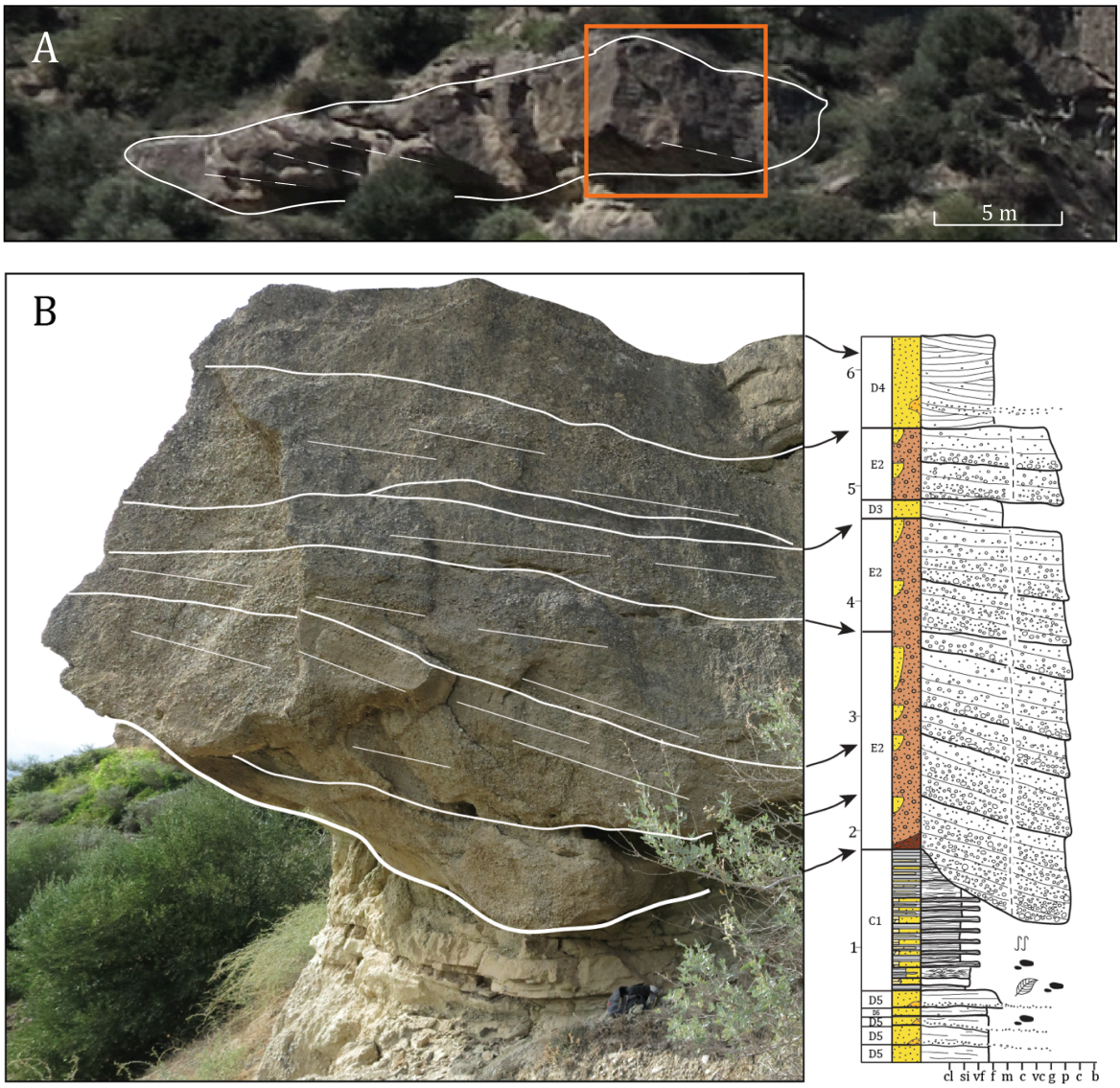

Figure 4.11: Large-scale simple ribbon (Architectural Element 4). ***A)*** *Field photograph of a Large-scale simple ribbon. Red square shows approximate position of* ***B. B)*** *Log section from the channel body depicted in field photograph* ***A*** *of coarse tail normal graded planar cross-stratified conglomerate bedsets (Facies E2) with internal lenses of low-angle planar cross-stratified sandstone (Facies D3) overlain by subhorizontal beds of trough cross-stratified sandstone (Facies D4). This channel is eroded into heterolithic deposits (Architectural Element 11).*

The large-scale inclined surfaces have sharp erosional bases and sharp tops. Bedsets frequently display an upward decrease in inclination of the large-scale inclined conglomerate and sandstone beds. Isolated 0.15 to 0.6 m thick sandstone lenses are frequently displaying low-angle cross-stratification (Facies D3), crude planar parallel stratification (D5) and structureless, crudely normal graded sandstone (D6).

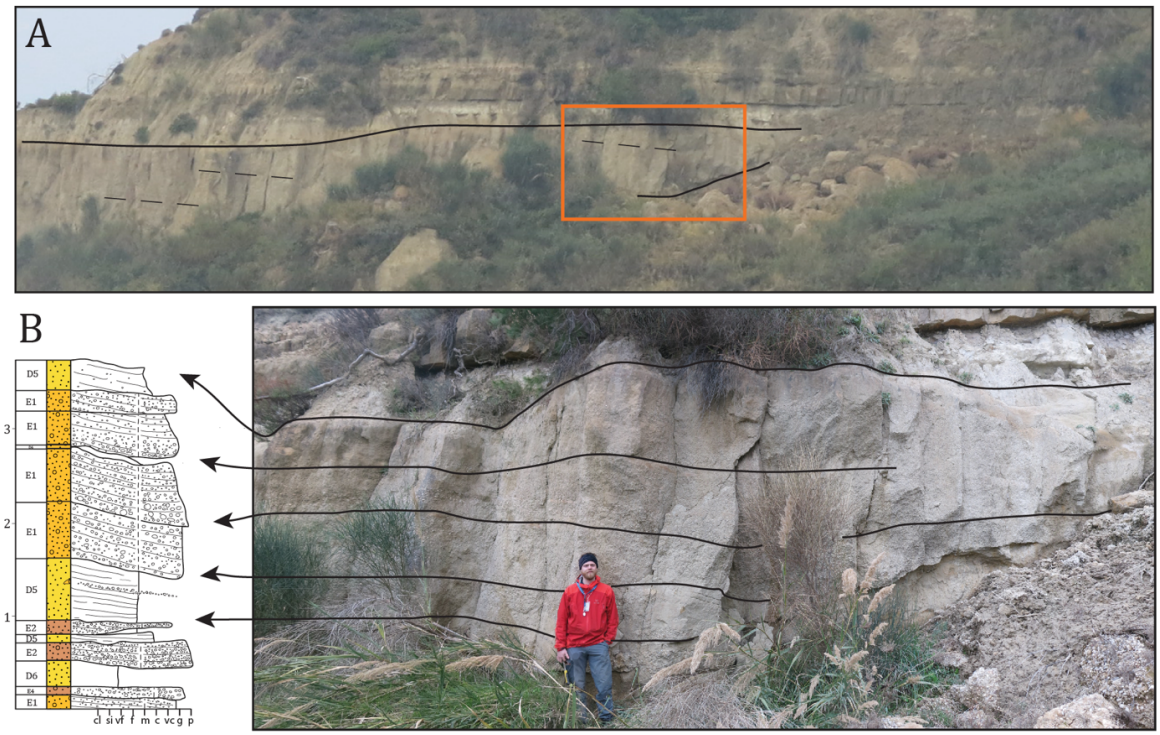

Figure 4.12: Large-scale simple ribbon (Architectural Element 4). ***A)*** *Outcrop view of a Large-scale simple ribbon (Architectural Element 4). Red square shows approximate position of* ***B. B)*** *Log section from the channel body depicted in field photograph* ***A*** *of planar cross-stratified matrix-supported conglomerate (Facies E2) and pebbly sandstone bedsets (Facies E1), alternating with crude planar parallel stratified sandstone (Facies D5).*

These lenses are distributed in the middle and uppermost division of the channel fill (Figures 4.10B and 4.11B), alternating with conglomerate bedsets similar to those in Architectural Elements 2 and 3. The lenses have a lateral extent of less than 4 m and are bounded by a planar or grain size transitional base and a planar or eroded top. Large-scale complex channels and simple channels (Architectural Elements 1, 2, 3, 5 and 6) are frequently recorded under 50 m adjacent to Architectural Element 4. Large-scale simple channels are both eroding into and overlain by conglomerate and sandstone sheets (Architectural Element 9), sandy heterolithics (Architectural Element 10; Figure 4.11B) and mudstone deposits (Architectural Element 11). No traces of bioturbation or organic material are found among Architectural Element 4 deposits.

Interpretation

Based on its external ribbon-shaped geometry, the development of amalgamated large-scale inclined bedsets perpendicular to the main channel orientation, and the fact that the ribbons are enchased in sandy and heterolithic interchannel deposits, suggest Architectural Element 4 to be of meandering channel origin (*e.g.* Abreu *et al.*, 2003). Large-scale inclined bedsets evidence channel meandering, developed by cutbank erosion of the outer-bend and simultaneous deposition on the inner-channel bend (Figure 4.13; *e.g.* Gibling, 2006; Janocko and Nemec, 2011). Sinuous and meandering channels suggest them to be close to their equilibrium profile (Janocko and Nemec, 2011). These bedsets are similar to the epsilon cross-bedding of Allen (1963) and are defined as lateral accretion packages (Abreu *et al.*, 2003).

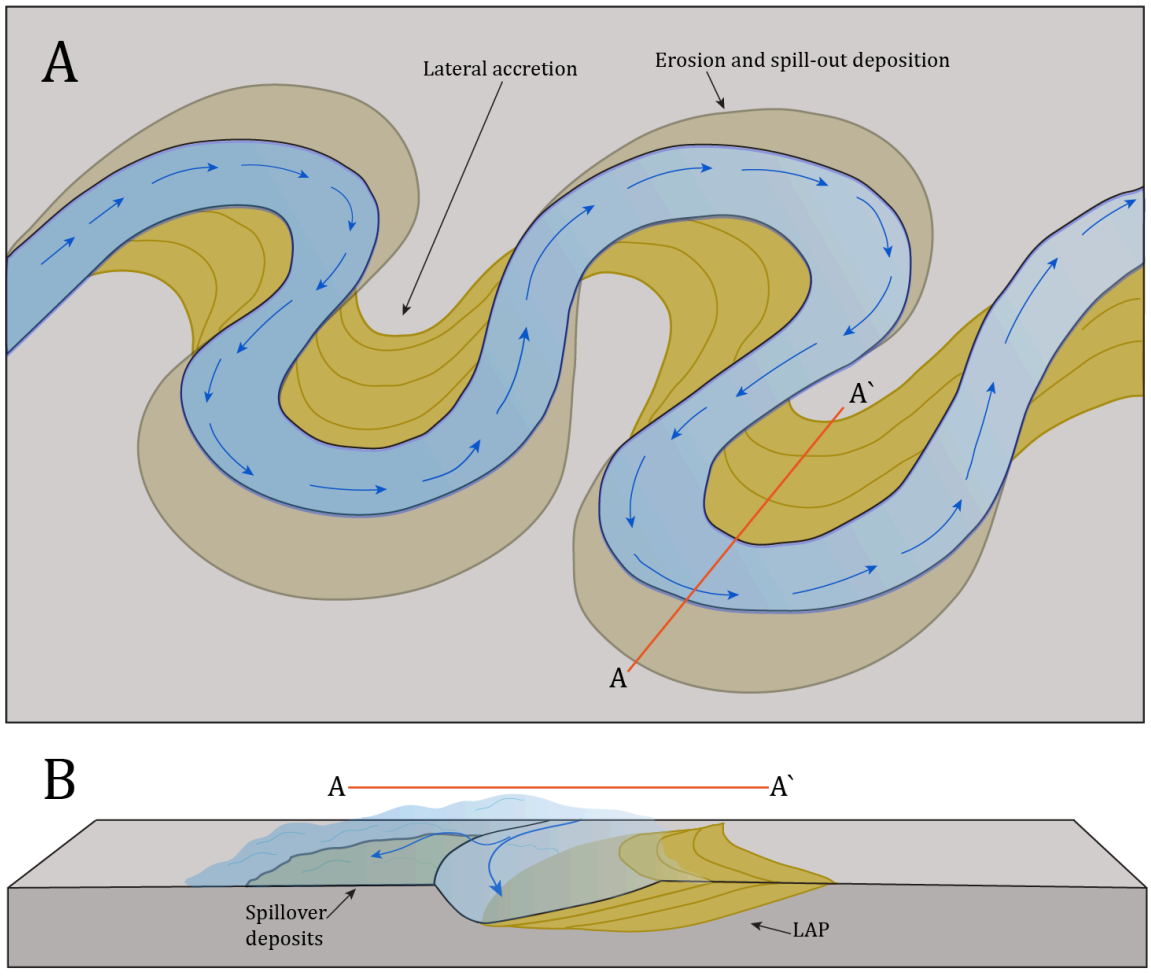

*Figure 4.13: **A**) Meandering channel belt, arrows indicate flow direction. **B**) Block diagram illustrating lateral accretion and spillover deposits in cross-section A-A`. LAP = Lateral accretion packages deposited in the inner-channel bend, whereas spillover deposits are accumulating on the outer bend.*

Lateral accretion packages developed in normal graded planar cross-stratified matrix-supported conglomerate (Facies E2) with an upper sand-prone division are similar to those described in Architectural Element 2 and 3, suggesting them to correspond to a single sedimentation unit (*e.g.* Dykstra and Kneller, 2009; Di Celma, 2011; Janocko and Nemec, 2011; Janocko *et al.*, 2011). Stratified and graded sandstone lenses (Facies D3 and Facies D4) represent tractive deposition from waning low-density turbidity currents (Lowe, 1982; Kneller, 1995). Structureless sandstone lenses (Facies D6) suggest rapid deposition by a high-density turbidity current (*e.g.* Janocko *et al.*, 2011; Talling *et al.*, 2012) or aggradational deposition by sustained steady turbidity flow (*e.g.* Kneller and Branney, 1995). The abundance of bed aligned granule- to pebble-sized clasts are indicative for tractive turbidity currents, whereby large volumes of finer-grained material bypassed as suspended load during the time of deposition. The uppermost subhorizontal and stratified sandstone beds (Facies D3, D4 and D5) represent the last stage of channel fill deposition from waning low-density turbidity currents when erosion has ceased and sedimentation prevails. As for Architectural Element 1, 2 and 3, overlying beds of mudstone deposits suggest abandonment due to abrupt upstream avulsion or channel abandonment as the channel was filled up.

4.3.5 AE5: Small-scale simple U-shaped elements

Descriptions

Architectural Element 5 is characterized by its symmetrical, cross-sectional U-shaped geometry, bounded by steeply inclined margins of 30° to 60° (Figure 4.14). Small-scale simple U-shaped elements range in width from 2.4 to 12 m and in thickness from 1.3 to 3.7 m, with a *W/T* ratio rarely exceeding 3. Architectural Element 5 is defined as 3rd order element, bounded by a plane or stepped erosional base, with a planar or weakly convex top (Figure 4.14). Stepped erosive bases are commonly found within the thickest and widest U-shaped segments, ranging between 0.10 to 0.40, relative to the smallest entities which are frequently characterized as true isolated channels with an erosional relief between 1.2 to 3 m. Small-scale simple U-shaped elements are filled by 0.30 to 2 m thick crudely normal graded or ungraded beds of trough cross-stratified sandstone (Facies D4), crudely planar parallel sandstone (Facies D5) and low-angle cross-stratified pebbly

sandstone (Facies E1). Architectural Element 6 is scour into, and are overlain by non-channelized, crudely planar parallel stratified or structureless sandstone deposits (Architectural Element 9), sandy heterolithics (Architectural Element 10) and massive mudstone successions (Architectural Element 11). Small-scale simple U-shaped elements are frequently distributed laterally adjacent to large-scale single- and multi-storey channels (Architectural Element 2, 3 and 4) and Small-scale channels (Architectural Element 6), frequently oriented oblique to the larger scale channels. These Small-scale channels are also distributed laterally adjacent to each other on the same bedding surface. No signs of bioturbation are observed in Architectural Element 5.

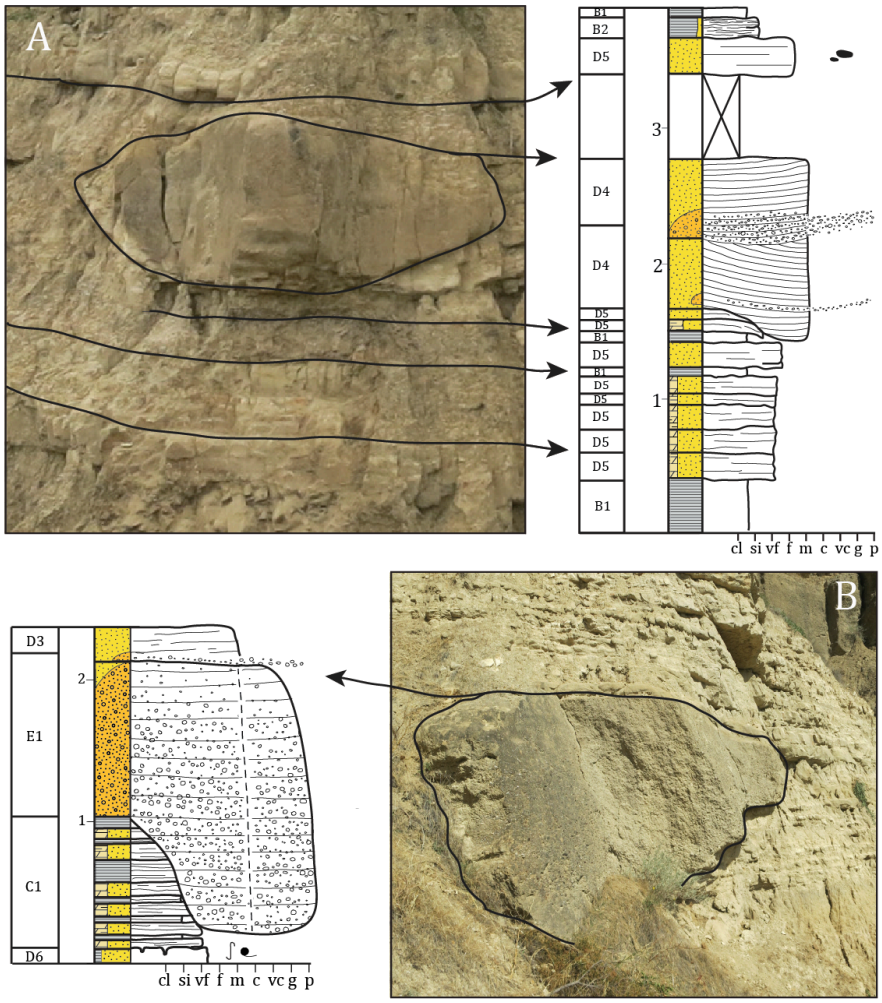

Figure 4.14: Small-scale simple U-shaped elements (Architectural Element 5). ***A)*** *Trough cross-stratified sandstone with pebble-lags (Facies D4) eroding into alternating succession of fine-grained sandstone and mudstone deposits (Architectural Element 9), with an erosional relief of 1.10 m.* ***B)*** *Low-angle planar cross-stratified pebbly sandstone (Facies E1) stepped erosional relief cutting into heterolithic deposits (Architectural Element 11).*

Interpretation

Based on the external U- shaped geometry, low *W/T* ratio, simple fill of traction-generated deposits and the absence of lateral accretion packages, Architectural Element 5 is interpreted as a non-meandering channel. The channels size and shape, combined with their simple fill, suggests that these channels to have a shorter lifespan than large-scale channels and channel complexes." (Architectural Elements 1 to 4).

Normal graded and stratified sandstone (Facies D4 and D5) pebbly sandstone (Facies E1) and conglomerate (Facies E2) represent deposition from tractive and waning high-density turbidity currents (Lowe, 1982; Kneller, 1995). Its steeply inclined margins and spatial distribution among heterolithics and mudstone deposits, suggest stable channel banks. As previously described for Architectural Elements 1 and 2, stepped erosive bases scouring into adjacent finer-grained deposits suggest a period of substantial erosion, followed by rapid deposition, which prevent the margins from being smoothened by following turbidity flows (*e.g.* Hickson and Lowe, 2002; Kane *et al.*, 2009; Janocko *et al.*, 2011).

The fact that Architectural element 5 is distributed adjacent to one another at the same bedding surface, as well as laterally adjacent to sinuous and meandering channels, suggest Small-scale simple U-shaped elements to be crevasse channels. Crevasse channels are formed during episodes of main channel breaching, typically occurring during overbank stages by powerful currents (Mutti, 1977). They are typically oriented obliquely to the axis of the main channel orientation within an interchannel setting (*e.g*. Zelt and Rossen, 1995). This theory is supported by Lien et al. (2003), suggesting crevasse channels to explicitly be generated outside meandering channel bends, commonly found laterally adjacent to finer grained interchannel deposits.

4.3.6 AE6: Small-scale simple ribbons

Description

Small-scale simple ribbons (Architectural Element 6) are some of the most frequently recorded channelized elements within the Pellini Member. They are distributed within the whole study area, being slightly predominant in the northeastern exposures (Area E). Small-scale simple ribbons are characterised as symmetrical 3rd order elements, bounded by well-defined channel margins, ranging in dip between 10° and 30°. Architectural Element 6 occurs as 0.8 to 3.6 m thick bodies, ranging in width between 3 and 35 m, displaying a *W/T* ratio of 5 to 11. Most of these units occur as true isolated channels, bounded by a planar or irregular top, exhibiting an erosional relief of 0.5 to 1 m. However, a slight portion of the observed units occur encased within thick sandstone sheets (Figure 4.15).

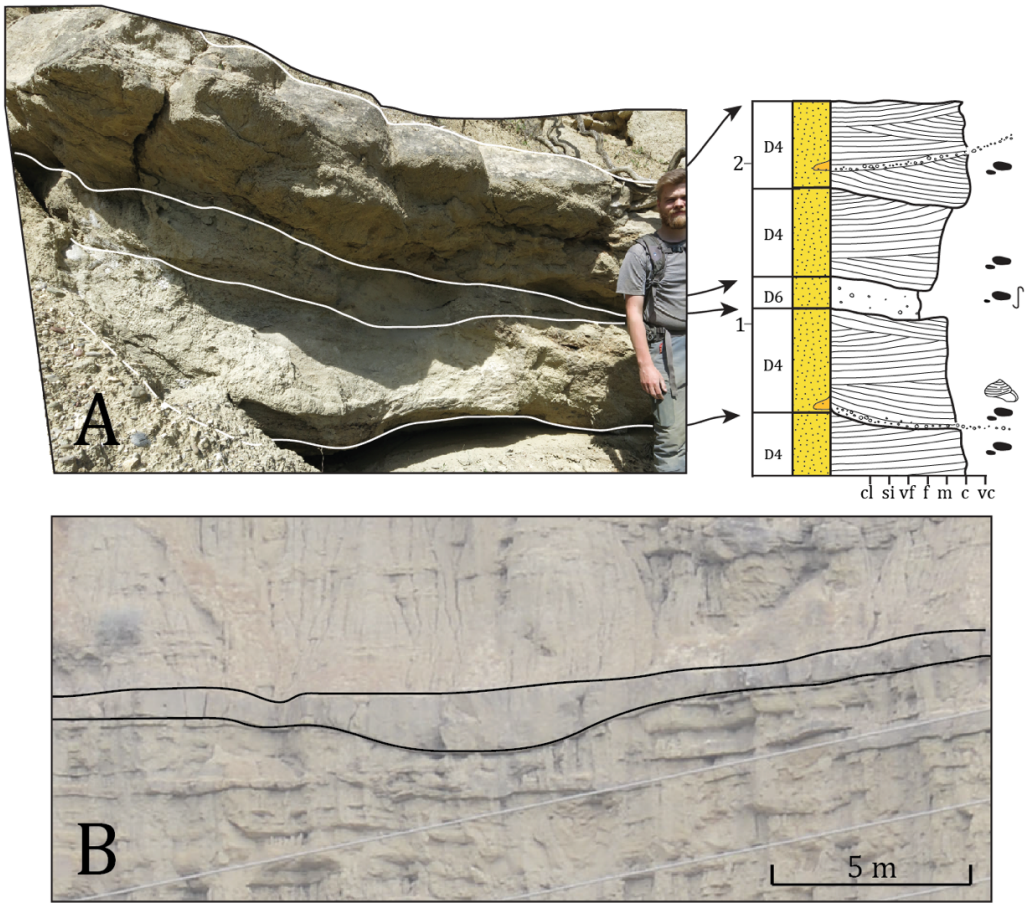

Figure 4.15: Small-scale simple ribbons (Architectural Element 6). ***A)*** *Trough cross-stratified coarse- to medium-grained sandstone with pebble-lags (Facies D4), coal and shell fragments.* ***B)*** *Outcrop view photography of a Small-scale ribbon-shaped element.*

Small-scale simple ribbons are filled by amalgamated 0.20 to 1.20 m thick structureless sandstone beds (Facies D6), normal graded or ungraded coarse to fine-grained trough cross-stratified sandstone beds with pebble-lags (Facies D4) and planar cross-stratified matrix-supported conglomerate (Facies E2; Figure 4.15). Coal and shell fragments are occasionally found within the bases of these bedsets. The erosive base cut down into non-channelized structureless and stratified sandstone sheets (Architectural Element 9) and heterolithic deposits (Architectural Element 10). As for the U-shaped channels, Ribbon-shaped units have a tendency to appear adjacent to one another on the same bedding surface and close to large- and small-scale channels (Architectural Element 1 to 7). Bioturbation was not recorded in Architectural Element 6 deposits.

Interpretation:

Based on the external ribbon-shaped geometry, *W/T* ratio, traction-generated channel fill, and the absence of lateral accretion packages, suggest Small-scale simple ribbons to be non-meandering, poorly confining channels. The internal fill of trough cross-stratified sandstone (Facies D4) and planar cross-stratified conglomerate (Facies E2) represent deposition from tractive, high-density turbidity currents, whereas structureless sandstone (Facies D6) suggest rapid deposition from high-energy turbidity currents (Lowe, 1982) . The lack of stepped erosional basal surfaces suggest single events of erosion filled by pulsating and/or multiple single flows of depositional character.

These elements differ from Small-scale simple U-shaped channels (Architectural Element 5) in terms of external geometry, *W/T* ratio, and erosional signature. However, they are both small-scale elements, relative to Architectural Element 1 to 4, filled by sand and conglomerate deposited by tractive turbidity currents, frequently cutting down into sandstone beds or heterolithic successions. This suggest Small-scale simple ribbons to be generated by similar processes as Small-scale simple U-shaped elements, whereby the planar geometry differs due to its position relative to the breached channel banks. Progressive widening and narrowing occurs as the crevassing channel goes from being confined to unconfined in an interchannel setting (Figure 5.8).

4.3.7 AE7: Small-scale simple ribbon-sheets

Description

Architectural Element 7 is defined as 3rd order elements, distinguished by its extensive ribbon-sheet geometry (Figure 4.16). Small-scale simple ribbon-sheets are bounded to poorly defined, shallowly inclined margins. These ribbon-sheets have a thickness between 1.4 and 2.3 m, ranging in width from 30 to 80 m, with a *W/T* ratio of 10 to 35.

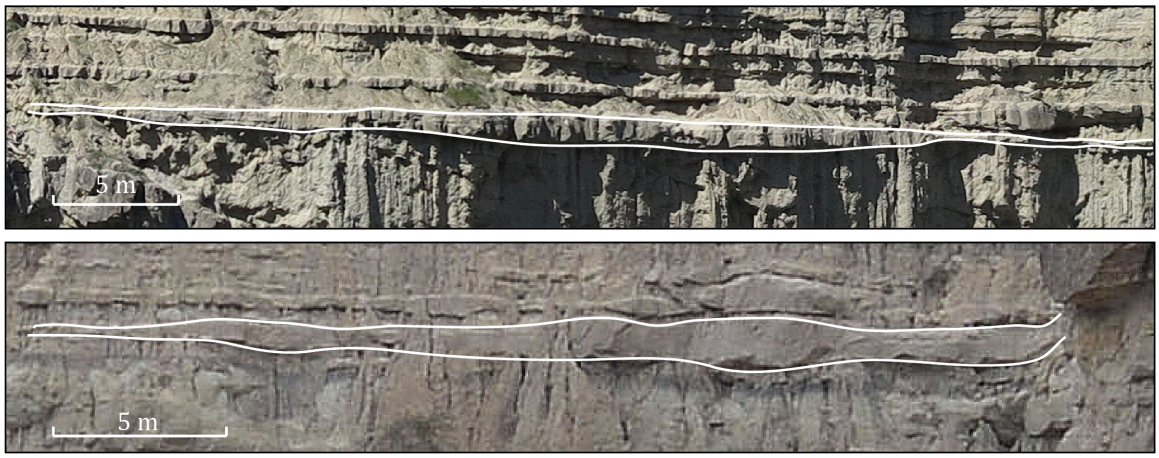

Figure 4.16: Outcrop photography of two Small-scale simple ribbon-sheets (Architectural Element 7) comprising facies group D deposits.

Small-scale simple ribbon-sheets are defined by their shallowly inclined and bilateral thinning margins, bounded by a planar top. These features have an erosive relief ranging from 1.4 to 2.3m. Scoured erosive features are frequently recorded and recognized due to the local high-erosive step, ranging from 0.3 to 0.8 m. These features are obliquely oriented to the main orientation of the ribbon-sheet. The internal facies assemblage consist of conspicuously amalgamated facies group D deposits frequently structureless (Facies D6), exhibiting crude planar parallel stratification (Facies D5). These features are similar to the unconfined medium to thick bedded sandstone sheets (Architectural Element 9), however, the occurrence of a main erosive basal surface of Small-scale simple ribbon-sheets separate them from one another. Architectural Element 6 is frequently distributed vertically and laterally adjacent to single-storey channels (Architectural Elements 4 and 5) and unconfined sandy heterolithics and mudstone deposits (Architectural Element 10 and 11). No signs of bioturbation are observed in Architectural Element 7.

Interpretation

Architectural Element 7 is interpreted as a poorly confined channelized elements based on its laterally extensive geometry, high *W/T* ratio and low erosional step relief. The amalgamated channel fill of structureless and crude planar parallel stratified sandstone suggests rapid deposition by poorly confined low- or high-density turbidity currents (*e.g.* Lowe, 1982; Janocko *et al.*, 2011; Talling *et al.*, 2012) within a wide, non- meandering channel, supported by its lack of lateral accretion packages. Its spatial relation to small and large-scale channels (Architectural Elements 4 and 5), unconfined fine-grained heterolithics and mudstone deposits (Architectural Elements 9 and 10), suggest deposition within an interchannel setting as sheet-like turbidites, also known as crevasse splays. Crevasse splays are generated from a narrow point source, such as a crevasse channel (Damuth *et al.*, 1995; Posamentier and Kolla, 2003; Arnott, 2010). The occasional high-relief scoured bases are interpreted as flute marks, generated by vortices within a turbulent flow (Nichols, 2009).

4.4 Non-Channelized elements

Non-channelized elements are characterized as unconfined depositional features, commonly displaying broad, sheet-like geometry which are laterally extensive and can be traced over hundreds of metres. The majority of these elements are dominated by fine-grained material ranging in bed thickness from centimetres- to meter-scale and are volumetrically the most significant elements within the Pellini Member. Four non-channelized elements have been distinguished within the study area: 1) Deformed large-scale complex sheets, 2) Thin to thick-bedded sandstone sheets, 3) Sandy heterolithics and 4) Mudstone with thin-bedded sandstone sheets.

4.4.1 AE8: Deformed large-scale complex sheets

Description

Deformed large-scale complex sheets are restricted to the northeasternmost part of the study outcrop at the base of the Pellini Member succession, area D (Figure 4.17A). Architectural Element 8 is characterized by its external sheet planform geometry and its internal folding and distortion. The base is covered by scree and vegetation, so no exact thickness could be measured, however, the exposed section could locally be up to 25 m thick, which makes it the thickest observed depositional feature within the study area. This feature can be laterally traced over hundreds of metres, but local faults and scree covers makes it difficult to estimate its original extent. Deformed large-scale complex sheets comprise Facies F1 deposits which constitutes matrix-supported conglomerate, fine- to medium-grained sandstone and mudstone with intercalated coal and shell fragments. Primary structures are in general poorly preserved.

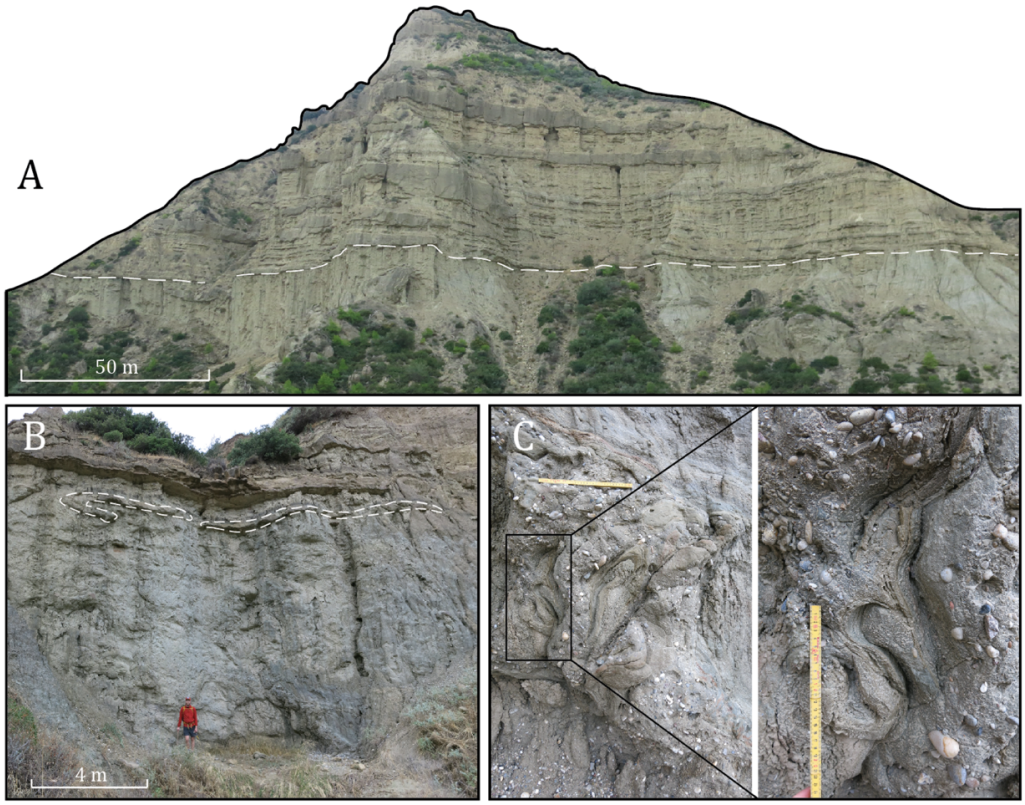

Figure 4.17: Deformed large-scale complex sheets (Architectural Element 8). ***A-B****) Outcrop photography of deformed large-scale complex sheet (Architectural Element 8), exposed within area E. Dashed line in A illustrate its upper boundary. Whereas the dashed line in B mark the brecciated and folded sandstone blocks.* ***C****) Internal deformation structures (Facies F1).*

The basal region consists of a 0.7 m thick succession of deformed planar parallel laminated mudstone (Facies B1) overlain by a 0.4 m thick inversely graded heterolithic sand-prone succession. A 3.5 m thick bedset of matrix-supported conglomerate is displayed on top of the finer-grained basal succession, which exhibit a higher degree of deformation compared to the underlying unit. The extraformational clasts are rounded to sub-rounded pebble-sized, unevenly distributed within a highly contorted and distorted strata (Figure 4.17C). The upper division is a 1.35 m thick medium- to fine-grained sandstone unit with randomly scattered pebble-sized clasts, and plant fragments. This section is less deformed than the prominently folded matrix-supported conglomerate unit. This section comprises folded and brecciated blocks of fine-grained sandstone, where its primary structures of crude planar parallel stratification are recognised (Figure 4.17B: marked by dashed line). This section defines the uppermost part of the large-scale complex sheet, abruptly overlain by 1 m thick succession of mudstone and a thick-bedded sandstone sheet.

Interpretation

Based on the external geometry, lateral and vertical extent, internal large-scale deformation structures and poorly preserved primary structures, Architectural Element 8 is interpreted as a slumped unit (Figure 4.18). Slumping is defined as a gravity induced mass-movement, activated when the sediment`s internal shear-strength is exceeded (*e.g.* Postma, 1984; Nemec, 1990) . This phenomenon can occur in various settings (*e.g.* along steep foresets of Gilbert-type deltas or canyon margins; *e.g.* Postma, 1984; Colella *et al.*, 1987; Nemec, 1990; Janocko *et al.*, 2011; Kane and Hodgson, 2011). Slope failure occurs due to high sedimentation rates, high internal pore pressure, over-steepening and/or seismic loading (Postma, 1984; Postma and Roep, 1985; Pickering *et al.*, 1986; Locat and Lee, 2002) resulting in *en masse* downslope migration, involving plastic and brittle deformation of primary structures and morphology (Colella *et al.*, 1987). The compressional deformation structures such as shear folds and thrusts suggest deceleration in slump movement. The varying degree of deformation within this slumped unit suggest that time of sediment *freezing* occurred at different stages throughout the emplacement, resulting in subsequent folding and complex internal deformation (Stow *et al.*, 1996).

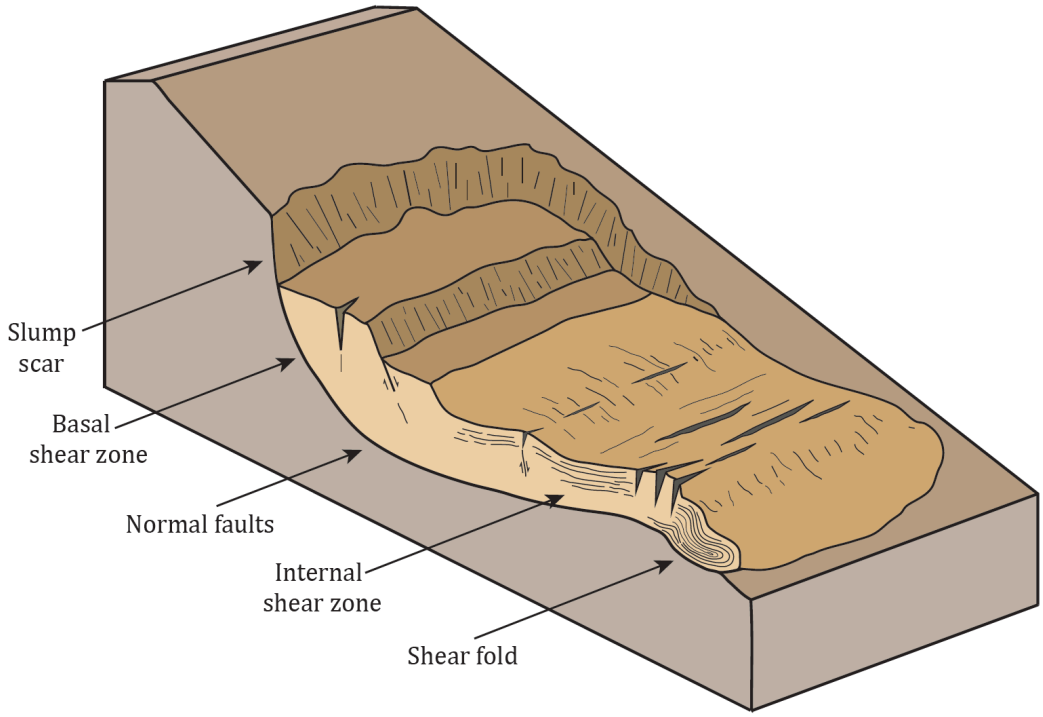

Figure 4.18: Cross sectional illustration of a slumped unit.

The slumped unit is interpreted to be much more extensive than what the outcrop reveals. However, the exposed slumped section suggests one major or several large-scale slumping events. Its internal lithological composition of mudstone, sandstone and pebbles suggest low sediment strength and stability, which results in higher degree of mobility (Colella *et al.*, 1987). The large volume of sediments will increase the internal shear stress, subsequently enhancing travel distances of the remobilized unit (Colella *et al.*, 1987).

4.4.2 AE9: Thin- to thick-bedded sandstone sheets

Description

Thin- to thick-bedded sandstone sheets (Architectural Element 9) are volumetrically the most significant elements within the Pellini Member, characterized by their lateral extensive tabular geometry. Architectural Element 9 is defined as a 3rd order element, comprising 0.5 to 10 m thick bedsets of 0.05 to 1.2 m thick beds. The facies assemblage is predominated by sandstone and subordinate marlstone, mudstone, heterolithics and conglomerate. Sandstone and conglomerate beds are frequently bounded by a straight to irregular top and an irregular or locally erosive lower boundary with an erosional relief rarely exceeding 0.2 m.

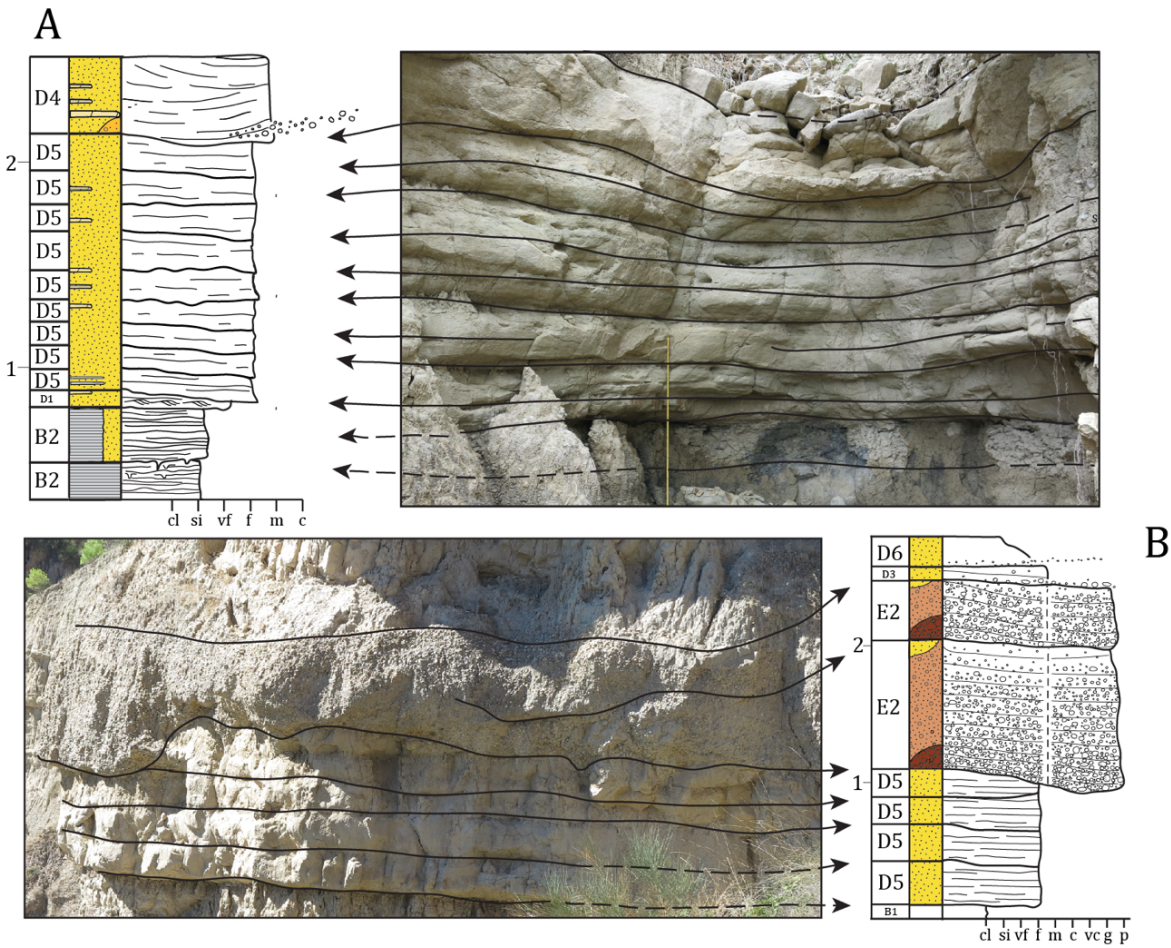

Figure 4.19: Medium to thick-bedded sandstone sheets (Architectural Element 9). ***A)*** *Amalgamated crudely planar parallel stratified sandstone sheets (Facies D5) displaying a coarsening and thickening-upwards motif.* ***B****) Planar cross-stratified conglomerate (Facies E2) eroding down into amalgamated crude planar parallel stratified sandstone sheets (Facies D5).*

Mudstone, marlstone and heterolithic deposits are bounded by a planar to transitional lower boundary and planar to eroded tops. Normal or ungraded sandstone and conglomerate frequently display a variety of structures: ripple cross-lamination (Facies D1), planar parallel lamination (Facies D2), low-angle planar cross-stratification (Facies D3, E1 and E3), trough cross-stratification (Facies D4) and crude planar parallel stratification (Facies D5). Some beds are bipartite and comprises a planar parallel stratified or massive sandstone division grading into ripple cross-laminated sandstone. Individual sandstone beds are bounded by a planar top and a planar or erosive lower boundary, which display a low erosional relief, rarely exceeding 0.05 m.

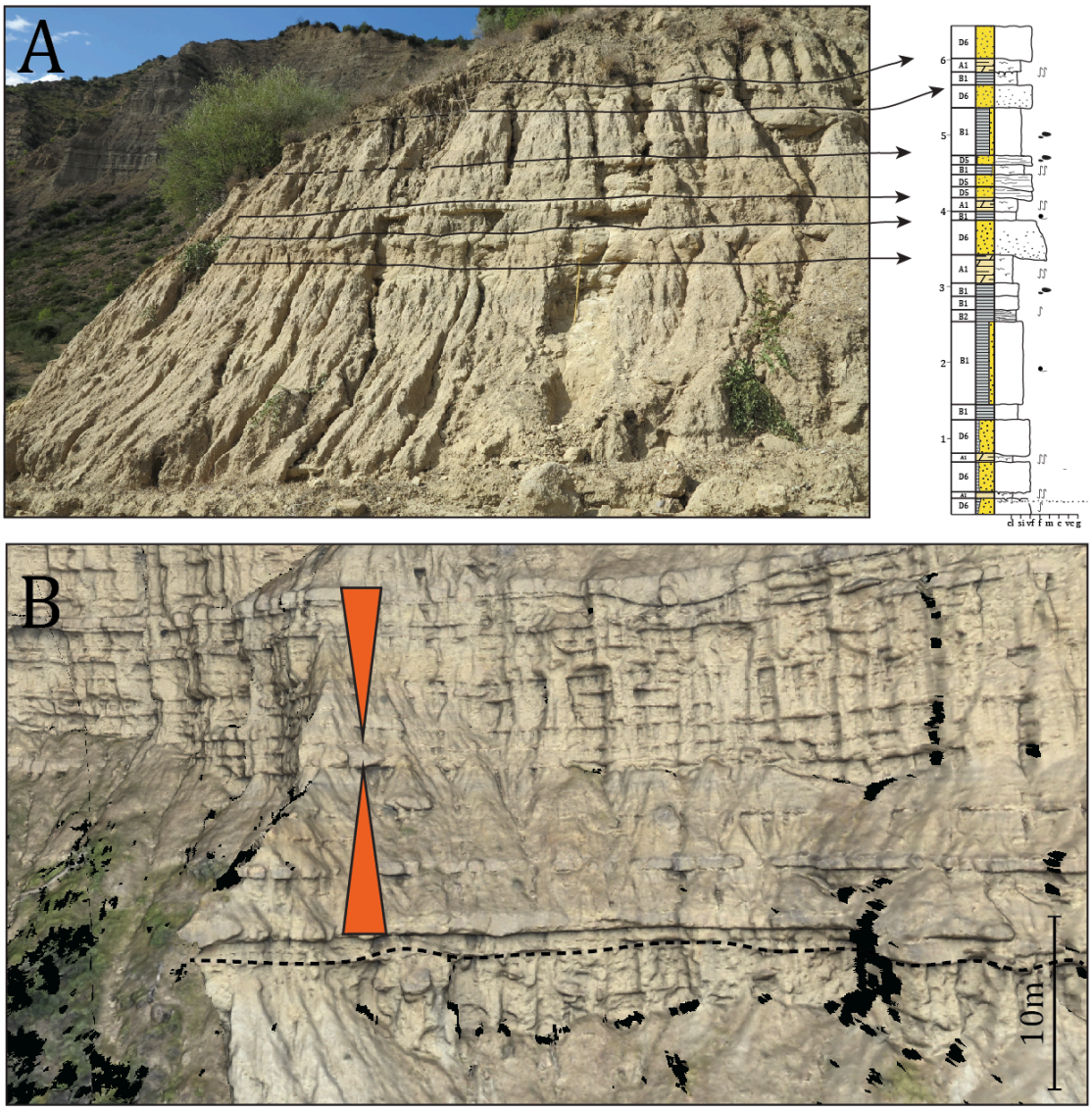

*Figure 4.20: Thin- to thick-bedded sandstone sheets (Architectural Element 9). **A)** Crude planar parallel*

stratified (Facies D5) and structureless sandstone sheets (D6) alternating with structureless marlstone (Facies A1) and mudstone (Facies B1). ***B****) Digital outcrop model view of overall thinning-upwards and thickening-upwards trend. Dashed line illustrate top of slumped section (Architectural Element 9).*

Thin- to thick-bedded sandstone sheets occur as stacked or isolated beds (Figures 4.19 and 4.20). Amalgamated sandstone beds are distinguished by subtle breaks in grain size and by non-continuous erosive surfaces (Figure 4.19A). Isolated sandstone beds occur as 0.1 to 0.8 m thick sheets, alternating with 0.05 to 0.40 m thick beds of massive or planar parallel stratified marlstone (Facies A1) mudstone (Facies B1 and B2), sandy heterolithic (Facies C1) and occasional 0.5 to 1 m thick beds of planar cross-stratified or structureless conglomerate (Facies E1, E2 and E4). The relative thickness proportion of sandstone and fine-grained marlstone and mudstone varies throughout the succession.

Overall thickening- and coarsening upwards and thinning- and fining-upwards trends frequently occur within up to 20 m thick successions of thin- to thick-bedded sandstone sheets (Figure 4.20B). Thickening- and coarsening-upwards trends are recognized from the overall upward increase in bed thickness, grains-size and erosive signature. This phenomenon occurs with a simultaneous decrease in marlstone and mudstone content. The lower part of a thickening- and coarsening-upwards succession is dominated by ripple cross-stratified sandstone (Facies D1), planar parallel stratified sandstone (Facies D2), crude planar parallel stratified sandstone (Facies D5) and occasional alternations of structureless or planar parallel stratified marlstone (Facies A1) and mudstone (Facies B1 and B2). Gradually, this succession passes upwards into graded structureless sandstone (Facies D6) with granule- to pebble-lags and up to 0.9 m thick stratified or structureless conglomerate sheets (Facies E1, E2 and E4). Thinning- and fining- upwards trends are recognized from the overall upward decrease in bed thickness, grain size, volumetric increase in marlstone and mudstone alternations (Facies A1, B1 and B2), combined with increased degree of bioturbation.

Shell fragments, leaf imprints, coal fragments and bioturbation were recorded. However, the degree of bioturbation is highly variable within Architectural Element 9 deposits. The highest degree of bioturbation is frequently occurring within finer-grained marlstone, mudstone and very-fine to fine- grained sandstone deposits. Bioturbation is not recorded within conglomerate deposits.

Interpretation

Based on the extensive tabular geometry, thickening- and coarsening-upwards and thinning- and fining- upwards trends, local scoured bases and its spatial relation to confined and unconfined depositional bodies, Architectural Element 9 is interpreted as turbidite sheet, deposits within an interchannel setting.

The lithological composition reflects its derivation from a siliceous- rich source area, whereas the sporadic marlstone deposits suggest sourcing from an exposed lime-rich bedrock, carbonate platform and/or direct chemical precipitation within the water column (*e.g.* Moxham and Eckhart, 1956; Janbu *et al.*, 2007). Stratified pebbly sandstone and conglomerate (Facies E1 and E2) suggest rapid deposition from tractive high-density turbidity currents, whereas structureless conglomerates (Facies E4) suggests rapid deposition by a sustained, quasi-steady, high-density turbidity currents. (Lowe, 1982; Kneller, 1995). These deposits are interpreted to have been transported by unconfined and partly confined turbidity flows. Partly confined turbidity flows are frequently spilling sediments out onto the overbank region, whereby a sharp channel bend can cause the entire turbidity current to flow out of the channel and into an overbank setting (*e.g.* Arnott, 2010; Janocko *et al.*, 2011). Another process that should be mentioned is flow stripping. Flow stripping is a phenomenon which separates the upper, frequently finer-grained part of the down-flowing current from the coarsest, lowermost division.

Crude planar parallel stratified sandstone (Facies D5) and structureless and normal graded sandstone (Facies D6) suggest high depositional rate, settling from suspension with no or faint bed-load traction. These sandstone sheets are interpreted to be deposited by collapsing high-density turbidity current, or aggradational sedimentation under depletive steady flow (*e.g.* Lowe, 1982; Kneller and Branney, 1995; Mastalerz, 1995; Kane *et al.*, 2009; Talling *et al.*, 2012; Pickering and Hiscott, 2015). Amalgamated sandstone successions with eroded bed tops suggest deposition from high-density turbidity currents (Lowe, 1982) where minor erosion is a result of turbulent scouring (Macauley and Hubbard, 2013). Bipartite beds with locally preserved planar and ripple cross-laminations in the upper section of massive sedimentation units are interpreted to represent tractive deposition during a final stage of low-density turbidity current (Lowe, 1982). The amalgamated, thickening- and coarsening-upwards successions suggest

aggradation and/or progradation of the depositional system or local progradation. Thinning- and fining-upwards trends reflect decrease in energy which could be due to local avulsion leading to gradual shifting of channel elements and/or lateral migration of the channels, which leads to gradual interchannel shutdown at this location. This is supported by the upwards volumetric increase of alternating marlstone and mudstone deposits.

4.4.4 AE10: Sandy heterolithics

Description

Architectural Element 10 is characterized by its extensive sheet geometry and its heterolithic facies assemblage.

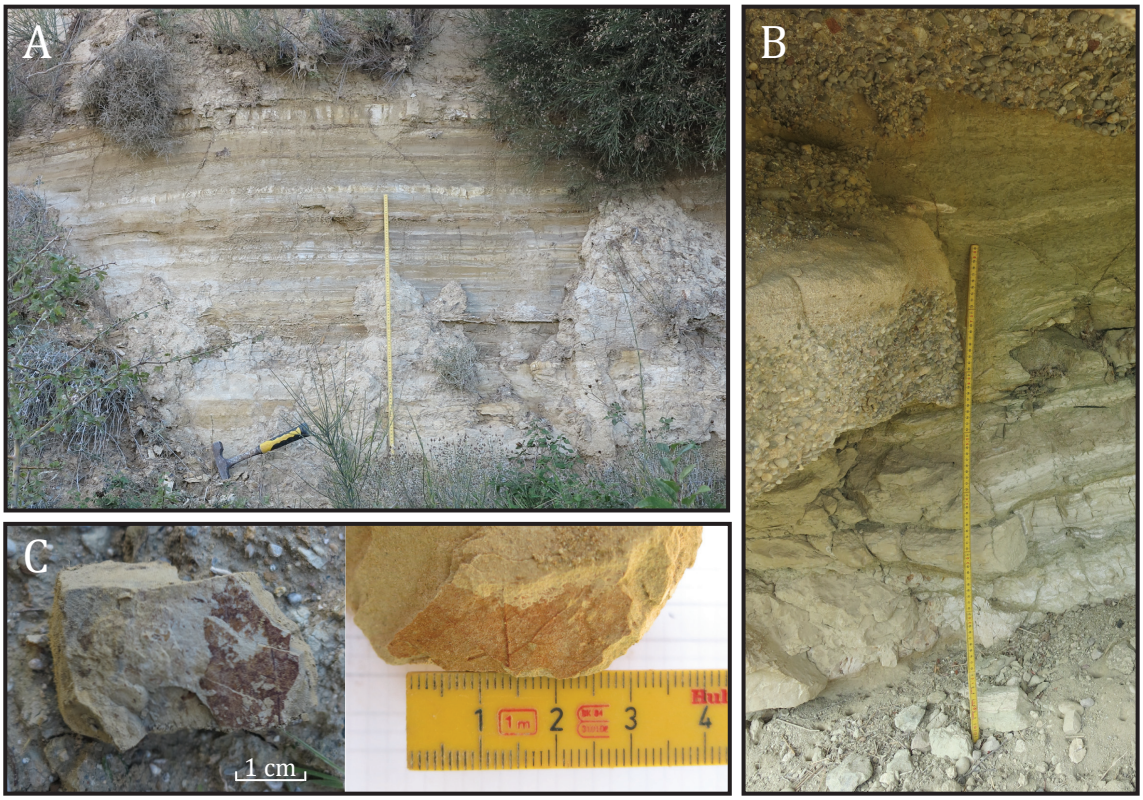

Figure 4.21: Sandy heterolithics (Architectural Element 10). ***A)*** *over 1 m thick succession of thinly bedded and laminated marlstone, mudstone, and very fine-grained sandstone (Facies C1).* ***B)*** *Heterolithic succession are frequently eroded into by channelized units.* ***C)*** *Leaf imprints.*

Sandy heterolithics is defined as a 3rd order element comprising 0.2 to 1.1 m thick successions of laminae and tabular beds, rarely exceeding 0.08 m in thickness (Figure 4.21). The internal laminae and beds bounded by mottled, planar, or grain size transitional lower and upper boundaries, are recognized by changes in colour, texture, and internal structures. Sandy heterolithics comprise normal graded or ungraded deposits of alternating white marlstone (Facies A1), dark to light grey structureless mudstone (Facies B1), dark to light grey laminated mudstone (Facies B2) and very fine- to medium-grained sandstones (Facies group D). The sandstone laminae and beds display various internal structures: ripple cross-lamination (Facies D1), planar parallel stratification (Facies D2) and crude planar parallel stratification (Facies D5) which can be up to 0.2 m thick. From outcrop to outcrop the sand to mud ratio is highly variable, predominantly occurring as mud-prone or monotonous with an equal mud to sand ratio. Architectural Element 10 displays repetitive alternations of mudstone, marlstone and sandstone laminae and beds. Sandy heterolithics are frequently eroded into by large- and small-scale channels (Architectural Elements 2, 4, 5 and 6) and thin- to thick-bedded sandstone sheets (Architectural Element 9). Sandy heterolithics display a moderate degree of bioturbation, frequently comprising organic detritus and well preserved plant imprints (Figure 4.21C).

Interpretation

Based on the heterolithic lithological assemblage, with no occurrence of internal erosive surfaces, combined with the presence of well preserved leaf imprints, the sandy heterolithics are suggested to be deposited by dilute, low-density turbidity currents such as hyperpycnal suspension plumes combined with hemipelagic and pelagic suspension settling (*e.g.* Janbu *et al.*, 2007; Pickering and Hiscott, 2015). Ripple cross-laminated sandstone (Facies D1) and planar parallel stratified sandstone (Facies D2) with overlying mudstone (Facies B1 and B2) are attributed to deposition from a tractive and waning low-density turbidity current. A sudden increase in sandstone within the vertical succession may reflect an increase in flow magnitude which enables more sand to be transported over the channel margins (*e.g.* Kneller, 1995; Janbu *et al.*, 2007). The varying proportion of sandstone and fine-grained marlstone and mudstone from outcrop to outcrop could also suggest its relative distance from the spillout conduit.

4.4.5 AE11: Mudstone with thin-bedded sandstone sheets

Description

Architectural Element 11 is characterized by its laterally extensive fine-grained facies assemblage, alternating with sparse occurrences of thin-bedded sandstone sheets (Figure 5.22).

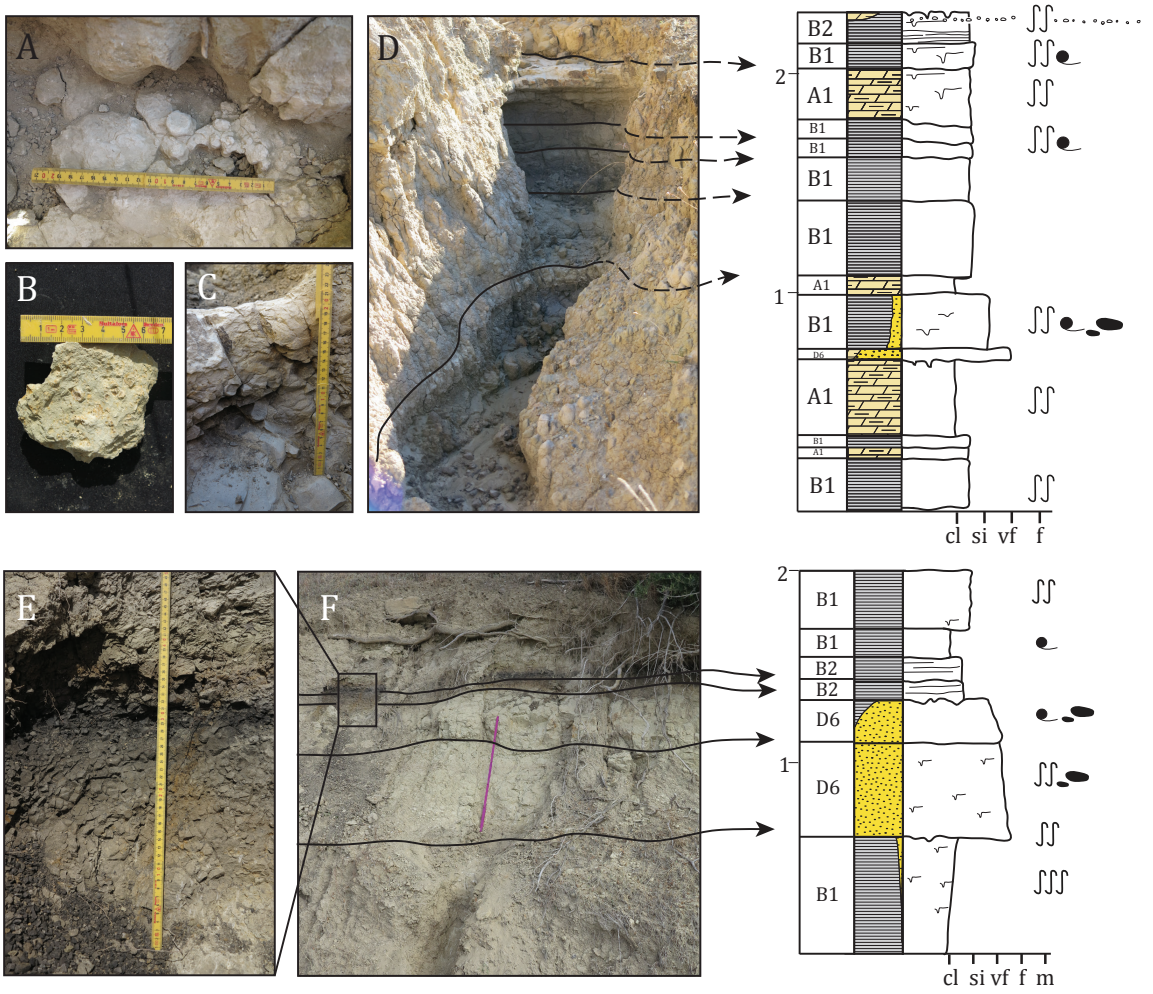

Figure 4.22: Mudstone with thin-bedded sandstone sheets (Architectural Element 11), ***A-C)*** *Mottled marlstone (Facies A1).* ***D)*** *Alternating successions of marlstone (Facies A1) and mudstone (Facies B1 and B2).* ***E-F)*** *Planar parallel laminated mudstone (Facies B2).*

Mudstone and marlstone deposits are bounded by mottled, planar, or grain size transitional lower and upper boundaries, recognized by changes in colour, grain size, and internal structures. Fine-grained material could be hard to trace over large distance due to thick semi-consolidated material covering the deposits in the outcrop section.

Architectural Element 11 comprise 0.01 to 0.5 m thick tabular beds of white marlstone (Facies A1), 0.02 to over 1 m thick grey and brown structureless mudstone (Facies B1), 0.03 to 0.7 m thick grey or brown-red planar parallel laminated mudstone beds (Facies B2) and 0.2 m thick beds of multi-coloured heterolithics (Facies C1). These units are occasionally interfingering with 0.04 m thick beds of structureless fine-grained sandstone (Facies D6). Mudstone deposits can occur as 1.5 m thick isolated beds or as bed intervals intercalating with marlstone and sandstone, ranging in thickness from 1 to 5 m. Marlstone is commonly mottled and highly bioturbated (Figure 4.22 A-C). Architectural Element 11 is frequently overlaying and eroded into by large- and small-scale channelized elements, and thin- to thick-bedded sandstone sheets (Architectural Element 9). Mudstone with thin-bedded sandstone sheets comprise moderate- to low-degree of bioturbation and contain high amounts of organic detritus, such as plant and shell fragments.

Interpretation

The fine-grained facies assemblage, sparse occurrence of sandstone deposits, the lack of erosive surfaces and its spatial relation to channels and sandstone sheets, suggest Architectural Element 11 to represent deposition in a interchannel setting, prone to experience sedimentation of fine-grained material and infrequent events of sandstone deposition. These deposits record sporadic incursions of dilute low-density turbidity currents (*e.g.* Prélat et al., 2009) within an environment dominated by pelagic and hemipelagic suspension settling (*e.g.* Kneller and Branney, 1995; Nemec, 1995; Janbu *et al.*, 2007).

5. CHANNEL ANALYSIS

5.1 Introduction

The purpose of this chapter is to reveal potential trends within the Pellini Member based on the orientation, dimension and spatial distribution of 80 channelized bodies. Width and thickness measurements of the channel bodies together with dip and dip direction of their lateral margins and erosive basal features were obtained from the digital models in VRGS. The majority of the channelized bodies are exposed in sections oblique to their depositional dip direction, yielding too large apparent widths. Individual measurements were therefore corrected to remove the effects of apparent lengthening of bodies due to oblique exposures (Fabuel-Perez *et al*., 2009). Palaeocurrent directions was measured from the erosive bases of individual channel bodies (Figures 3.1 and 4.4).

5.2 Palaeocurrent analysis

The single or multiple thalwegs of individual channelized feature is considered as a flow axis indicator, defined by its lateral bounding margins, oriented parallel to the flow direction (Nichols, 2009). The following section provide descriptions and interpretations of the bulk dataset comprising 235 palaeocurrent measurements and average palaeocurrent directions of 80 channelized bodies. Palaeocurrent data is separated according to the locality and the channelized architectural element measurements was obtained from, which provides insight into sediment transport directions.

5.2.1 The bulk dataset

Through use of the statistical methods by Kuiper, Watson and Rayleigh, it was possible to evaluate whether the bulk dataset of 235 measurements displayed a random or preferential direction. Statistical analysis of the bulk dataset reveals preferential orientation of the palaeocurrent data towards 135° (Figure 5.1A). Kuiper, Watson and Rayleigh tests indicate that the data population has a non-uniform distribution with a confidence level of 95% (Kuiper and Watson) and 99% (Rayleigh).

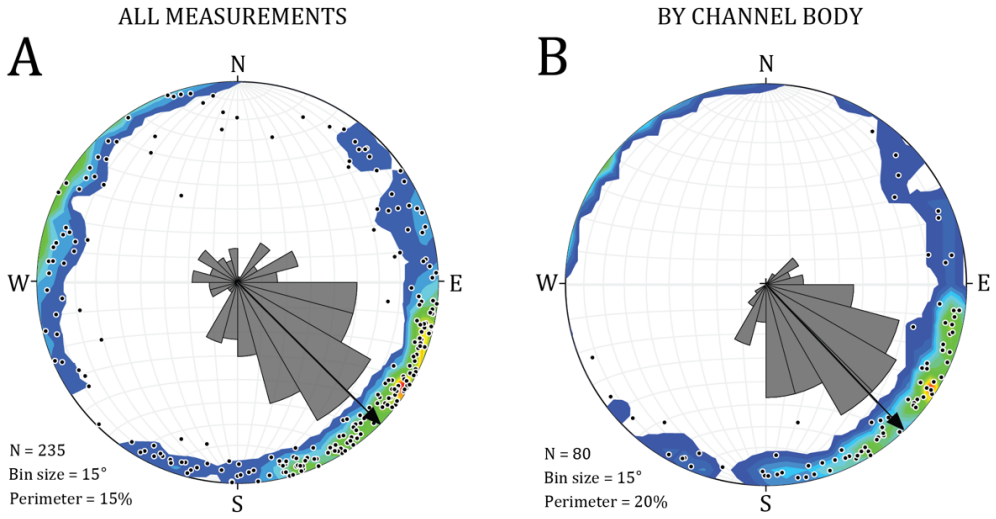

*Figure 5.1: **A**) Rose diagram of 235 palaeocurrent indicators obtained from 80 channel bodies. The arrow is directed towards the average transport direction of the bulk dataset (135°). **B**) Average palaeocurrent orientation of each of the identified channel bodies, using a binned dataset based on **A** (137°). Black dots represent individual vector directions.*

The average palaeotransport direction of the bulk dataset display a preferential orientation towards southeast (Figure 5.1). The plots show that in addition to the main, southeast oriented transport direction, a large spread of the palaeocurrent distribution occur. The measurements oriented obliquely to the main transport direction probably represent the result of sinuous and crevassing channels (*e.g.* Hubbard *et al.*, 2008). However, the 50 vectors directed in the opposed quadrant relative to the main transport direction are measurements obtained from shallowly dipping concave bases and naturally opposed scoured bases within multi-erosive features (Figure 5.1A). The majority of the concave erosive features found in the base of multi-erosive channel bodies do not reflect a clear erosive relief relative to the channelized and scoured bases. These features are frequently exhibiting a shallower dip in the outcrop section, relative to the laterally adjacent channelized and scoured erosive features of the same channel body. When correcting the channelized bodies orientation according to the tilt of the area in which it was obtained, palaeocurrent direction of the concave bases can occasionally dip in the opposed direction relative to the direction of the laterally adjacent channelized bases. Scoured erosive features are however naturally dipping with a high angle in the opposed direction relative to the laterally adjacent concave and channelized bases of multi-erosive channel bases. (Figure 4.4). Such features are indicative of flute marks and

represent the majority of the opposed palaeocurrent measurements. It is important to emphasize that the scoured and occasionally concave bases display the right orientation, however, dipping opposed to the transport direction. To enable mean palaeocurrent direction calculation, the opposed palaeocurrent vectors of the concave and scoured bases were assigned to the opposite direction. This modification provides a more constrained general sediment dispersal pattern of the 80 channel bodies (Figure 5.1B), relative to the bulk data compilation (Figure 5.1A).

5.2.2 Geographical palaeocurrent distribution

Several faults and occasional folds are observed within the study area. The faults have a throw less than 10 m, which are frequently recorded within areas B, C and D (Figure 5.2B). The bulk dataset from area A, C, D and E display an average vector direction towards southeast (Figure 5.2A). Area B, however, comprise a bimodal palaeocurrent distribution oriented transverse to the general average palaeocurrent direction towards northeast and southwest. Oblique and transverse palaeocurrent scatter is observed within all the rose-diagrams of Figure 5.2A, with occasional clusters of directional vectors oriented in the opposite quadrant, relative to the predominating palaeocurrent directions (Figure 5.2A). As previously described, opposed palaeocurrent directions are commonly obtained from scoured features and occasionally shallowly dipping concave bases measured from multi-erosive channel bases. Average palaeocurrent directions thus provide a lower scatter by correcting the distorted and opposed data assemblage of the concave and scoured bases (Figure 5.2C). Nevertheless, area B still exhibits a bimodal distribution, which could be due to poor data quality affected by the small variations in tilt and dip direction within the area. An alternative interpretation suggests the channel orientation to represent the actual flow direction. This is coherent with the high variance of orientations in general, which reflect the nature of a highly sinuous and crevassing system (Ghosh, 2000; Hubbard *et al.*, 2008).

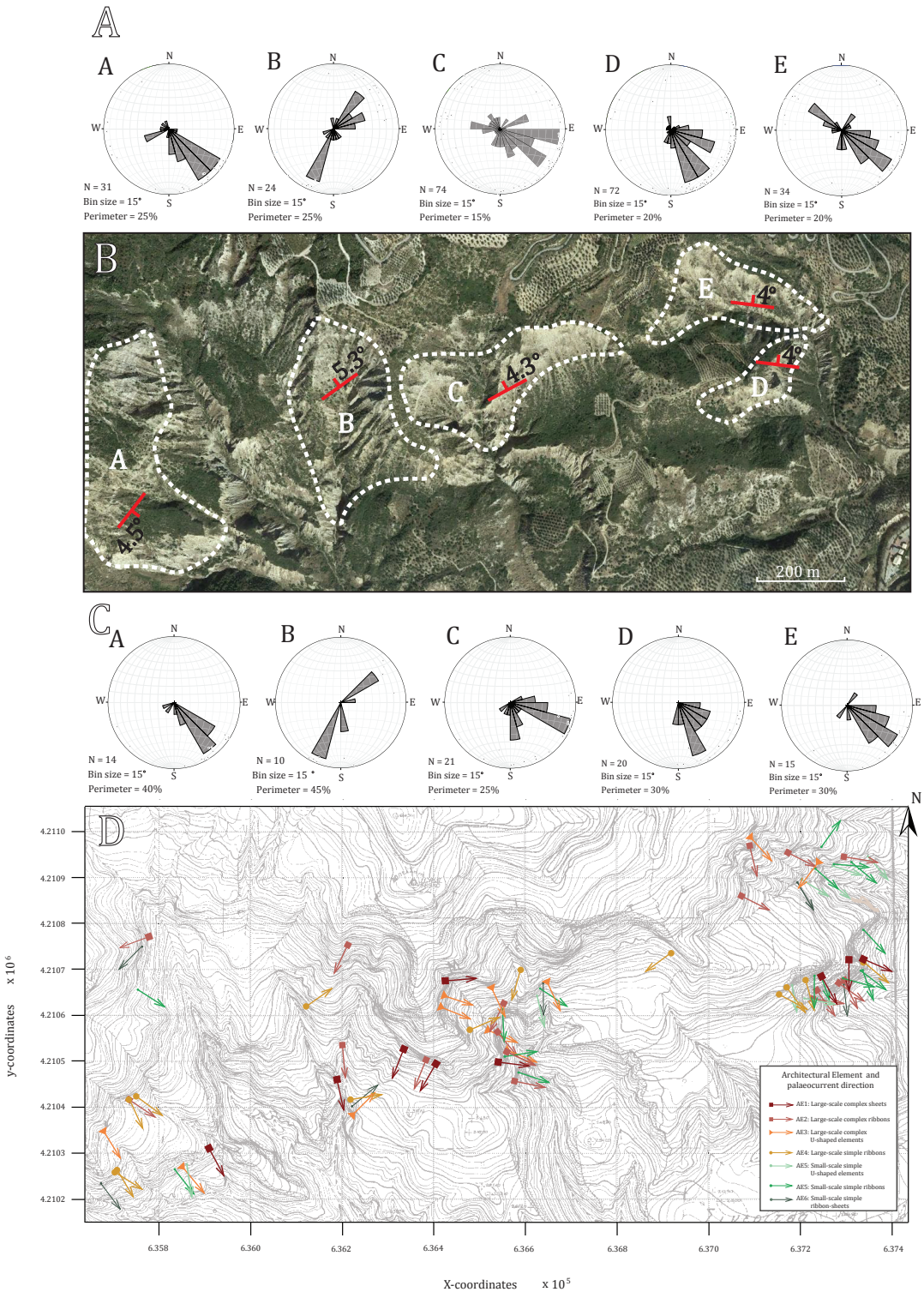

*Figure 5.2: **A)** Rose diagrams showing the palaeocurrent directions obtained in each area (Area A to E). **B)** Map of the study areas A, B, C, D and E, including average bedding dip and strike of each area. Modified from Google Earth. **C)** Average palaeocurrent direction of 80 individual channel bodies calculated from the bulk dataset presented in sub-figure **A). D)** Topographic map displaying average paleocurrent directions obtained for each channel body and discriminated according to Architectural Element (AE) type.*

5.2.3 Architectural Elements

Palaeocurrent indicators recorded from Architectural Element 1 to 7 display an average transport direction towards southeast (Figure 5.3A). However, individual architectural elements have oblique, transverse and opposed palaeocurrent vectors (Figure 5.3A). These vectors are similar to what is recorded from the individual datasets obtained from Area A to E. The oblique and transverse palaeocurrent directions evidence the relation to channel sinuosity and crevassing observed in the field. The opposed palaeocurrent directions mainly represent the scoured and occasionally concave erosive features of multi-erosive channel bodies. By assigning these measurements to their opposed direction, relative to their orientation the various architectural elements display a more constrained palaeocurrent distribution with a mean palaeocurrent direction towards southeast (Figure 5.3B). However, the non-meandering channels, crevasse channels and splays (Architectural Element 3, 5 and 7) reflect a polymodal distribution which may be due to the branching and crevassing nature of these channels, oriented transverse and oblique to the main palaeocurrent direction (*e.g.* Hubbard *et al.*, 2008). The high variation of vector directions obtained from the 80 channel bodies, combined with the internal sedimentary composition and structures observed in field, suggest a distributary deep-water system of moderate to high sinuosity, with frequent events of outer-bank breaching (Figure 5.4).

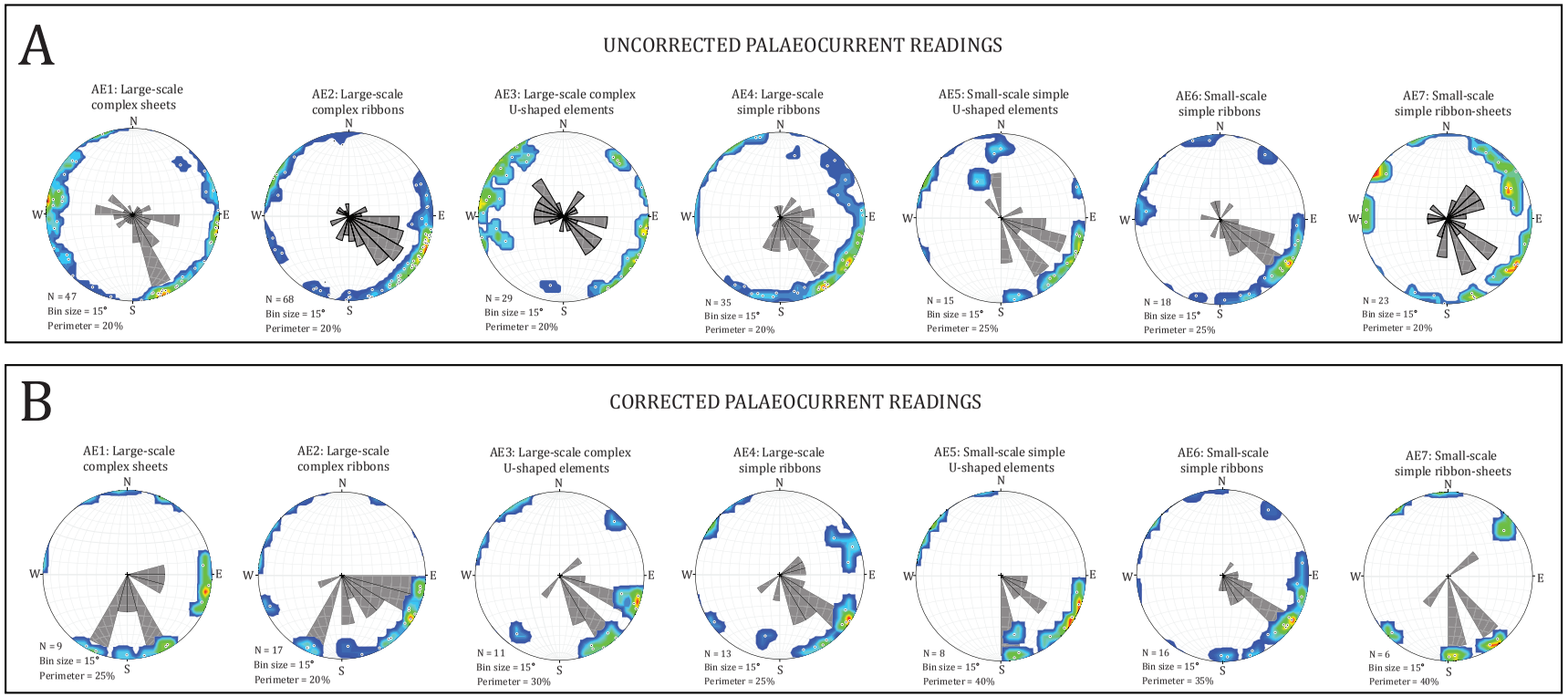

Figure 5.3: ***A)*** *Seven rose diagrams displaying palaeocurrent orientations obtained from 80 channel bodies. These measurements are grouped by type of architectural element individual measurements were obtained from. The opposed palaeocurent directions in figure* ***A*** *are concentrated in the northwest and southeast quadrant. These palaeocurrent measurements have been assigned to their opposed direction to enable average palaeocurrent direction calculation. The result is shown in figure* ***B****.* ***B)*** *The resultant rose diagrams displaying the average palaeocurrent direction of seven architectural elements.*

Figure 5.4: Block diagram of a distributive sinuous channel system. Arrows represent the direction of the flow within the distributary system. Stereoplot diagram shows palaeocurrent directions for each of the localities marked in the diagram (A to J). Note the high variation in transport directions within the same depositional system.

5.3 Channel body Width/Thickness dimensions

The individual cross-section aspect of the 80 channelized rock bodies is highly variable in width and thickness, exhibiting aspect ratios from 1.6 to 35. Sixty-three channel bodies are classified as *complete,* exposing both of their lateral bounding margins. However, fourteen channels are defined as *partially complete*, exposing one lateral channel margin, whereas three channels are defined as *incomplete,* exposing none of their lateral bounding margins. Partly complete and incomplete channels and channel complexes provide information on minimum channel width, however, these channels are not applicable for *W/T* ratio analysis. The width and thickness values are analysed in linear and log-log scatter plots to identify potential trends in the seven channelized Architectural Elements (Figures 5.5 to 5.7).

Large-scale complex U-shaped elements (Architectural Element 3), and Large-scale simple ribbons (Architectural Element 4) have a moderate *W/T* relation with a correlation coefficient (R^2) of 47% and 57%, whereas Small-scale simple U-shaped elements (Architectural Element 5) and Small-scale simple ribbons (Architectural Element 6) have a strong correlation coefficient 60% and 80% (Figure 5.6). However, the multi-storey channels (Architectural Element 1 and 2) and crevasse channel sheets (Architectural Element 7) reflect the highest scatter in both the linear and log-log plots, with correlation coefficients of 10% to 31% (Figure 5.6). Measurements obtained from channel complexes comprising laterally and vertically stacked channels are complex because they imply width/thickness ratios either higher or lower than that of the individual internal channels.

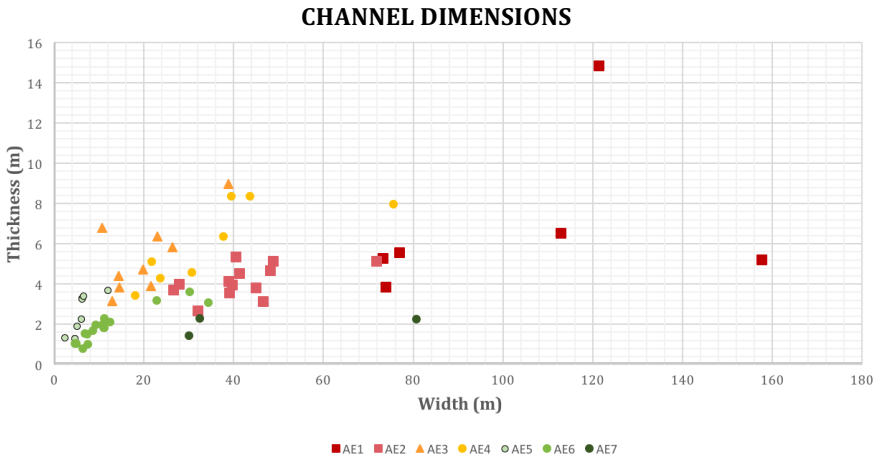

Figure 5.5: Linear scatterplot of the W/T relation of 63 complete channel bodies grouped into seven Architectural Elements (AE).

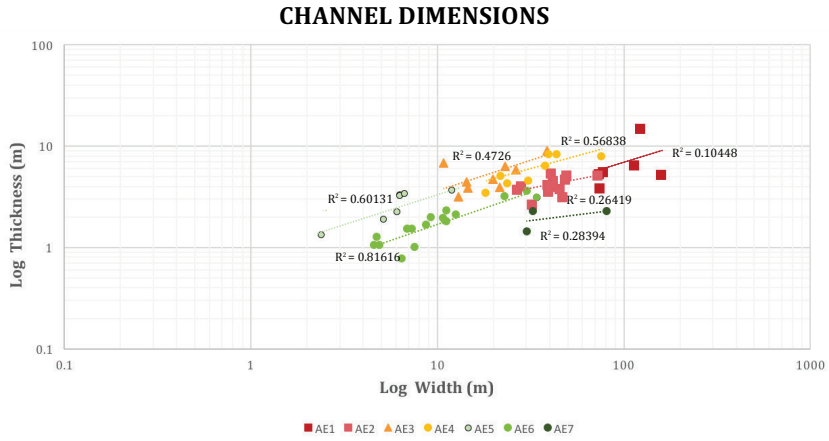

Figure 5.6: Log-log scatter plot of the W/T relation of 63 channel bodies, also presented in linear scatter plot (Figure 5.5.).

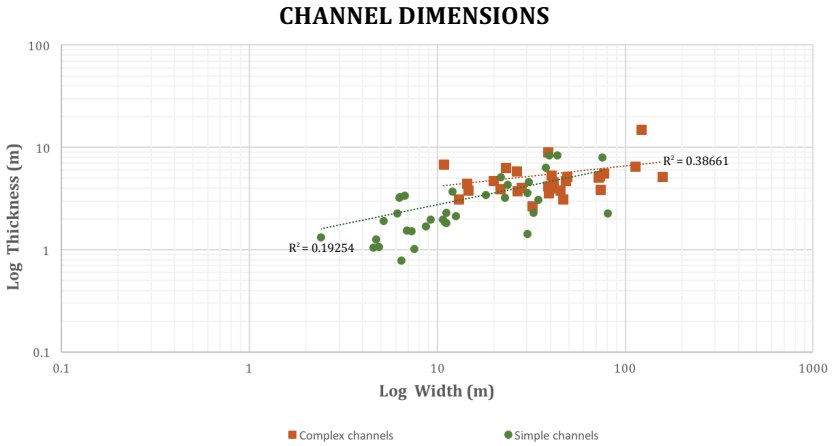

Figure 5.7: Log-log scatter plot of the W/T relation of 63 channel bodies, also presented in linear and log-log scatterplot (Figure 5.6 and 5.7), grouped into complex and simple channels.

The weak linear relation of the width and thickness values of Small-scale simple U-shaped elements(Architectural Element 5) Small-scale simple ribbons (Architectural Element 6) and Small-scale simple ribbon-sheets (Architectural Element 7; Figure 5.7), suggest the crevassing channel to rapidly change in width and thickness, during the transition from being confined to unconfined (Figure 5.8). This transition reflects substantial changes in the crevassing channels W/T ratio, whereby the erosive step gradually decreases with simultaneous rapid lateral expansion.

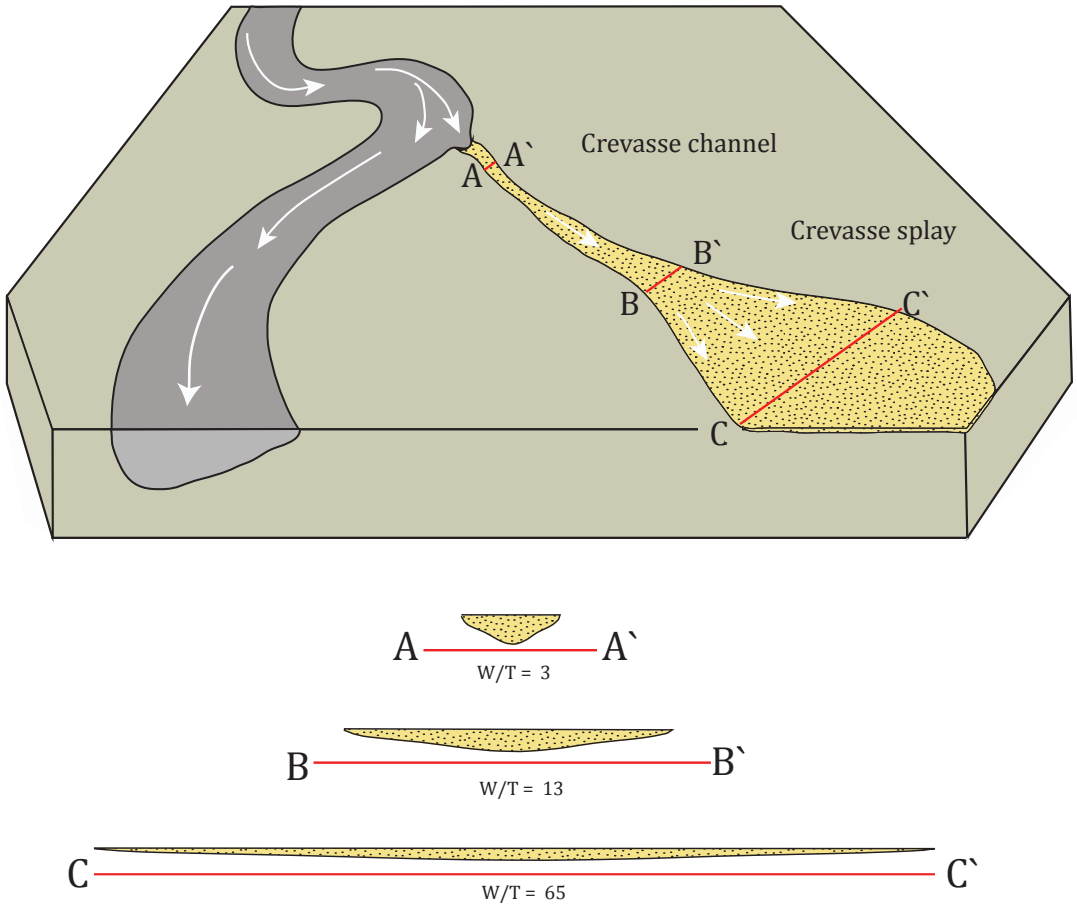

Figure 5.8: Schematic diagram illustrating the lateral change in crevasse channel/splay geometry during a brief spill-out or initial phase of longer spill-out event. The crevassing channel rapidly increases its W/T ratio from being fully confined to unconfined. Arrows represent the flow direction.

5.4 Spatial distribution and variation of channelized bodies

5.4.1 Vertical variation in channel body dimension and orientation

In order to identify any stratigraphic trends in terms of channel body dimensions, spatial distribution and orientation, minimum, maximum and average thickness, width, *W/T* ratio and palaeocurrent direction, values are evaluated against their topographic height of the study area. The linear and semi-log scatterplots reflect a non-linear data distribution, whereby no apparent trend is recognized (Figure 5.9A, C, E and G). However, by using the average value of every parameter per 20 m upwards within the stratigraphy, apparent trends are recognized (Figure 5.9B, D, F and H).

Apparent trends are displayed within all the data variables, which reflect multiple local decreasing and increasing-upwards trends for the minimum, maximum and/or average values for the different parameters (Figure 5.9B, D, F and H). It is thus important to emphasize the number of measurements representing the average values for individual bars. The majority of the bulk dataset has been obtained between 250 to 310 m.a.s.l., whereas the minority has been measured in the base and top of the Pellini Member. These measurements are defined to be less reliable based on the low number of measurements obtained in these regions. This is due to the lack of exposure and hence lack of data, and are not considered as representative for the average value at the given intervals. The following description will therefore not consider these sections, marked by red vertical lines in Figure 5.9B, D, F and H.

Channel thickness and palaeocurrent orientation (Figure 5.9B and H) display the clearest upward trends within the vertical length of the study area, in contrast to the channel width and *W/T* ratio which display a rather chaotic appearance. The average channel thickness reflects an overall upward increase, with local upwards decreasing trends in the average channel thickness (Figure 5.10B). An upwards increase in channel thickness could suggest a relative increased in the rate of overbank deposition, causing the channel to aggrade, combined with a decrease in channel avulsion (*e.g.* Weimer and Slatt, 2004).. Frequent upstream avulsion will prevent individual channel segments to evolve its planform geometry (*e.g.* Weimer and Slatt, 2004).

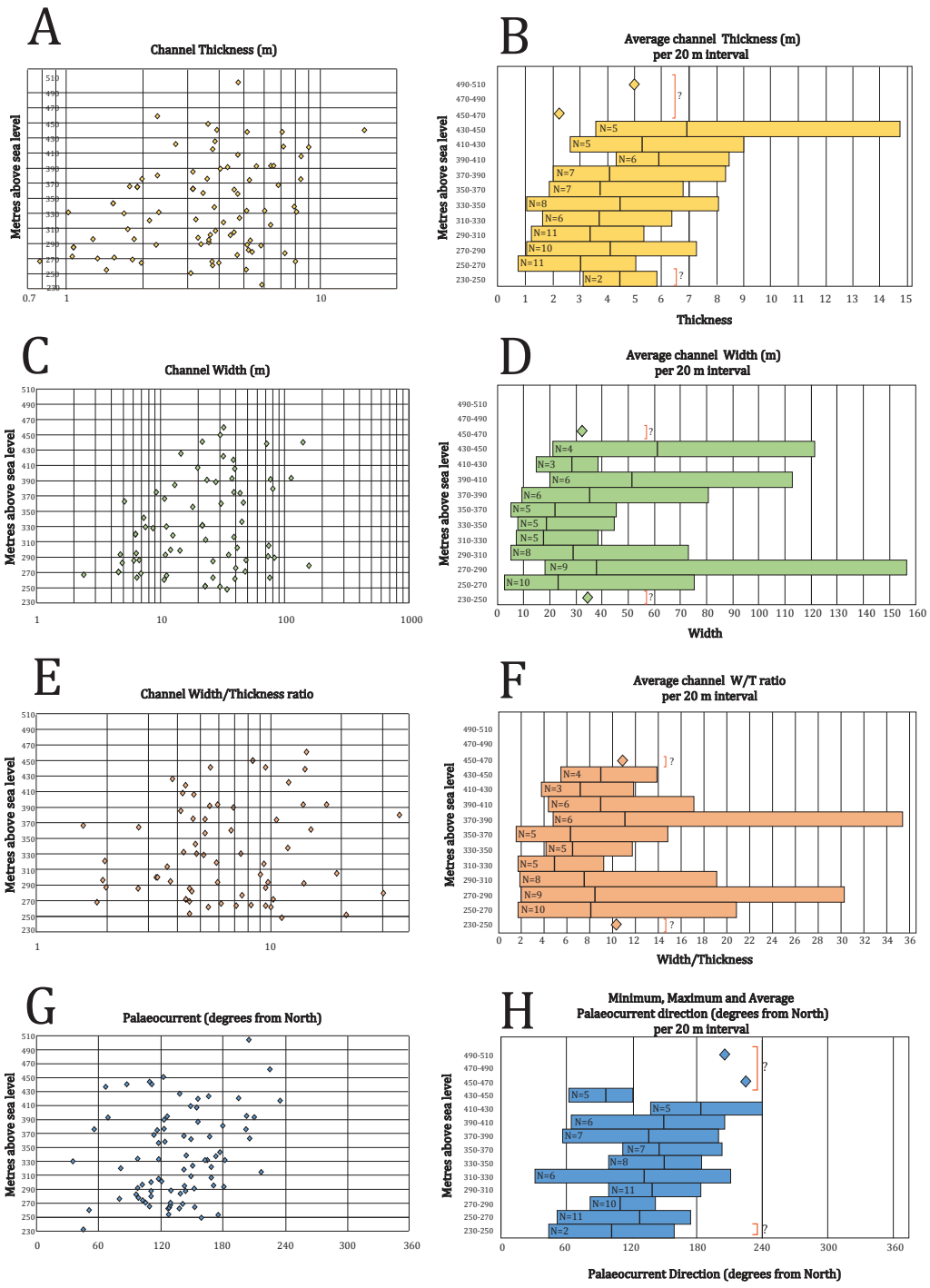

*Figure 5.9: Linear and log-log scatter plots displaying vertical distribution of channel thickness (**A**), channel width (**C**), W/T ratio (**E**) and palaeocurrent direction (**G**) against topographic height. Four bar charts, reflecting the minimum, maximum and average value of channel thickness (**B**), channel width (**D**), channel W/T ratio (**F**) and palaeocurrent direction (**H**) per 20 m upwards within the study area. Bar charts D and F comprise 63 measurements, whereas bar charts B and H comprise 80 measurements. Black vertical lines within every bar represent the average value. Question marks are placed in the bar charts where number of measurements is smaller than 3. Squares represent single isolated measurements.*

The average width and *W/T* values of 63 channel bodies display no clear vertical trend (Figures 5.9D and F). The minimum width and *W/T* ratio reflect an apparent upwards increase. In contrast, the maximum value displays an upward decreasing trend from 250 to 330 m.a.s.l, followed by an increase up to 410 m.a.s.l. The vertical signature of the width and *W/T* ratio reflect high variations in minimum and maximum dimensional values. These high dimensional variations are indicative for the nature of the channel system, whereby large- and small-scale channels are distributed on the same stratigraphic level (Figure 5.10). This results in bars displaying high contrast between the minimum to the maximum value.

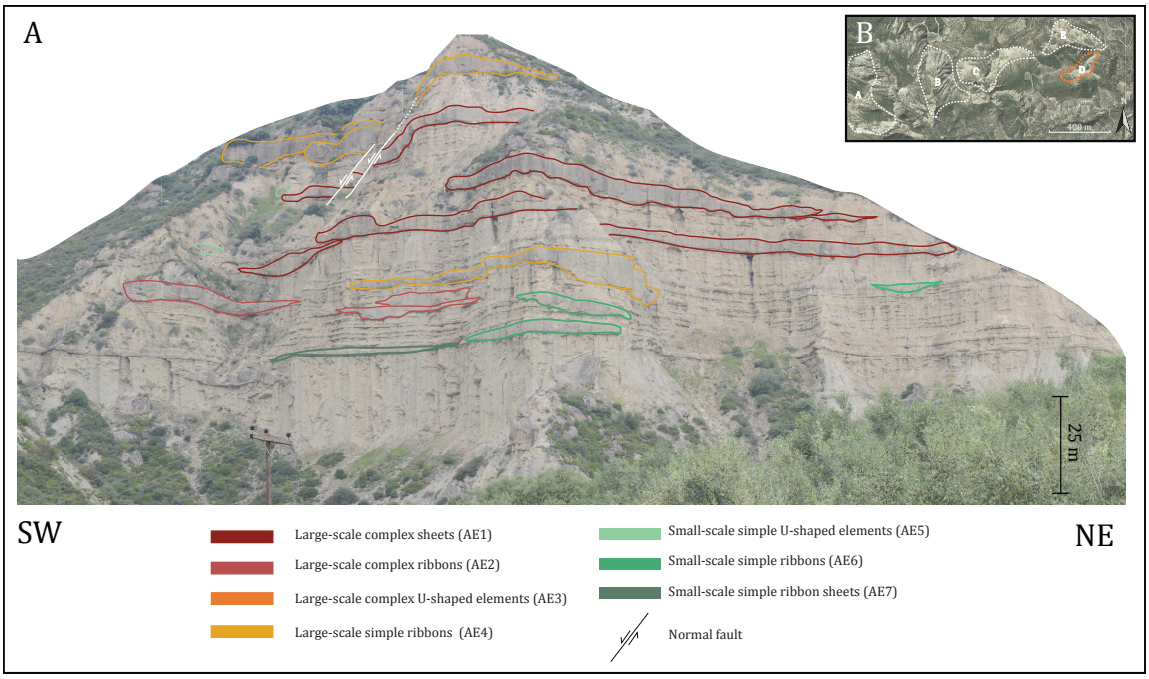

*Figure 5.10: **A**) Outcrop photograph of area D. Closely spaced multi- and single-storey, large- and small- scale channels and channel complexes. **B**) Overview map of the entire study area. Red dashed line mark area D.*

By compiling all the average palaeocurrent vectors within a vertical column (Figure 5.9H), an apparent trend is recorded in the minimum, maximum and average directional values. However, these data also show minor local, upward decreasing intervals. The average palaeocurrent distribution is generally between 100° to 175°. This vertical trend could suggest the system to be gradually migrating from east to south.

5.4.2 Meandering, non-meandering and crevassing channels

In order to analyse and identify potential vertical and lateral trends within the data population, three channel types are defined. The majority of the channelized Architectural Elements are interpreted as sinuous and meandering in origin (Architectural Element 1, 2 and 4), which constitutes 50% of the total sample population. In contrast, non-meandering channels (Architectural element 3) and crevasse channels (Architectural element 5, 6 and 7) comprise 14% and 36% of the bulk 80 channel bodies. Meandering, non-meandering and crevassing channels represent three channel types. These types display different flow properties and depositional mechanisms which will be outlined in the following section.

Meandering channels are characterized as sheet and ribbon-shaped single- and multi-storey 4th order elements. Channel deposits comprises lateral accretion packages oriented perpendicular to the flow direction, formed in matrix-supported conglomerates and sandstone. Meandering channels constitute the thickest and widest channelized elements within the Pellini Member, exhibiting a thickness mean of 5.4 m and a mean *W/T* ratio of 11.3. These large-scale channel bodies are distributed within the entire study area (Figure 5.11 and 5.12). The 331 to 361m and the 380 to 405 m intervals reflect an upward decrease and increase in channel thickness (Figure 5.13B) combined with a crude upward decrease and increase in channel *W/T* ratio (Figure 5.14B). Upwards increase in channel thickness suggests gradual aggradation of the channel system, which results in channel thickening (*e.g.* Posamentier and Kolla, 2003; Weimer and Slatt, 2004).

Non-meandering channels are characterized as multi-storey 4th order elements bounded by steeply dipping margins defining Large-scale complex U-shaped elements (Architectural element 3). These channels are separated from the meandering channels based on the lack of lateral accretion packages, and the low *W/T* ratio, with a mean value of 3.9. Non-meandering channels comprise vertically accreted and amalgamated bedsets of conglomerate and sandstone deposits, and are the least frequently recorded channelized body in the study area. An apparent higher occurrence is recorded within the middle part of the study area ranging from 405 to 445 m.a.s.l. (Figure 5.12). These channels are interpreted as short lived conduits relative to the sinuous and meandering channels due to the lack of lateral accretion packages.

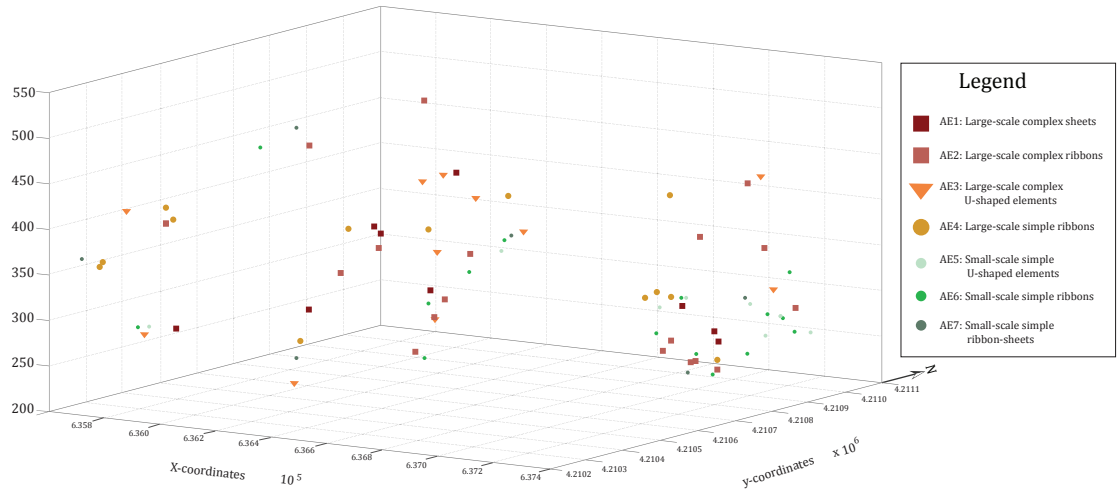

Figure 5.11: 3D scatterplot displaying the distribution of the 80 channel bodies measured in VRGS. Measurements were obtained from 233 to 505 m.a.s.l. AE = Architectural Element.

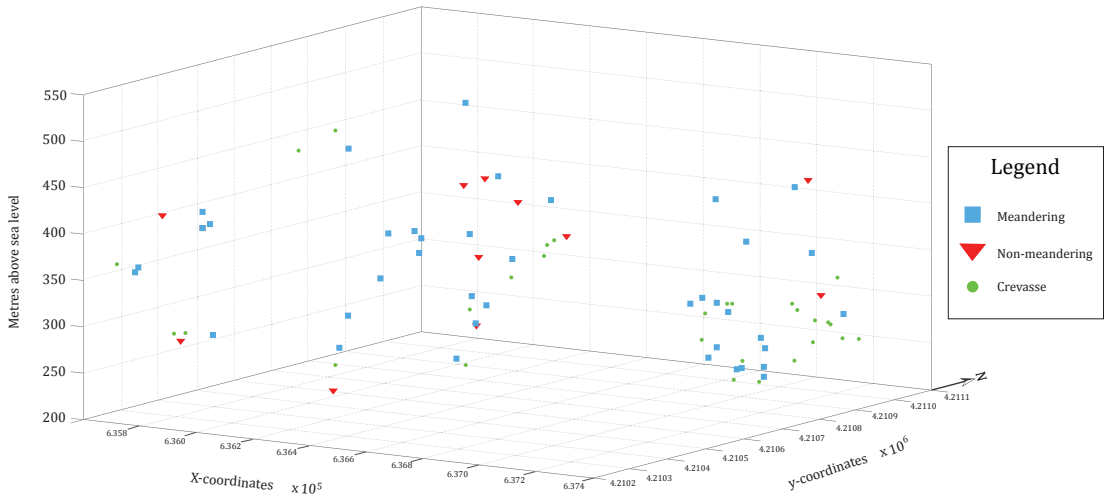

Figure 5.12: 3D scatterplot as seen in Figure 5.11, displaying the distribution of meandering, non-meandering and crevasse channels.

Crevasse channels comprises Small-scale simple U- shaped elements (Architectural Element 5), Small-scale simple ribbons (Architectural element 6) and Small-scale simple ribbon-sheets (Architectural Element 7). They are defined as 3rd order elements, filled by sand-prone deposits (Facies group D) with occasional pebble-lags. These elements are the thinnest and narrowest channel bodies within the study area, displaying a mean thickness value of 2.1 m and a *W/T* ratio of 7.4. They are distributed evenly between 230 to 385

m.a.s.l. (Figure 5.13B and 5.14B), though with a higher frequency towards east, east-northeast (Figure 5.12). Crevasse channels are spatially distributed close to large-scale complex and simple meandering and non-meandering channels. This suggest both the meandering and non-meandering channels to comprise a relatively high sinuous nature resulting in frequent crevassing of the outer channel bank, generated by high-energy currents.

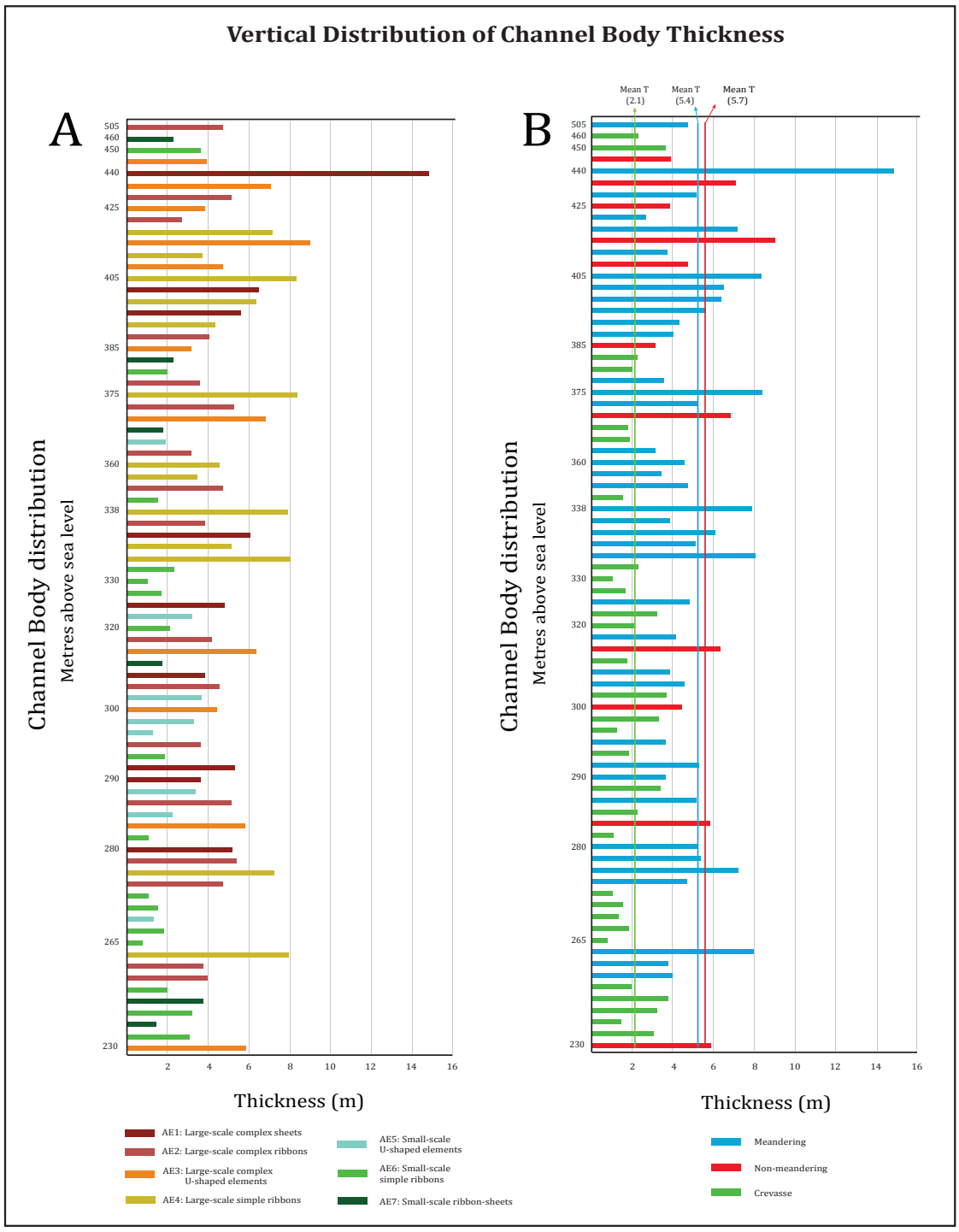

Figure 5.13: Bar diagrams displaying channel thickness variations and vertical distribution of 80 channels from 230 to 505 metres above sea level. ***A)*** *Vertical distribution of Architectural Element 1 to 7 (AE = Architectural Element)* ***B)*** *Similar bar diagram as displayed in* ***A,*** *though representing meandering (Architectural Element 1,2 and 4), non-meandering (Architectural Element 3) and crevasse channels (Architectural Element 5, 6 and 7).*

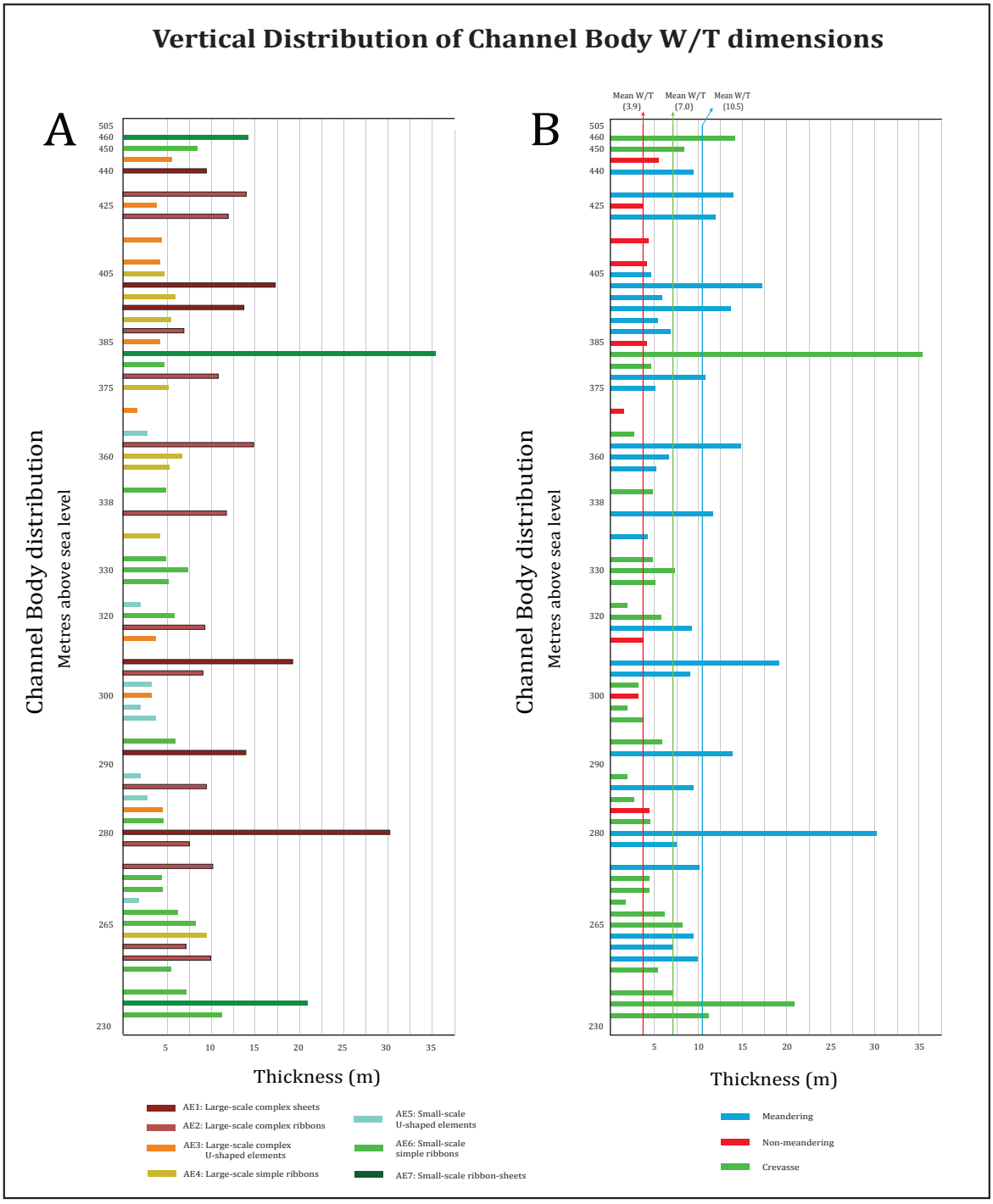

Figure 5.14: Bar diagrams displaying the vertical variation of the W/T ratio from 63 individual channels distribution from 230 to 505 metres above sea level. ***A)*** *Vertical distribution of Architectural Element 1 to 7.* ***B)*** *Similar bar diagram as displayed in* ***A****, though representing the vertical W/T variations of meandering (Architectural Element 1, 2 and 4), non-meandering (Architectural Element 3) and crevasse channels (Architectural Element 5, 6 and 7).*

6. DEPOSITIONAL MODEL AND PALAEOGEOGRAPHY

6.1 Applications for a deep-water distributary fan-channel system

The Pliocene to Pleistocene deep-water Aiges and Rethio-Dendro Formations are interpreted as turbiditic and hemipelagic in origin (Rohais *et al.*, 2007a; Leeder *et al.*, 2012). They are argued to have been sourced by large-scale Gilbert-type deltas, which prograded along an east to west trending lacustrine to brackish water basin (Rohais *et al.*, 2007a; Leeder *et al.*, 2012). Theses formations contain minor basal occurrences of tabular or lenticular beds, interpreted as cohesionless debris flow deposits (Rohais *et al.*, 2007a). In contrast to the Aiges and Rethio-Dendro Formations, the Pellini Member is dominated by coarse-grained sandstones and conglomerates. This study suggests the Pellini Member to represent a high-energy environment, relative to the Aiges and Rethio-Dendro Formations, whereby the sediment transport and deposition was largely controlled by high-density turbidity currents.

The Pellini Member comprises closely spaced large- and small-scale, single- and multi-storey channels of meandering, non-meandering and crevassing origin. Various channel typed are frequently distributed along the same stratigraphic levels, ranging in width from 2.4 to 156 m, in thickness from 0.8 to 15 m, and display a W/T ratio between 3 and 35. This suggests the depositional system to comprise multiple, simultaneously active channels (*e.g.* Figure 5.10), which combined with the high variety in channel dimensions suggest a highly avulsive channel system. The channelized elements within the Pellini Member have a mean transport direction towards the southeast (Figure 5.1B), whereby the oblique and transverse orientations are interpreted to reflect the sinuous and crevassing nature of the system (Figure 5.4; *e.g.* Hubbard *et al.*, 2008). Based on the various channel types, present on the same stratigraphic interval, displaying different palaeocurrent directions, suggests a sinuous channel system with a branched morphology.

The large variations in channel width and thickness dimensions (*e.g.* Figures 5.5 to 5.7), suggest the channels of the Pellini Member to be highly affected by channel avulsion. The channel avulsion-threshold conditions may have been caused by an increase in channel sinuosity, channel lengthening, aggradation of overbank, levee, and channel thalweg,

and/or a decrease in channel relief (Kolla, 2007). These instabilities and avulsion-threshold conditions are indicative of allocyclic and autocyclic control mechanisms. The majority of the large-scale channels are filled with graded, tractive generated conglomerates and sandstone deposits, which indicate multiple episodes of channel infill. In contrast, small-scale channels frequently display a homogenous channel infill that is interpreted to reflect relatively rapid deposition, without any normal grading (*e.g.* Lowe, 1982; Janocko *et al.*, 2011; Talling *et al.*, 2012).

The multi-storey channels within the Pellini Member display a planform development of laterally stacked internal channels (Figure 4.6), vertically stacked internal channels (Figures 4.8 and 4.9), and a combination of both laterally and vertically stacked internal channels (Figure 4.5). The laterally stacked channels within the Pellini Member are interpreted to reflect times of minor overbank deposition, and/or rapid channel migration based on the lack of an upwards aggrading channel thalweg. Their laterally extensive geometries reflect a relatively modest, lateral confinement, which suggests the confining materials were cohesive to a lesser degree, relative to the turbidity flows. Channel aggradation is dependent upon overbank deposition, whereby overbank aggradation affects the stacking pattern of the channels (*e.g.* Clark and Pickering, 1996; McHargue *et al.*, 2011). Vertically stacked channel bodies are also indicative for being laterally confined by cohesive material which causes the channels to aggrade. (McHargue *et al.*, 2011).

Single-storey channels comprise meandering and crevassing channels and splays. Simple meandering channels are unilateral and display similar width and thickness dimensions as for multi-storey channels. These single-storey channels reflect a relatively low degree of lateral confinement, generated during times of minor overbank deposition; hence the lack of an aggrading thalweg. Crevasse channels and splays are defined as aggradational. These channels display the highest variations in lateral planform development as the channels transforms from being fully confined to unconfined (Figure 6.1A). The crevasse channel dimensions are strongly dependant on the duration and hydrograph of the gravity flow and spill-out flows, and of the character of the overbank environment. On the basis of flow jet expansion hydraulics, it is theoretically expected that the crevasse splay is 7 times wider than its feeder crevasse channel, and increasingly wider (>7x) with a

longer duration of the spill-out flow (Allen, 1985). Long-lasting spill-out events and/or multiple spill-out series are interpreted to result in crevasse channel branching, distributed on top of the crevasse splay (Figure 6.1B; Posamentier and Kolla, 2003). This phenomenon could explain the closely spaced crevasse channels located on the same bedding surface in the study area.

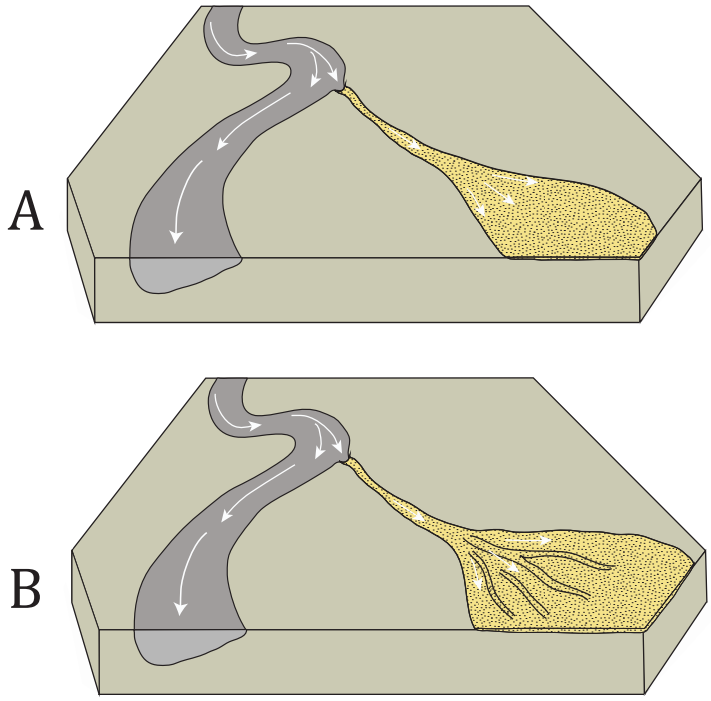

Figure 6.1: Schematic diagram of crevasse channel and initial flow-jet deposit (splay). ***A)*** *One single spill-out event.* ***B)*** *Long-lasting spill-out event or multiple spill-out series. Splay builds out and laterally expands with simultaneous crevasse channel extension and branching.*

The relative high occurrence of crevasse channels within the Pellini Member could indicate that the laterally adjacent large-scale channels have highly sinuous channel bends, whereby high-energy turbidity flows have scoured into the outer bends. These processes are thus equivalent to the mechanisms generating channel avulsion. Channel crevassing and subsequent avulsion is by several authors associated with leveed channels (*e.g.* Damuth *et al.*, 1983; Kenyon *et al.*, 1995; Pickering *et al.*, 1995; Posamentier and Kolla, 2003; Gervais *et al.*, 2004; O'Byrne *et al.*, 2007). However, such wedge shaped elements are not recorded within the Pellini Member. According to Posamentier and Kolla (2003) aggradational deep-water channels are associated with levee-overbank constructions, that are commonly one order of magnitude wider than their associated

channels. This suggests the hypothetical levee deposits within the Pellini Member to be laterally extensive, whereby any vertical thinning is hard to detect. The channels of the Pellini Member are dominated by coarse-grained sediment infill, in large part filled with matrix-supported conglomerates. Since the turbidity flow is density stratified, such coarse-grained channel infill is highly indicative of the turbidity flows vertical extent, whereby the majority of the flow is unconfined (Dykstra and Kneller, 2009; Janocko *et al.*, 2011). This suggests that large parts of the overbank regions are affected by the down-flowing, partly confined turbidity currents, which further indicates that extensive regions experienced subsequent aggradation during deposition. The lack of any levee indicators in the Pellini Member could also suggest the system to prevent high-relief levee accumulation by high-energy currents, scouring away topographic highs. Non-leveed channels enable the down-flowing turbidity currents to expand both, laterally and vertically, in contrast to subaerial channels and large-scale subaquous channels, which limits the turbidity flows lateral movements. Despite the lack of visually identified levee deposits within the Pellini Member, the channels are interpreted to experience frequent events of channel avulsion and/or bifurcation, which is supported by the high occurrence of crevasse channels and splays within the succession.

Aggradation, avulsion and bifurcation processes is interpreted as important factors controlling the planform development of the channels within the Pellini Member. Channel avulsion and bifurcation are considered natural processes occurring in the system. External factors such as eustatic changes, climatic variations or tectonic activity, however, can affect the nature of the channel-fan systems, whereby the channels planform development, avulsion and sediment aggradation becomes externally controlled.

Visual analysis of the three bar charts (Figure 5.9B, D and F) suggests that the width and *W/T* ratio do not display any clear vertical trends (Figure 5.9D and F). However, a progressive increase in channel thickness is recorded upwards within the succession (Figure 5.9B). The upwards increase in channel thickness is thus interpreted to reflect a gradual upwards increase in the rate of sedimentation leading to overbank and channel aggradation and/or an upwards decrease in the frequency of channel avulsion. It is debatable why an apparent upwards increase in channel thickness is not reflected in the channel width dimensions. It is thus important to emphasize that the contrast between

the thickest and thinnest channel in the Pellini Member (0.8 m to 15 m) is not as extensive as the variation in channel width (2.4 to 152 m). These large dimensional variations demonstrate the nature of an aggradational and highly avulsive channel system, within a deep-water environment.

The interchannel deposits within the Pellini Member comprise conglomerates, sandstones, mudstones and marlstones (*e.g.* Figures 4.19 and 4.2), and are volumetrically the most significant depositional elements within the Pellini Member. This supports the assumption that the turbidity-flows were largely unconfined. Thickening- and thinning-upwards sandstone sheets are interpreted to reflect gradual migration, avulsion, and/or bifurcation of the channel system, which re-routes the down-flowing turbidity-flows, and modify the local rate of sedimentation within the interchannel region (Gervais *et al.*, 2006; Prélat and Hodgson, 2013). This results in thicker sandstone deposits and increased sandstone amalgamation close to the spill-out conduits, and thinner sandstone deposits in the regions experiencing temporary depositional shut-down. The latter is then dominated by deposition from dilute, low-density turbidity currents, combined with hemipelagic and pelagic suspension settled mudstones and marlstones. Upwards increase or decrease in bed thickness of turbidite successions has traditionally been interpreted as lobes in a deep-water setting (Mutti and Normark, 1987), however, faults, folds, and variation in tectonic tilt, combined with vegetation and scree cover, complicates the recognition of large-scale lobe features within the study area.

The fine-grained mudstone and marlstone deposits are volumetrically the least recorded deposits within the deep-water Pellini Member. That could suggest the depositional environment to experience a high frequency of turbidity currents and/or high sedimentation rate, which preclude finer grained material from settling out of suspension. The frequency distribution of turbidity flows within the Pellini Member is unknown. It is, however, theoretically reasonable to assume that the deep-water system has also experienced smaller depositional events, which could be largely mud-prone. Thick successions of marlstone and mudstone could thus be a result of subaerial flooding events or flash floods reflecting seasonal changes.

The thickest mudstone and marlstone succession recorded within the Pellini Member is 5 m thick, which suggest deposition close to an abandoned channel and interchannel region. An alternative interpretation of the thick and laterally extensive mudstone and marlstone deposits to have been deposited within an interlobe zone (Figure 6.2A).

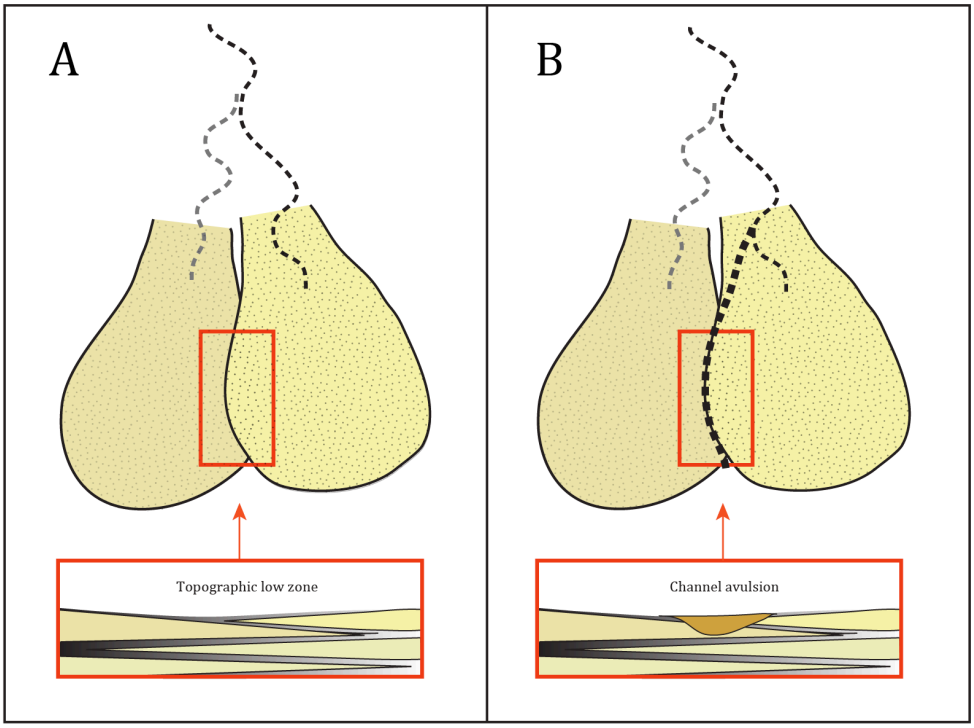

Figure 6.2: The interlobe zone. ***A)*** *Fine-grained deposition, accumulated between depositional lobes.* ***B)*** *Upstream channel avulsion with subsequent channel migration into the topographically lower interlobe zone. Dashed line represent deep-water channels.*

Field relationships, however, fail to support this theory due to the limitation within the study area including the variation in tectonic tilt, faults, folds vegetation and scree cover. This proposition is thus purely hypothetical in regards to the position of thick, fine-grained deposits within an interchannel region. An interlobe zone is generally characterized by fine-grained mudstone deposits, accumulated in a topographic low-zone (*sensu* Prèlat *et al.*, 2009). Compensational stacking of sandstone sheets is suggested to frequently occur within topographic low-zones, due to their ideal pathway for turbidity flows. Topographic low-zones are also an ideal pathway for channels which may cause the channels to migrate towards this region (Figure 6.2B; Prélat and Hodgson, 2013). As for fluvial channels, deep-water channels will continuously seek a longitudinal profile, graded to a base level, which in subaqueous settings is defined as the gravity base. This

phenomenon could thus be indicative of the recorded thick mudstone successions overlain by large-scale channel bodies (Figure 4. 8).

A slumped unit define the exposed basal region of the deep-water Pellini Member and reflect a major event of sediment emplacement into the deep-water basin. This thick succession could be evidential of tectonic activity, which is a reasonable assumption in relation to the Pliocene-Pleistocene extensional activity (Rohais *et al.*, 2007a; Leeder *et al.*, 2012; Ford *et al.*, 2013). However, the origin of this event is debatable due to the numerous possible trigger mechanisms which could have caused the emplacement. This slump may have affected the subsequent gravity flows to route along topographic depressions adjacent to the emplaced slump, until depressions were infilled and the local basin floor gradient was reduced (Cattaneo and Lucchi, 1995).

The Pellini Member is a syn-rift succession which suggests regional tectonics to be the most crucial mechanism affecting the deep-water depositional setting. Local faults with minor fault throws were recorded within the study area, indicating deformation after deposition. If the confined gravity flows were locally controlled, one would expect to record an increase in channel thickness close to deformation induced topography. However, no clear indication of fault controlled channels were recorded in the study area.

In regards to these observations and interpretations, combined with available literature on the Aiges Formation (Rohais *et al.*, 2007a) and Rethio-Dendro Formation (Leeder *et al.*, 2012), the Pellini Member is interpreted to represent a sinuous distributary fan-channel system within a deep-water environment (Figure 6.3).

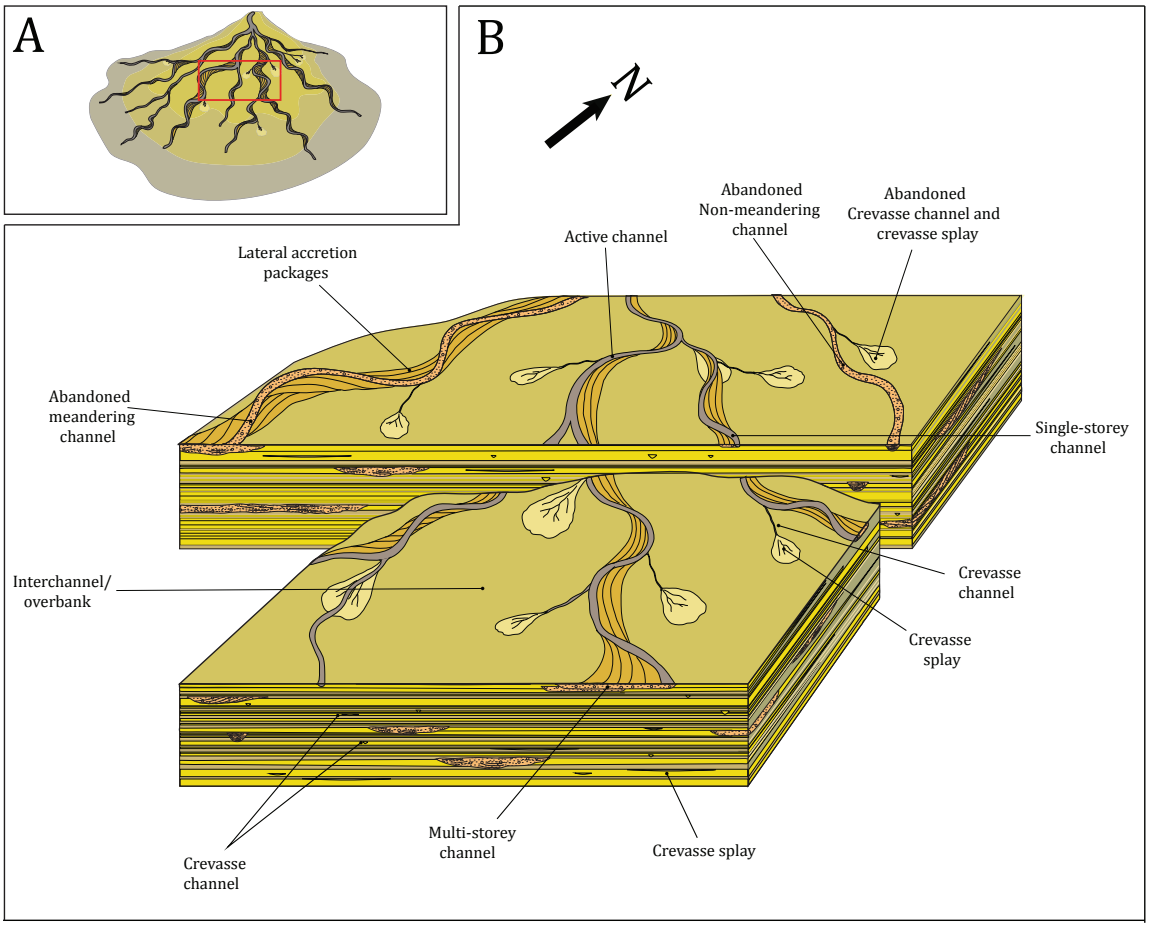

*Figure 6.3: Depositional model **A)** The relative position of the Pellini Members position in an idealized fan-channel system. **B)** Schematic block diagram of the various depositional elements within the Pellini Member.*

6.2 Palaeogeography and Environment

The palaeocurrent analysis reflects a predominant transport orientation from the west-northwest to the east- southeast, which suggests the source area to be localized opposed to the transport direction. Leeder *et al.*, 2012 argued the Rethio-Dendro Formation to be supplied by the large-scale Killini and/or Mavro fan deltas based on palaoecurrent measurements obtained by Rohais *et al.* (2007a) (Figure 6.4), combined with the lithological clast composition of the Rethio-Dendro Formation, and the formation`s geographical position. The Killini and Mavro fan deltas display radial palaeocurrent orientations also directed towards the Pellini Member (Figure 6.4). The channels of the Pellini Member reflect a mean transport direction towards the southeast (Figure 5.1B), which strongly suggest the feeder systems to be the Killini, and/or the Mavro fan deltas (Figure 6. 4). Other contributing factors supporting this assumption is the geographical position of the potential source areas relative to the Pellini Member, combined with the coarse-grained interior of the Pellini Member, pointing towards a coarse-grained source area.

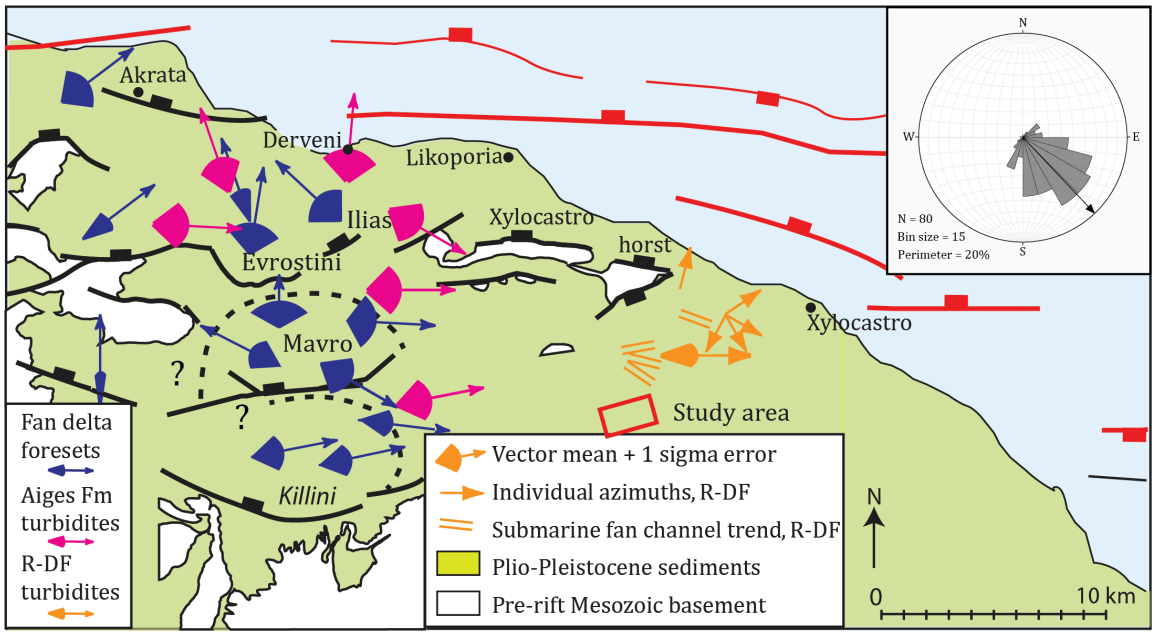

Figure 6.4: Palaeocurrent measurements obtained from the Killini, Mavro, Evrostini and Ilias Gilbert-type deltas. Dashed lines indicates the relative position of the Killini and Mavro fan deltas. Red square indicates the position of the study area. Stereonet in upper right corner displays palaeocurrent directions obtained from the Pellini Member. Modified from Leeder et al. (2012).

The Killini fan delta is older than the Mavro fan delta and comprises low quantities of Phyllite-Quartzite clasts, which are abundant in the Mavro fan delta (Rohais *et al.*, 2007a). According to Rohais *et al.* (2007a) this suggests that the Zarouchla complex to became exposed and extensively incisised by antecedent north-flowing rivers during the deposition of the Mavro fan delta, and during the time of subsequent abandonment of the Killini fan delta (Rohais *et al.*, 2007a). Phyllite-Quartzite clasts are not recorded within the study area which promoted the Killini fan delta as the most compatible feeder system to the Pellini Member.

An upwards relocation of the mean palaeocurrent direction is recorded within the vertical length of the study area (Figure 5.9H). This suggests the depositional system to gradually relocate from east to south. The Pellini Member is bounded to the north by the major northeast dipping Amphithea Fault. During deposition, this fault may have affected the transport direction by gradually influencing the channel system to migrate towards a topographic low-zone in the south.

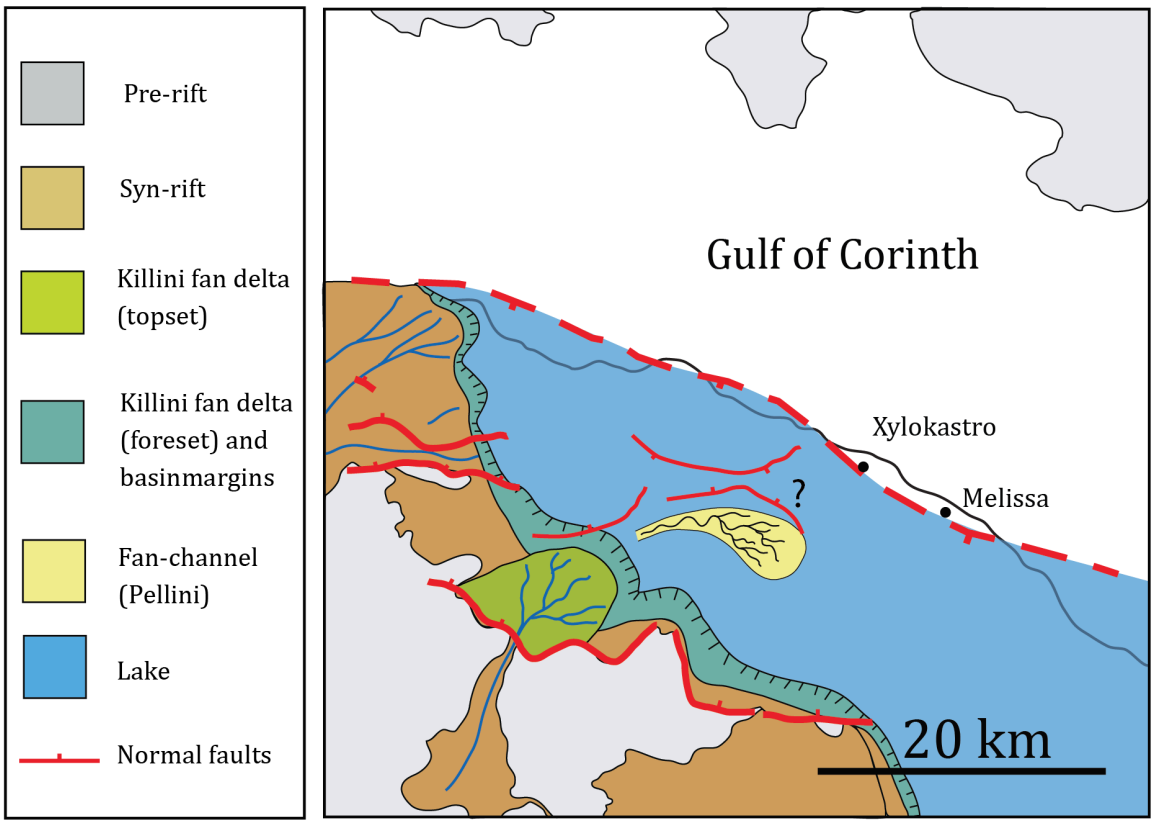

Figure 6.5: Proposed palaeogeographic source area of the Pellini Member. Modified Gawthorpe et al. (2016).

Leeder *et al.* (2012) argued that the deposition of the turbiditic/hemipelagic Rethio-Dendro Formation began during the "Great Deepening" event, which caused focused extension along the Killini and Mavro faults. The "Great Deepening" event was estimated to have occurred around 3.2 to 3.0 Ma by Leeder *et al.* (2012), based on the thickness and sedimentation rate of the Rethio-Dendro Formation, below the $^{40}Ar/^{39}Ar$ dated Xylocastro ash-layer. The thickness of the Rethio-Dendro Formation, 520 to 800m, was divided against comparable mean sedimentation rates of 1.2 mm/yr, These sedimentation rates were determined from three piston cores through the Late-Pleistocene turbiditic/hemipelagic lacustrine sediments in the modern central rift basin (Moretti *et al.*, 2004). This estimation, however, does not include the Pellini Member succession (Mike Leeder and Rob Gawthorpe, *pers. comm*.), which indicates that the "Great Deepening" event is much older than previously interpreted.

The Pellini Member is only exposed in a small area, and its lower and upper boundary is unrecorded. These limitations complicate any estimation of the member's vertical and lateral extent and also the member`s relation to under and overlying members and formations. Another factor is that the Pellini Member and the Rethio-Dendro Formation is separated by the northeast dipping Amphithea fault, which together with the Xylocastro high is argued to have laterally confined the Rethio-Dendro Formation during deposition. This could thus indicate that the Pellini Member might not be a part of the turbiditic/hemipalegic Rethio-Dendro fan system which is difficult to confirm due to the lack of correlating sedimentary successions between the Pellini Member and the Rethio-Dendro Formation. These successions, however, are separated according to their clast compositions, whereby the Rethio-Dendro Formation comprises Phyllite-Quartzite clasts, fine-grained turbidite and hemipelagic sediments, and the Pellini Member lacks Phyllite-Quartzite clasts, and is dominated by conglomerates and sandstone deposits. This lithological difference indicates different feeder systems within a deep-water setting.

Any age estimation in regards to the timing of the focused extension is complicated due to the lack of exposed stratigraphy between the Pellini Member and Rethio-Dendro Formation. Nevertheless, an estimation of the minimum can be performed by dividing the exposed vertical length of the study area, against a suitable rate for coarse-grained turbidite sedimentation.

The tectonic configuration during the deposition of the Pliocene Pellini Member is suggested to be the main allocyclic control mechanism of the palaeogeographic setting. Based on the predominating southeast directed palaeocurrent orientations, combined with available literature research of the Pliocene-Pleistocene extensional regimes and configuration (Ford *et al.*, 2007; Rohais *et al.*, 2007a; Leeder *et al.*, 2012; Ford *et al.*, 2013), the regional basin physiography is interpreted to be highly controlled by the extensional tectonic setting (Talling, 1998; Gawthorpe and Leeder, 2000). The Pellini Member is thus interpreted to have been deposited within a constrained elongated E-W trending rift basin, fed by axial and/or transverse feeder systems.

The extensional region affected the rate of accommodation space creation which exceeded the rate of sedimentation, due to the extensive rifting of the "Great Deepening" event. The Pellini Member deposits, however, do not display any upwards deepening trend, although frequent upwards thickening and thinning trends were recorded within successions of laterally extensive sandstone sheets and a general upwards increase in channel thickness. As such, the Pellini Member deposits reflect a more aggradational sedimentation, rather than retrogradational, indicate high rates of sedimentation causing overbank and channel aggradation and subsequent avulsion.

6.3 Modern Analogue

A similar, modern depositional system, fed by coarse-grained deltas, confined within a rift basin configuration is located in the present day Gulf of Corinth. The present day Gulf of Corinth has a maximum depth of 880 m. This bathymetric low is located in the eastern part of the basin. According to Leeder et al. (2012), the Pliocene-Pleistocene rift basin was 300 to 600 m deep, evidenced by Gilbert-type deltas prograding into the basin. The palaeocurrent measurements obtained from the Pellini Member channels are directed towards the southeast which could indicative the deepest part of the Pliocene-basin to be located within the eastern region. According to Rohais *et al.* (2007a) and Leeder *et al.* (2012) the Aiges and Rethio-Dendro Formation was deposited in brackish to freshwater conditions, whereas the present day Gulf of Corinth is marine. The Pellini Member is

interpreted to have been sourced by a Gilbert-type delta which are also considered some of the major feeder systems of the present day Gulf of Corinth. These coarse-grained deltas are to be found along the northern shores of the Peloponnese Peninsula, sourced by north-flowing rivers. An axial tributary channel is also considered an important feeder system located in the western region of the Gulf of Corinth (Figure 6.6).

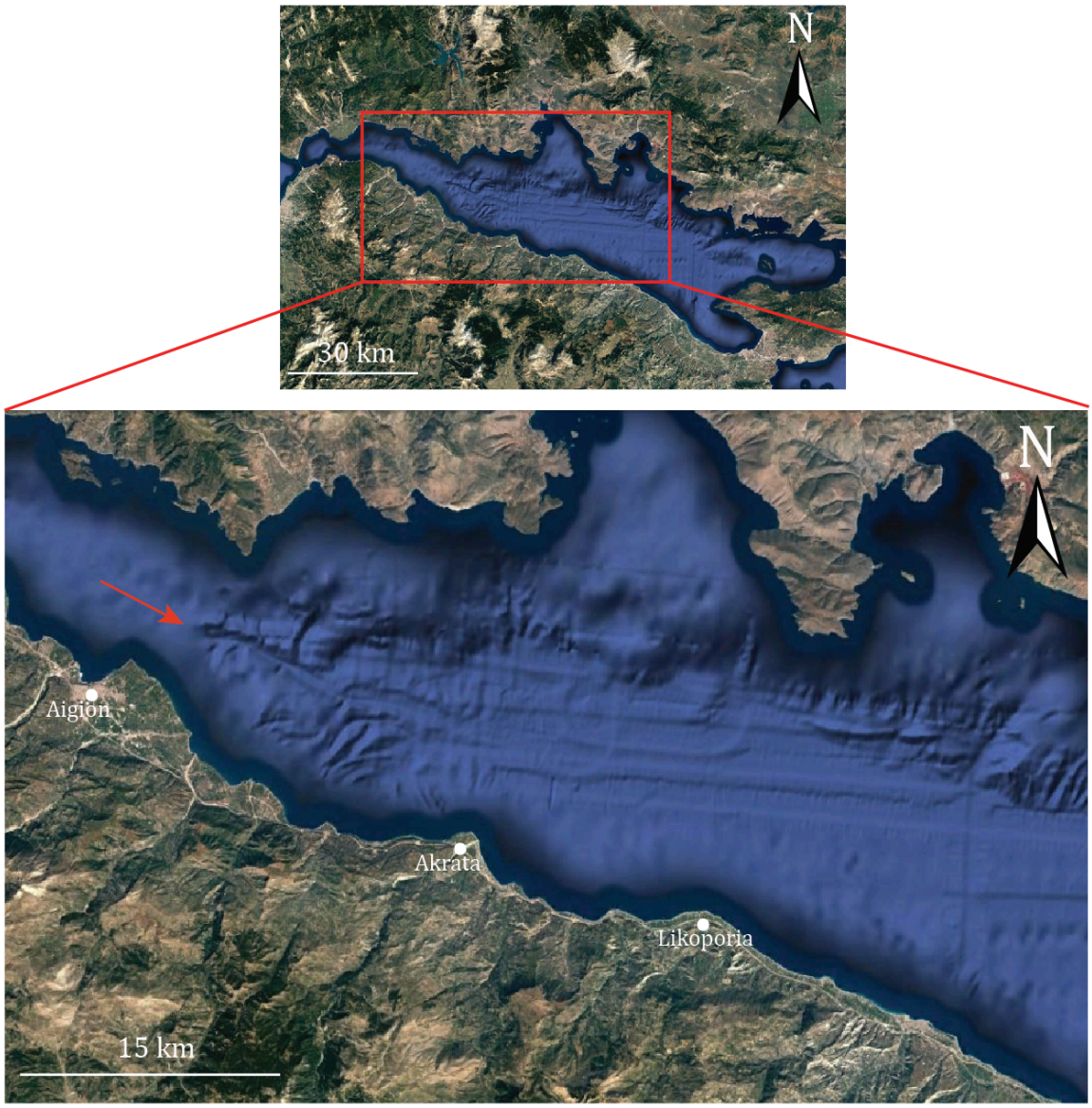

Figure 6.6: The present day Gulf of Corinth. Gilbert-type deltas building out along the northern shores of the Peloponnese Peninsula. Deep-water channel system oriented parallel to the northwest-southeast oriented basin configuration, transporting sediments from the bathymetric low in the west, to the bathymetric low in the east. Arrow indicates the flow direction of the deep-water channel system.

The primary mechanisms transporting sediments into the Gulf of Corinth are slumping, debris flows, and turbidity currents, trigged by earthquakes and slope instabilities along the steep flanks surrounding the gulf (McNeill *et al.*, 2005; Charalampakis *et al.*, 2007). The southern flanks of the gulf are heavily scoured into by sediment flows which have creates channels and canyons (McNeill *et al.*, 2005). The sediments succession of the Pellini Member is interpreted to have been transported and deposited by high- and low-energy turbidity flows. No large canyon features have been recorded within the Pellini Member.

The western part of the Gulf of Corinth has a lower subsidence compared to the eastern region, which has affected the deep-water channels to incise between the western bathymetric high and the bathymetric low central basin (Figure 6.6.). The basin comprises an axial channel, controlled by the south dipping subchannel fault. This submarine channel system comprise tributary channels in its middle and upper reaches, and sinuous channels that are subparallel to the axial channels lower reach (McNeill and Collier, 2004; Taylor *et al.*, 2011). The channels within the Pellini Member are interpreted to be gradually affected by the Amphithea Fault, which may have caused the channel system to relocate. Nevertheless, there has not been recorded any direct local control on the individual channels within the study area.

7. CONCLUSIONS

- Traditional sedimentological field techniques has enabled the distinction of 15 lithofacies within the Pellini Member, each representing different modes of deposition, which combined with digital outcrop analysis and literary research has allowed characterization of eleven architectural elements. These eleven architectural elements are distinguished according to their external and internal geometries, aspect ratios, bounding surfaces, and internal facies assemblages, representing different channelized and non-channelized elements within a deep-water system. Channelized elements Large-scale complex sheets (AE1), Large-scale complex ribbons (AE2), Large-scale complex U-shaped elements (AE3), Large-scale simple ribbons (AE4), Small-scale U-shaped elements (AE5), Small-scale simple ribbons, (AE6), and Small-scale simple ribbon-sheets and (AE7). Non-channelized elements are described as: Deformed large-scale complex sheets (AE8), Thin-to thick-bedded sandstone sheets (AE9) Sandy heterolithics (AE10), and Mudstone with thin-bedded sandstone sheets (AE11). These architectural elements represent meandering (AE1, 2 and 4), non-meandering (AE3) and crevasse-channels and splays (AE5, 6, and 7), alternating with interchannel deposits (AE8, 9, 10, and 11).

- Large- and small-scale channels are recorded on the same stratigraphic level, reflecting various transport directions which record the sinuous and crevassing nature of the channel system. On the basis of the recognized architectural elements, their spatial distribution, and high dimensional variety of the channelized elements, the Pellini Member is interpreted to reveal a depositional history as a sinuous distributary fan-channel system.

- Multi-storey channels are distinguished as meandering and non-meandering channels, displaying a sheet, ribbon or U-shaped geometry. These channel complexes are internally composed of vertically and/or laterally stacked internal channel bodies. The laterally stacked channels reflect times of minor overbank deposition, and/or rapid channel migration due to the lack of an upwards aggrading channel thalweg. Vertically stacked channel bodies reflect lateral confinement and/or rapid overbank aggradation

causing the channel to aggrade. Single-storey channels are distinguished as meandering and crevassing channels and splays displaying a ribbon, ribbon-sheet or U-shaped geometry. The single-storey meandering channels reflect a relatively low degree of lateral confinement, generated during times of minor overbank deposition; based on lack of an aggrading thalweg.

- Crevasse channels and splays reflect the highest variations in planform geometry, rapidly changing in thickness and width in the transition from being confined to unconfined. These channel bodies are often occurring on the same bedding surface closely spaced which suggest them to reveal a branched crevassing system generated by Long-lasting spill-out event or multiple spill-out series.

- Large-scale channels are filled with conglomerates and sandstone which indicate the density stratified coarse-grained turbidity flows to be laterally more extensive than the channel depth, leading to constant overspilling and overbank aggradation. Thickening- and thinning-upwards sandstone sheets suggest its development to be caused by gradual and/or abrupt migration, avulsion and/or bifurcation of channel segments. As a response to the re-routed down-flowing turbidity flows, the local rate of sedimentation is modified, causing local increase and decrease in the rate of overbank aggradation.

- The palaeoenvironmental setting of the Pellini Member reflects overall relatively high rates of sediment aggradation, combined with high rates of channel avulsion, which are the main processes controlling the channels' planform development and the creation of thickening and thinning upwards sandstone sheets. High rates of aggradation is caused by relatively high-frequency of coarse-grained turbidity flows, which are the main transport mechanism of sediments to the deep-water fan-channel system. Despite the significant degree of overbank sedimentation, no levees were recognized within the study area.

- The Pellini channels record an average southeast transport direction, which combined with the relatively coarse-grained interior suggest the Pellini Member to have been sourced from the west by the Killini fan delta. This is also indicated by the Pellini Members clast composition which is similar to what is recorded within the Gilbert-type

delta. The stratigraphic upward relocation of the palaeocurrent transport direction suggests the northeast dipping Amphiathea fault to have been active causing the overall transport direction to change from east to south. The Pliocene-Pleistocene rift configuration suggest tectonic activity to be the main control mechanism during the deposition of the Pellini Member.

REFERENCES

Abreu, V., Sullivan, M., Pirmez, C., and Mohrig, D., 2003, Lateral accretion packages (LAPs): an important reservoir element in deep water sinuous channels: Marine and Petroleum Geology, v. 20, no. 6, p. 631-648.

Allen, J., 1985, Principles of Physical Sedimentology. Allen & Unwin, London, 288 pp.

Allmendinger, R. W., Cardozo, N. C., and Fisher, D. M., 2012, Structural geology algorithms: Vectors and tensors: Cambridge, England, Cambridge University Press, p. 289

Amy, L., McCaffrey, W., and Kneller, B., 2004, The influence of a lateral basin-slope on the depositional patterns of natural and experimental turbidity currents: Geological Society, London, Special Publications, v. 221, no. 1, p. 311-330.

Armijo, R., Meyer, B., Hubert, A., and Barka, A., 1999, Westward propagation of the North Anatolian fault into the northern Aegean: Timing and kinematics: Geology, v. 27, no. 3, p. 267-270.

Armijo, R., Meyer, B., King, G., Rigo, A., and Papanastassiou, D., 1996, Quaternary evolution of the Corinth Rift and its implications for the Late Cenozoic evolution of the Aegean: Geophysical Journal International, v. 126, no. 1, p. 11-53.

Arnott, R., 2010, Deep-marine sediments and sedimentary systems: Facies models, v. 4, p. 295-322.

Backert, N., Ford, M., and Malartre, F., 2010, Architecture and sedimentology of the Kerinitis Gilbert-type fan delta, Corinth Rift, Greece: Sedimentology, v. 57, no. 2, p. 543-586.

Bell, R. E., McNeill, L. C., Bull, J. M., and Henstock, T. J., 2008, Evolution of the offshore western Gulf of Corinth: Geological Society of America Bulletin, v. 120, no. 1-2, p. 156-178.

Bell, R. E., McNeill, L. C., Bull, J. M., Henstock, T. J., Collier, R. E. L., and Leeder, M. R., 2009, Fault architecture, basin structure and evolution of the Gulf of Corinth Rift, central Greece: Basin Research, v. 21, no. 6, p. 824-855.

Bellian, J. A., Kerans, C., and Jennette, D. C., 2005, Digital outcrop models: applications of terrestrial scanning lidar technology in stratigraphic modeling: Journal of sedimentary research, v. 75, no. 2, p. 166-176.

Bernard, P., Lyon-Caen, H., Briole, P., Deschamps, A., Boudin, F., Makropoulos, K., Papadimitriou, P., Lemeille, F., Patau, G., and Billiris, H., 2006, Seismicity, deformation and seismic hazard in the western rift of Corinth: New insights from the Corinth Rift Laboratory (CRL): Tectonophysics, v. 426, no. 1, p. 7-30.

Billiris, H., Paradissis, D., Veis, G., England, P., Featherstone, W., Parsons, B., Cross, P., Rands, P., Rayson, M., and Sellers, P., 1991, Geodetic determination of tectonic deformation in central Greece from 1900 to 1988: Nature, v. 350, no. 6314, p. 124-129.

Boggs, S., 2011, Principles of sedimentology and stratigraphy, v. 551.3. 051 BOG.

Bouma, A. H., 1962, Sedimentology of Some Flysch Deposits: A Graphic Approach to Facies Interpretation, Elsevier Amsterdam, 168 p.:

Bouma, A. H., 2004, Key controls on the characteristics of turbidite systems: Geological Society, London, Special Publications, v. 222, no. 1, p. 9-22.

Briole, P., Rigo, A., Lyon-Caen, H., Ruegg, J., Papazissi, K., Mitsakaki, C., Balodimou, A., Veis, G., Hatzfeld, D., and Deschamps, A., 2000, Active deformation of the Corinth rift, Greece: results from repeated Global Positioning System surveys between

1990 and 1995: Journal of Geophysical Research: Solid Earth (1978–2012), v. 105, no. B11, p. 25605-25625.

Buckley, S. J., Howell, J., Enge, H., and Kurz, T., 2008, Terrestrial laser scanning in geology: data acquisition, processing and accuracy considerations: Journal of the Geological Society, v. 165, no. 3, p. 625-638.

Baas, J. H., 2000, EZ-ROSE: a computer program for equal-area circular histograms and statistical analysis of two-dimensional vectorial data: Computers & Geosciences, v. 26, no. 2, p. 153-166.

Cardozo, N., and Allmendinger, R. W., 2013, Spherical projections with OSXStereonet: Computers & Geosciences, v. 51, p. 193-205.

Cattaneo, A., and Lucchi, F. R., 1995, Long-distance correlation of sandy turbidites: a 2.5 km long cross-section of Marnoso-Arenacea, Santerno Valley, Northern Apennines, Atlas of Deep Water Environments, Springer, p. 303-306.

Charalampakis, M., Stefatos, A., Hasiotis, T., and Ferentinos, G., 2007, Submarine mass movements on an active fault system in the central Gulf of Corinth, Submarine Mass Movements and Their Consequences, Springer, p. 67-75.

Clark, J. D., and Pickering, K. T., 1996, Architectural elements and growth patterns of submarine channels: application to hydrocarbon exploration: AAPG bulletin, v. 80, no. 2, p. 194-220.

Colella, A., De Boer, P., and Nio, S., 1987, Sedimentology of a marine intermontane Pleistocene Gilbert-type fan-delta complex in the Crati Basin, Calabria, southern Italy: Sedimentology, v. 34, no. 4, p. 721-736.

Collier, R. L., and Dart, C., 1991, Neogene to Quaternary rifting, sedimentation and uplift in the Corinth Basin, Greece: Journal of the Geological Society, v. 148, no. 6, p. 1049-1065.

Cowie, P., Gupta, S., and Dawers, N., 2000, Implications of fault array evolution for synrift depocentre development: insights from a numerical fault growth model: Basin Research, v. 12, no. 3-4, p. 241-261.

Damuth, J. E., Flood, R., Pirmez, C., and Manley, P., 1995, Architectural elements and depositional processes of Amazon Deep-sea Fan imaged by long-range sidescan sonar (GLORIA), bathymetric swath-mapping (Sea Beam), high-resolution seismic and piston-core data, Atlas of Deep Water Environments, Springer, p. 105-121.

Damuth, J. E., Kolla, V., Flood, R. D., Kowsmann, R. O., Monteiro, M. C., Gorini, M. A., Palma, J. J., and Belderson, R. H., 1983, Distributary channel meandering and bifurcation patterns on the Amazon deep-sea fan as revealed by long-range side-scan sonar (GLORIA): Geology, v. 11, no. 2, p. 94-98.

Dart, C. J., Collier, R. E. L., Gawthorpe, R. L., Keller, J. V., and Nichols, G., 1994, Sequence stratigraphy of (?) Pliocene-Quaternary synrift, Gilbert-type fan deltas, northern Peloponnesos, Greece: Marine and petroleum geology, v. 11, no. 5, p. 545-560.

Davies, R., England, P., Parsons, B., Billiris, H., Paradissis, D., and Veis, G., 1997, Geodetic strain of Greece in the interval 1892–1992: Journal of Geophysical Research: Solid Earth (1978–2012), v. 102, no. B11, p. 24571-24588.

Degnan, P., and Robertson, A., 1998, Mesozoic-early Tertiary passive margin evolution of the Pindos ocean (NW Peloponnese, Greece): Sedimentary Geology, v. 117, no. 1, p. 33-70.

Dewey, J. F., and Şengôr, A. M. C., 1979, Aegean and surrounding regions: complex multiplate and continuum tectonics in a convergent zone: Geological Society of America Bulletin, v. 90, no. 1, p. 84-92.

REFERENCES

Di Celma, C., 2011, Sedimentology, architecture, and depositional evolution of a coarse-grained submarine canyon fill from the Gelasian (early Pleistocene) of the Peri-Adriatic basin, Offida, central Italy: Sedimentary Geology, v. 238, no. 3, p. 233-253.

Di Celma, C., Cantalamessa, G., Didaskalou, P., and Lori, P., 2010, Sedimentology, architecture, and sequence stratigraphy of coarse-grained, submarine canyon fills from the Pleistocene (Gelasian-Calabrian) of the Peri-Adriatic basin, central Italy: Marine and Petroleum Geology, v. 27, no. 7, p. 1340-1365.

Doutsos, T., Kontopoulos, N., and Poulimenos, G., 1988, The Corinth-Patras rift as the initial stage of continental fragmentation behind an active island arc (Greece): Basin Research, v. 1, no. 3, p. 177-190.

Doutsos, T., and Piper, D. J., 1990, Listric faulting, sedimentation, and morphological evolution of the Quaternary eastern Corinth rift, Greece: first stages of continental rifting: Geological Society of America Bulletin, v. 102, no. 6, p. 812-829.

Duffy, O. B., Brocklehurst, S. H., Gawthorpe, R. L., Leeder, M. R., and Finch, E., 2015, Controls on landscape and drainage evolution in regions of distributed normal faulting: Perachora Peninsula, Corinth Rift, Central Greece. Basin Research v. 27, no 4, p 473-494.

Dykstra, M., and Kneller, B., 2009, Lateral accretion in a deep-marine channel complex: implications for channellized flow processes in turbidity currents: Sedimentology, v. 56, no. 5, p. 1411-1432.

Fabuel-Perez, I., Hodgetts, D., and Redfern, J., 2009, A new approach for outcrop characterization and geostatistical analysis of a low-sinuosity fluvial-dominated succession using digital outcrop models: Upper Triassic Oukaimeden Sandstone Formation, central High Atlas, Morocco: AAPG bulletin, v. 93, no. 6, p. 795-827.

Flotté, N., Sorel, D., Müller, C., and Tensi, J., 2005, Along strike changes in the structural evolution over a brittle detachment fault: Example of the Pleistocene Corinth–Patras rift (Greece): Tectonophysics, v. 403, no. 1, p. 77-94.

Ford, M., Rohais, S., Williams, E. A., Bourlange, S., Jousselin, D., Backert, N., and Malartre, F., 2013, Tectono-sedimentary evolution of the western Corinth rift (Central Greece): Basin Research, v. 25, no. 1, p. 3-25.

Ford, M., Williams, E. A., Malartre, F., and Popescu, S. M., 2007, Stratigraphic Architecture, Sedimentology and Structure of the Vouraikos Gilbert-Type Fan Delta, Gulf of Corinth, Greece: Sedimentary Processes, Environments and Basins: A Tribute to Peter Friend (Special Publication 38 of the IAS), v. 22, p. 49.

Friend, P., Slater, M., and Williams, R., 1979, Vertical and lateral building of river sandstone bodies, Ebro Basin, Spain: Journal of the Geological Society, v. 136, no. 1, p. 39-46.

Gawthorpe, R., and Colella, A., 1990, Tectonic Controls on Coarse-Grained Delta Depositional Systems in Rift Basins: Systems in Rift Basins. Coarse-Grained Deltas: Special Publication 10 of the IAS, v. 27, p. 113-127.

Gawthorpe, R., and Leeder, M., 2000, Tectono-sedimentary evolution of active extensional basins: Basin Research, v. 12, no. 3-4, p. 195-218.

Gawthorpe, R., Leeder, M., Muravchik, M., Kranis, H., Skourtsos, E., Andrews, J., and Henstra, G. A., Deepwater Syn-Rift Sedimentation: Tectonic Geomorphology and Sedimentology From the Modern and Plio-Pleistocene of the Corinth Rift, Greece. Paper presented at the annual convention and exhibition of the AAPG, Calgary, Canada.2016.

Gawthorpe, R. L., Fraser, A. J., and Collier, R. E. L., 1994, Sequence stratigraphy in active extensional basins: implications for the interpretation of ancient basin-fills: Marine and Petroleum Geology, v. 11, no. 6, p. 642-658.

Gervais, A., Savoye, B., Mulder, T., and Gonthier, E., 2006, Sandy modern turbidite lobes: a new insight from high resolution seismic data: Marine and Petroleum Geology, v. 23, no. 4, p. 485-502.

Gervais, A., Savoye, B., Piper, D. J., Mulder, T., Cremer, M., and Pichevin, L., 2004, Present morphology and depositional architecture of a sandy confined submarine system: the Golo turbidite system (eastern margin of Corsica): Geological Society, London, Special Publications, v. 222, no. 1, p. 59-89.

Ghisetti, F., and Vezzani, L., 2005, Inherited structural controls on normal fault architecture in the Gulf of Corinth (Greece): Tectonics, v. 24, no. 4.

Ghosh, B., and Lowe, D. R., 1993, The architecture of deepwater channel complexes, Cretaceous Venado Sandstone Member, Sacramento Valley, California. In: Graham, S.A., Lowe, D.R.. (Eds.), Advances in the sedimentary Geology of the Great Valley Group, Sacramento Valley, California, p. 51-65. SEPM, Pacific Section, Guidebook 73.

Ghosh, P., 2000, Estimation of channel sinuosity from paleocurrent data: a method using fractal geometry: Journal of Sedimentary Research, v. 70, no. 3.

Gibling, M. R., 2006, Width and thickness of fluvial channel bodies and valley fills in the geological record: a literature compilation and classification: Journal of sedimentary Research, v. 76, no. 5, p. 731-770.

Gobo, K., Ghinassi, M., and Nemec, W., 2014a, Reciprocal changes in foreset to bottomset facies in a Gilbert-type delta: response to short-term changes in base level: Journal of Sedimentary Research, v. 84, no. 11, p. 1079-1095.

Gobo, K., Ghinassi, M., and Nemec, W., 2015, Gilbert-type deltas recording short-term base-level changes: Delta-brink morphodynamics and related foreset facies: Sedimentology, v. 62, no. 7, p. 1923-1949.

Gobo, K., Ghinassi, M., Nemec, W., and Sjursen, E., 2014b, Development of an incised valley-fill at an evolving rift margin: Pleistocene eustasy and tectonics on the southern side of the Gulf of Corinth, Greece: Sedimentology, v. 61, no. 4, p. 1086-1119.

Grundvåg, S. A., Johannessen, E. P., Helland-Hansen, W., and Plink-Björklund, P., 2014, Depositional architecture and evolution of progradationally stacked lobe complexes in the Eocene Central Basin of Spitsbergen: Sedimentology, v. 61, no. 2, p. 535-569.

Hickson, T. A., and Lowe, D. R., 2002, Facies architecture of a submarine fan channel–levee complex: the Juniper Ridge Conglomerate, Coalinga, California: Sedimentology, v. 49, no. 2, p. 335-362.

Hodgetts, D., 2009, LiDAR in the environmental sciences: geological applications. In: Laser Scanning for the Environmental Sciences (Ed. by G. Heritage & A. Large), Wiley-Blackwell, Oxford p. 165–179.

Hubbard, S. M., Covault, J. A., Fildani, A., and Romans, B. W., 2014, Sediment transfer and deposition in slope channels: Deciphering the record of enigmatic deep-sea processes from outcrop: Geological Society of America Bulletin, v. 126, no. 5-6, p. 857-871.

Hubbard, S. M., Romans, B. W., and Graham, S. A., 2008, Deep-water foreland basin deposits of the Cerro Toro Formation, Magallanes basin, Chile: Architectural

elements of a sinuous basin axial channel belt: Sedimentology, v. 55, no. 5, p. 1333-1359.

Jackson, J., and McKenzie, D., 1984, Active tectonics of the Alpine—Himalayan Belt between western Turkey and Pakistan: Geophysical Journal International, v. 77, no. 1, p. 185-264.

Jackson, J., and McKenzie, D., 1988, Rates of active deformation in the Aegean Sea and surrounding regions: Basin Research, v. 1, no. 3, p. 121-128.

Janbu, N. E., Nemec, W., and Kırman, E., Özaksoy, 2007, Facies anatomy of a channelizedsand-rich turbiditic system: the Eocene Kusuri Formation in the Sinop Basin, north-central Turkey: In: Nichols, G., Paola, C., Williams, E.A. (Eds.), Sedimentary Environments, Processes and Basins e A Tribute to Peter Friend. International Association of Sedimentologists Special Publication, vol. 38, p. 457-517.

Janocko, M., and Nemec, W., 2011, The facies architecture and formation of deep-water point bars: an outcrop perspective: Sedimentology. Dissertation for the degree of philosophiae, University of Bergen, p 1-33.

Janocko, M., Nemec, W., Henriksen, S., and Warchoł, M., 2011, The diversity of deep-water sinuous channel belts and slope valley-fill complexes: Marine and Petroleum Geology, v. 41, p. 7-34.

Jobe, Z. R., Bernhardt, A., and Lowe, D. R., 2010, Facies and architectural asymmetry in a conglomerate-rich submarine channel fill, Cerro Toro Formation, Sierra del Toro, Magallanes Basin, Chile: Journal of Sedimentary Research, v. 80, no. 12, p. 1085-1108.

Jolivet, L., 2001, A comparison of geodetic and finite strain pattern in the Aegean, geodynamic implications: Earth and Planetary Science Letters, v. 187, no. 1, p. 95-104.

Jolivet, L., Brun, J.-P., Gautier, P., Lallemant, S., and Patriat, M., 1994, 3D-kinematics of extension in the Aegean region from the early Miocene to the present; insights from the ductile crust: Bulletin de la Société géologique de France, v. 165, no. 3, p. 195-209.

Jolivet, L., and Faccenna, C., 2000, Mediterranean extension and the Africa-Eurasia collision: Tectonics, v. 19, no. 6, p. 1095-1106.

Jolivet, L., Faccenna, C., Huet, B., Labrousse, L., Le Pourhiet, L., Lacombe, O., Lecomte, E., Burov, E., Denele, Y., and Brun, J.-P., 2013, Aegean tectonics: Strain localisation, slab tearing and trench retreat: Tectonophysics, v. 597, p. 1-33.

Kane, I. A., Dykstra, M. L., Kneller, B. C., Tremblay, S., and McCAFFREY, W. D., 2009, Architecture of a coarse-grained channel–levée system: the Rosario Formation, Baja California, Mexico: Sedimentology, v. 56, no. 7, p. 2207-2234.

Kane, I. A., and Hodgson, D. M., 2011, Sedimentological criteria to differentiate submarine channel levee subenvironments: exhumed examples from the Rosario Fm.(Upper Cretaceous) of Baja California, Mexico, and the Fort Brown Fm.(Permian), Karoo basin, S. Africa: Marine and Petroleum Geology, v. 28, no. 3, p. 807-823.

Kenyon, N., Amir, A., and Cramp, A., 1995, Geometry of the younger sediment bodies of the Indus Fan, Atlas of Deep Water Environments, Springer, p. 89-93.

Kneller, B., 1995, Beyond the turbidite paradigm: physical models for deposition of turbidites and their implications for reservoir prediction: Geological Society, London, Special Publications, v. 94, no. 1, p. 31-49.

Kneller, B. C., and Branney, M. J., 1995, Sustained high-density turbidity currents and the deposition of thick massive sands: Sedimentology, v. 42, no. 4, p. 607-616.

Kolla, V., 2007, A review of sinuous channel avulsion patterns in some major deep-sea fans and factors controlling them: Marine and Petroleum Geology, v. 24, no. 6, p. 450-469.

Koutsouveli, A., Mettos, A., Tsapralis, V., Tsaila-Monopoli, S., and Ioakim, C., 1989, Geological Map of Greece, scale 1: 50000, Xylokastro sheet, IGME publications, Greece.

Kranis, H., Skourtsos, E., Gawthorpe, R., Leeder, M., and Stamatakis, M., Pre-rift basement structure and syn-rift faulting at the eastern onshore Gulf of Corinth Rift, *in* Proceedings EGU General Assembly Conference Abstracts2015, Volume 17, p. 2575.

Le Pichon, X., and Angelier, J., 1979, The Hellenic arc and trench system: a key to the neotectonic evolution of the eastern Mediterranean area: Tectonophysics, v. 60, no. 1, p. 1-42.

Leeder, M., and Jackson, J., 1993, The interaction between normal faulting and drainage in active extensional basins, with examples from the western United States and central Greece: Basin research, v. 5, no. 2, p. 79-102.

Leeder, M., Mark, D., Gawthorpe, R., Kranis, H., Loveless, S., Pedentchouk, N., Skourtsos, E., Turner, J., Andrews, J., and Stamatakis, M., 2012, A "Great Deepening": chronology of rift climax, Corinth rift, Greece: Geology, v. 40, no. 11, p. 999-1002.

Lien, T., Walker, R. G., and Martinsen, O. J., 2003, Turbidites in the Upper Carboniferous Ross Formation, western Ireland: reconstruction of a channel and spillover system: Sedimentology, v. 50, no. 1, p. 113-148.

Locat, J., and Lee, H. J., 2002, Submarine landslides: advances and challenges: Canadian Geotechnical Journal, v. 39, no. 1, p. 193-212.

Lowe, D. R., 1982, Sediment gravity flows: II Depositional models with special reference to the deposits of high-density turbidity currents: Journal of Sedimentary Research, v. 52, no. 1, p. 279-297.

Macauley, R. V., and Hubbard, S. M., 2013, Slope channel sedimentary processes and stratigraphic stacking, Cretaceous Tres Pasos Formation slope system, Chilean Patagonia: Marine and Petroleum Geology, v. 41, p. 146-162.

Macdonald, H. A., Peakall, J., Wignall, P. B., and Best, J., 2011, Sedimentation in deep-sea lobe-elements: implications for the origin of thickening-upward sequences: Journal of the Geological Society, v. 168, no. 2, p. 319-332.

Mastalerz, K., 1995, Deposits of high-density turbidity currents on fan-delta slopes: an example from the upper Visean Szczawno Formation, Intrasudetic Basin, Poland: Sedimentary Geology, v. 98, no. 1, p. 121-146.

McClusky, S., Balassanian, S., Barka, A., Demir, C., Ergintav, S., Georgiev, I., Gurkan, O., Hamburger, M., Hurst, K., and Kahle, H., 2000, Global Positioning System constraints on plate kinematics and dynamics in the eastern Mediterranean and Caucasus: Journal of Geophysical Research: Solid Earth (1978–2012), v. 105, no. B3, p. 5695-5719.

McHargue, T., Pyrcz, M. J., Sullivan, M. D., Clark, J., Fildani, A., Romans, B., Covault, J., Levy, M., Posamentier, H., and Drinkwater, N., 2011, Architecture of turbidite channel systems on the continental slope: patterns and predictions: Marine and Petroleum Geology, v. 28, no. 3, p. 728-743.

McKenzie, D., 1970, Plate tectonics of the Mediterranean region: Nature, v. 226, no. 5242, p. 239-243.

McKenzie, D., 1972, Active tectonics of the Mediterranean region: Geophysical Journal International, v. 30, no. 2, p. 109-185.

McKenzie, D., 1978, Active tectonics of the Alpine—Himalayan belt: the Aegean Sea and surrounding regions: Geophysical Journal International, v. 55, no. 1, p. 217-254.

McNeill, L., and Collier, R. L., 2004, Uplift and slip rates of the eastern Eliki fault segment, Gulf of Corinth, Greece, inferred from Holocene and Pleistocene terraces: Journal of the Geological Society, v. 161, no. 1, p. 81-92.

McNeill, L., Cotterill, C., Henstock, T., Bull, J., Stefatos, A., Collier, R. L., Papatheoderou, G., Ferentinos, G., and Hicks, S., 2005, Active faulting within the offshore western Gulf of Corinth, Greece: implications for models of continental rift deformation: Geology, v. 33, no. 4, p. 241-244.

Miall, A. D., 1985, Architectural-element analysis: a new method of facies analysis applied to fluvial deposits. Earth-Science Reviews 22, 261-308.

Moretti, I., Lykousis, V., Sakellariou, D., Reynaud, J.-Y., Benziane, B., and Prinzhoffer, A., 2004, Sedimentation and subsidence rate in the Gulf of Corinth: what we learn from the Marion Dufresne's long-piston coring: Comptes Rendus Geoscience, v. 336, no. 4, p. 291-299.

Moretti, I., Sakellariou, D., Lykousis, V., and Micarelli, L., 2003, The Gulf of Corinth: an active half graben?: Journal of Geodynamics, v. 36, no. 1, p. 323-340.

Moxham, R. M., and Eckhart, R. A., 1956, Marl deposits in the Knik Arm area, Alaska. Geology, p. 1-23.

Mutti, E., 1977, Distinctive thin-bedded turbidite facies and related depositional environments in the Eocene Hecho Group (south-central Pyrenees, Spain): Sedimentology, v. 24, no. 1, p. 107-131.

Mutti, E., and Normark, W. R., 1987, Comparing examples of modern and ancient turbidite systems: problems and concepts, Marine clastic sedimentology, Springer, p. 1-38.

Mutti, E., Tinterri, B., Remacha, E., Mavilla, N., Angella, S., and Fava, L., 1999, An Introduction to the Analysis of Ancient Turbidite Basins from an Outdrop perspective. AAPG Continuing Course Note Series, 39, 96-pp.

Nemec, W., 1988, The shape of the rose: Sedimentary Geology, v. 59, no. 1-2, p. 149-152.

Nemec, W., 1990, Aspects of sediment movement on steep delta slopes: Coarse-grained deltas, v. 10, p. 29-73.

Nemec, W., 1995, The dynamics of deltaic suspension plumes: Geology of deltas, p. 31-93.

Nemec, W., 2005, Geostatistics: Course GEOV301 Lecture Notes: University of Bergen.

Nichols, G., 2009, Sedimentology and stratigraphy, John Wiley & Sons. p. 419.

O'Byrne, C., Prather, B., Sylvester, Z., Pirmez, C., Couzens, B., Smith, R., Barton, M., Steffens, G., and Willson, J., 2007, Architecture of a Deep-water Levee Avulsion, Silla Ojo Mesa, Parque Nacional Torres del Paine, Chile: Deep-water Outcrops of the World Atlas: AAPG, Studies in Geology, v. 56, p. 143-147.

Ori, G. G., 1989, Geologic history of the extensional basin of the Gulf of Corinth (? Miocene-Pleistocene), Greece: Geology, v. 17, no. 10, p. 918-921.

Pickering, K., Clark, J., Smith, R., Hiscott, R., Lucchi, F. R., and Kenyon, N., 1995, Architectural element analysis of turbidite systems, and selected topical problems for sand-prone deep-water systems, Atlas of deep water environments, Springer, p. 1-10.

Pickering, K., and Hiscott, R., 2015, Deep Marine Systems: Processes, Deposits, Environments, Tectonics and Sedimentation. American Geophysical Union, Wiley, p. 698.

Pickering, K., Stow, D., Watson, M., and Hiscott, R., 1986, Deep-water facies, processes and models: a review and classification scheme for modern and ancient sediments: Earth-Science Reviews, v. 23, no. 2, p. 75-174.

Posamentier, H. W., and Kolla, V., 2003, Seismic geomorphology and stratigraphy of depositional elements in deep-water settings: Journal of Sedimentary Research, v. 73, no. 3, p. 367-388.

Postma, G., 1984, Slumps and their deposits in fan delta front and slope: Geology, v. 12, no. 1, p. 27-30.

Postma, G., and Roep, T. B., 1985, Resedimented conglomerates in the bottomsets of Gilbert-type gravel deltas: Journal of Sedimentary Research, v. 55, no. 6.

Potter, P. E., 1967, Sand bodies and sedimentary environments: a review: AAPG Bulletin, v. 51, no. 3, p. 337-365.

Poulimenos, G., Zelilidis, A., Kontopoulos, N., and Doutsos, T., 1993, Geometry of trapezoidal fan deltas and their relationship to extensional faulting along the southwestern active margins of the Corinth rift, Greece: Basin research, v. 5, no. 3, p. 179-192.

Prèlat, A., Hodgson, D., and Flint, S., 2009, Evolution, architecture and hierarchy of distributary deep-water deposits: a high-resolution outcrop investigation from the Permian Karoo Basin, South Africa: Sedimentology, v. 56, no. 7, p. 2132-2154.

Prélat, A., and Hodgson, D. M., 2013, The full range of turbidite bed thickness patterns in submarine lobes: controls and implications: Journal of the Geological Society, v. 170, no. 1, p. 209-214.

Rarity, F., Van Lanen, X., Hodgetts, D., Gawthorpe, R., Wilson, P., Fabuel-Perez, I., and Redfern, J., 2014, LiDAR-based digital outcrops for sedimentological analysis: workflows and techniques: Geological Society, London, Special Publications, v. 387, no. 1, p. 153-183.

Reineck, H.-E., and Singh, I. B., 1980, Scour marks, Depositional Sedimentary Environments, Springer, p. 73-77.

Rohais, S., Eschard, R., Ford, M., Guillocheau, F., and Moretti, I., 2007a, Stratigraphic architecture of the Plio-Pleistocene infill of the Corinth Rift: implications for its structural evolution: Tectonophysics, v. 440, no. 1, p. 5-28.

Rohais, S., Eschard, R., and Guillocheau, F., 2008, Depositional model and stratigraphic architecture of rift climax Gilbert-type fan deltas (Gulf of Corinth, Greece): Sedimentary Geology, v. 210, no. 3, p. 132-145.

Rohais, S., Joannin, S., Colin, J.-P., Suc, J.-P., Guillocheau, F., and Eschard, R., 2007b, Age and environmental evolution of the syn-rift fill of the southern coast of the Gulf of Corinth (Akrata-Derveni region, Greece): Bulletin de la Société géologique de France, v. 178, no. 3, p. 231-243.

Sachpazi, M., Clément, C., Laigle, M., Hirn, A., and Roussos, N., 2003, Rift structure, evolution, and earthquakes in the Gulf of Corinth, from reflection seismic images: Earth and Planetary Science Letters, v. 216, no. 3, p. 243-257.

Skourlis, K., and Doutsos, T., 2003, The Pindos Fold-and-thrust belt (Greece): inversion kinematics of a passive continental margin: International Journal of Earth Sciences, v. 92, no. 6, p. 891-903.

Skourtsos, E., and Kranis, H., 2009, Structure and evolution of the western Corinth Rift, through new field data from the Northern Peloponnesus: Geological Society, London, Special Publications, v. 321, no. 1, p. 119-138.

Stefatos, A., Papatheodorou, G., Ferentinos, G., Leeder, M., and Collier, R., 2002, Seismic reflection imaging of active offshore faults in the Gulf of Corinth: their seismotectonic significance: Basin Research, v. 14, no. 4, p. 487-502.

Stow, D. A. V., Howell, D. G., and Nelson, C. H., 1985, Sedimentary, tectonic, and sea-level controls, Submarine fans and related turbidite systems, Springer, p. 15-22.

Stow, D. A. V., Reading, H. G., and Collinson, J. D., 1996, Sedimentary environments: processes, facies and stratigraphy; Deep seas, p. 395-453, Oxford, Blackwell Publishing.

Talling, P. J., 1998, How and where do incised valleys form if sea level remains above the shelf edge?: Geology, v. 26, no. 1, p. 87-90.

Talling, P. J., Masson, D. G., Sumner, E. J., and Malgesini, G., 2012, Subaqueous sediment density flows: depositional processes and deposit types: Sedimentology, v. 59, no. 7, p. 1937-2003.

Taylor, B., Weiss, J. R., Goodliffe, A. M., Sachpazi, M., Laigle, M., and Hirn, A., 2011, The structures, stratigraphy and evolution of the Gulf of Corinth rift, Greece: Geophysical Journal International, v. 185, no. 3, p. 1189-1219.

Trotet, F., Goffe, B., Vidal, O., and Jolivet, L., 2006, Evidence of retrograde Mg-carpholite in the Phyllite-Quartzite nappe of Peloponnese from thermobarometric modelisation-geodynamic implications: Geodinamica Acta, v. 19, no. 5, p. 323-343.

Veiga, G. D., Spalletti, L. A., and Flint, S. S., 2009, Anatomy of a fluvial lowstand wedge: the Avilé Member of the Agrio Formation (Hauterivian) in central Neuquén Basin (northwest Neuquén Province), Argentina: Sedimentary Processes, Environments and Basins: A Tribute to Peter Friend (Special Publication 38 of the IAS), v. 22, p. 341.

Walker, R. G., 1975, Generalized facies models for resedimented conglomerates of turbidite association: Geological Society of America Bulletin, v. 86, no. 6, p. 737-748.

Weimer, P., and Slatt, R. M., 2004, Petroleum systems of deepwater settings, p. 470.

Wynn, R. B., Kenyon, N. H., Masson, D. G., Stow, D. A., and Weaver, P. P., 2002, Characterization and recognition of deep-water channel-lobe transition zones: AAPG bulletin, v. 86, no. 8.

Zelt, F., and Rossen, C., 1995, Geometry and continuity of deep-water sandstones and siltstones, Brushy Canyon Formation (Permian) Delaware Mountains, Texas, Atlas of Deep Water Environments, Springer, p. 167-183.

APPENDIX

Lithological logs, Western Sythas Valley

Logs are presented in a 1:75 scale. Height is presented in metres above sea level.

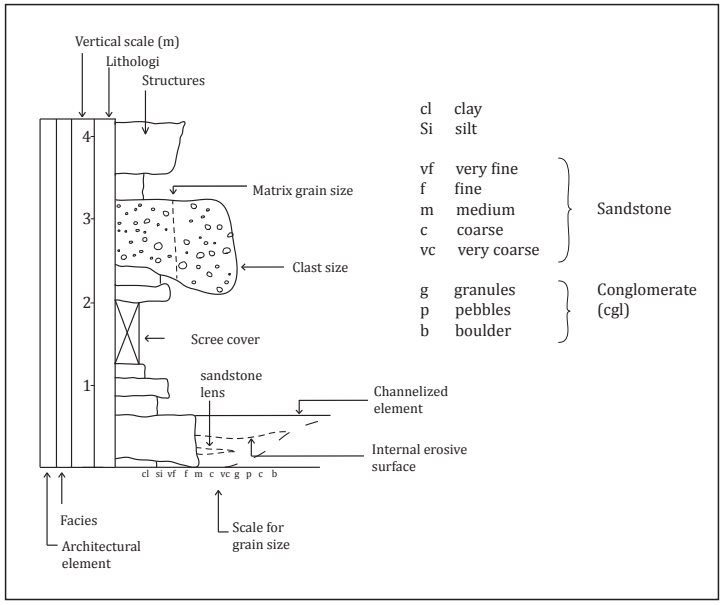

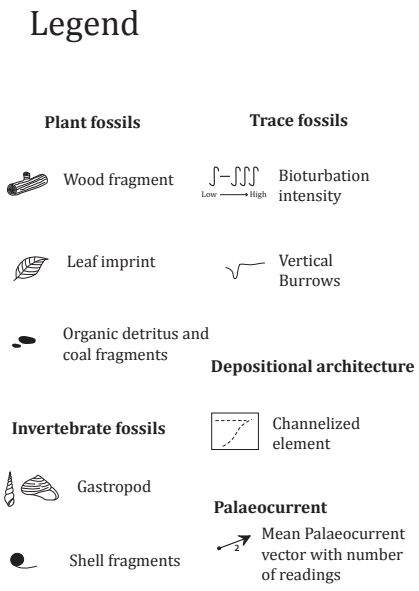

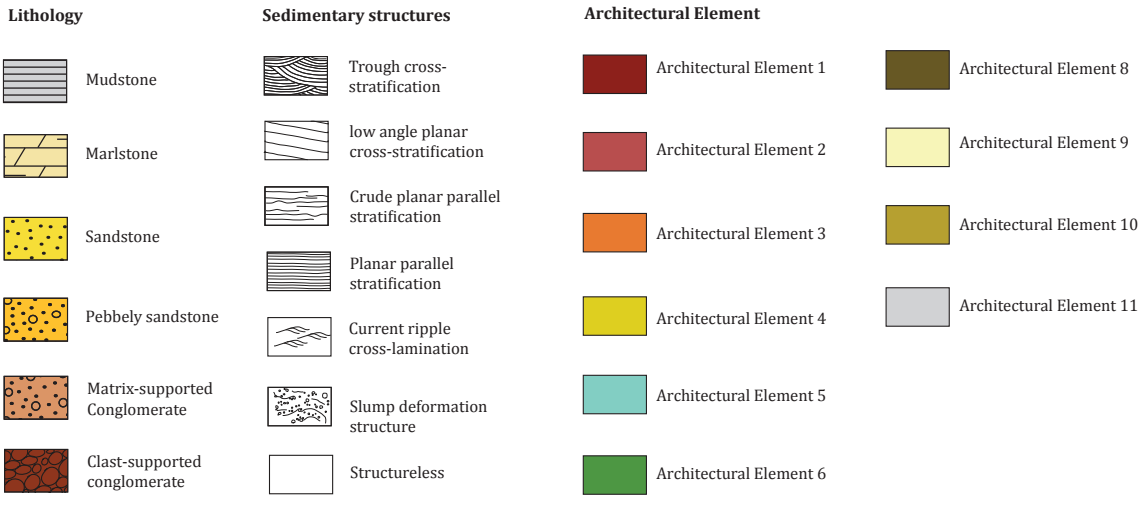

Log 1

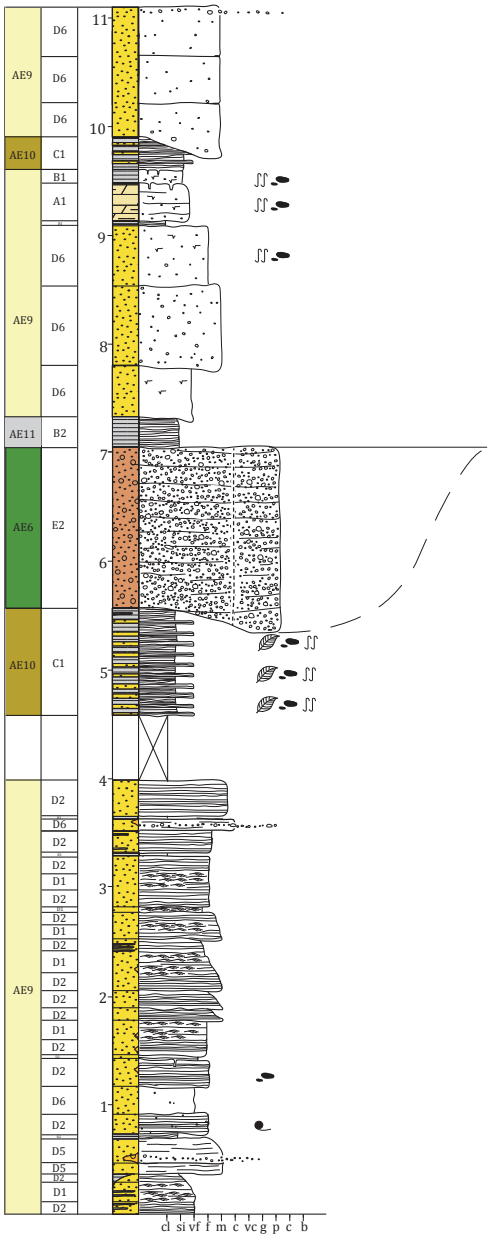

UTM Coordinates: 34S 637106.86 m E
4210344.61 m N

Metres above sea level: 227

Total logged metres: 11.10

Log 2

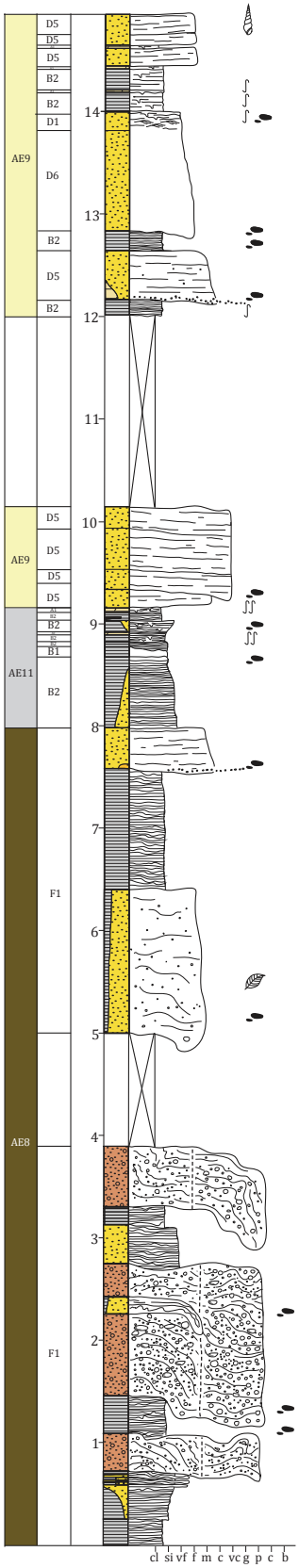

UTM Coordinates: 34S 637364.60 m E
4210866.61 m N

Metres above sea level: 247

Total logged metres: 14.90

Log 3

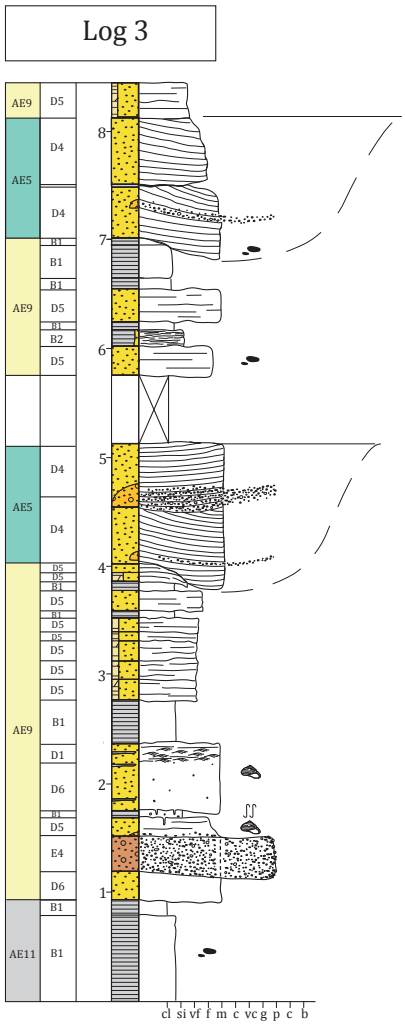

UTM Coordinates: 34S 637358.27 m E
4210940.83 m E

Metres above sea level: 265

Total logged metres: 8.40

Log 4

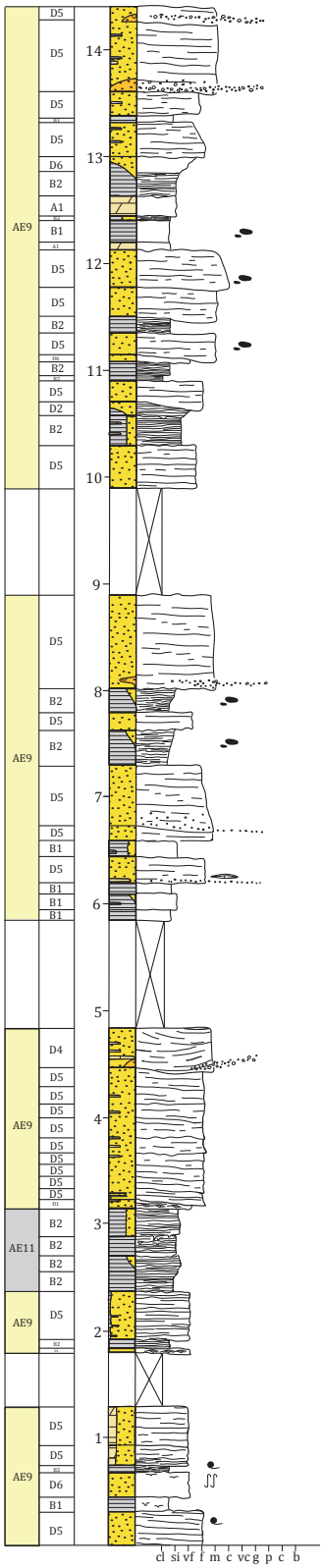

UTM Coordinates: 34S 637283.70 m E
4210855.91 m N

Metres above sea level: 286

Total logged metres: 14.40

Log 5

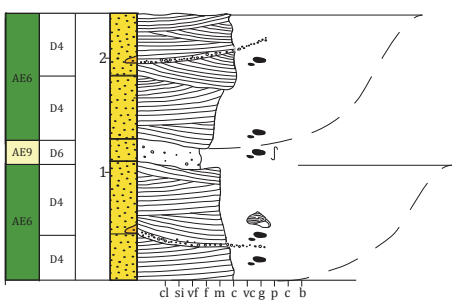

UTM Coordinates: 34S 637218.26 m E
4210602.28 m N

Metres above sea level: 289

Total logged metres: 2.40

Log 6

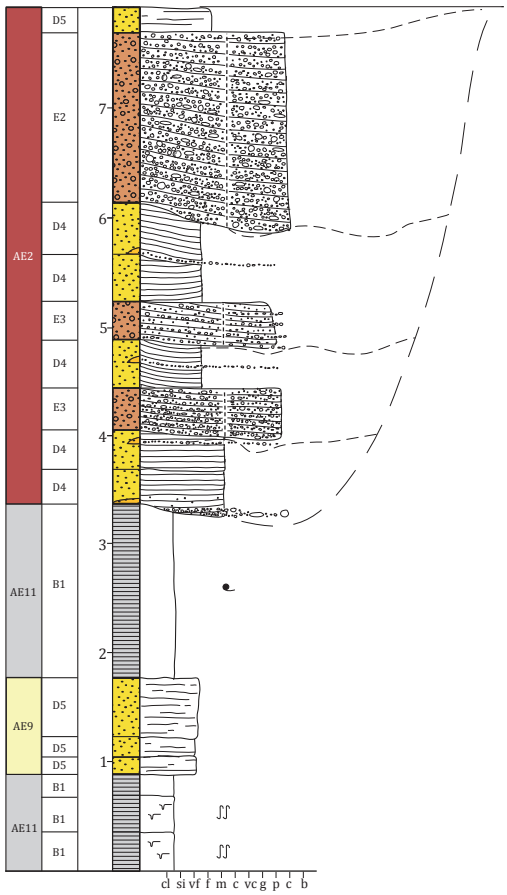

UTM Coordinates: 34S 637211.24 m E
4210611.54 m N

Metres above sea level: 294

Total logged metres: 7.90

Log 8

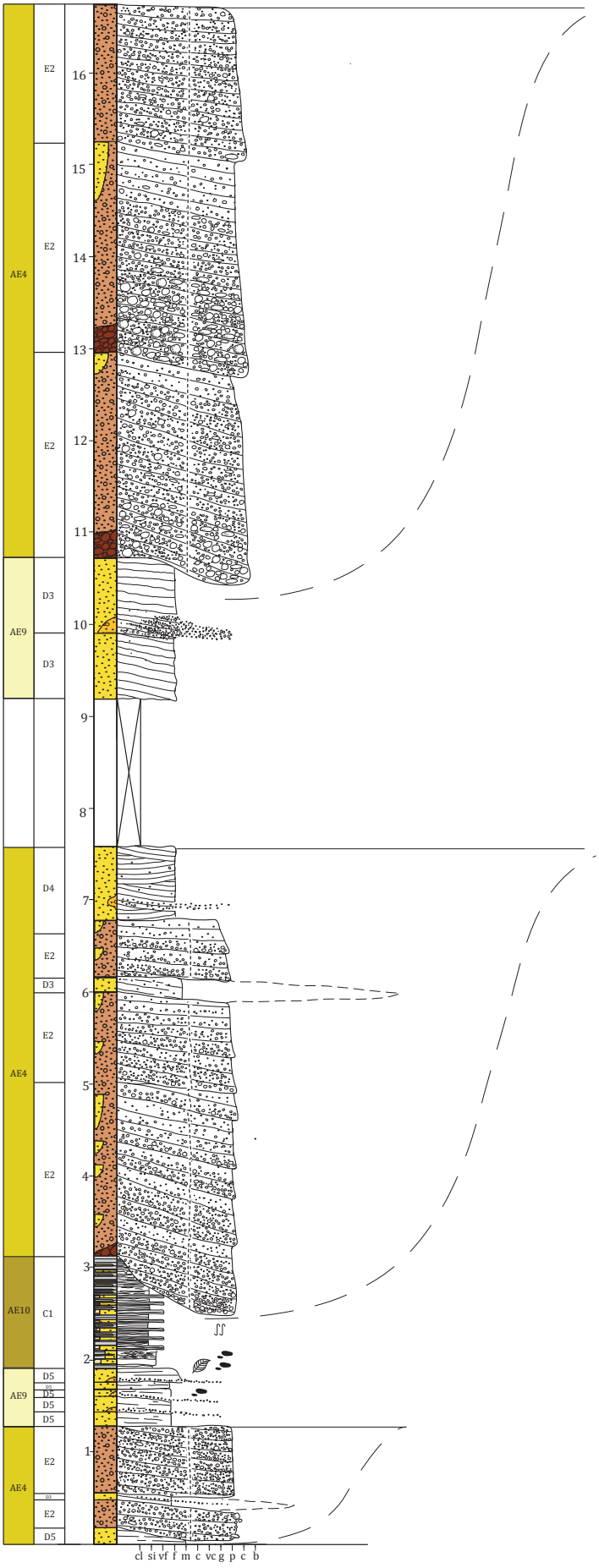

UTM Coordinates: 34S 637169.97 m E
4210659.44 m N

Metres above sea level: 336

Total logged metres: 16.70

Log 7

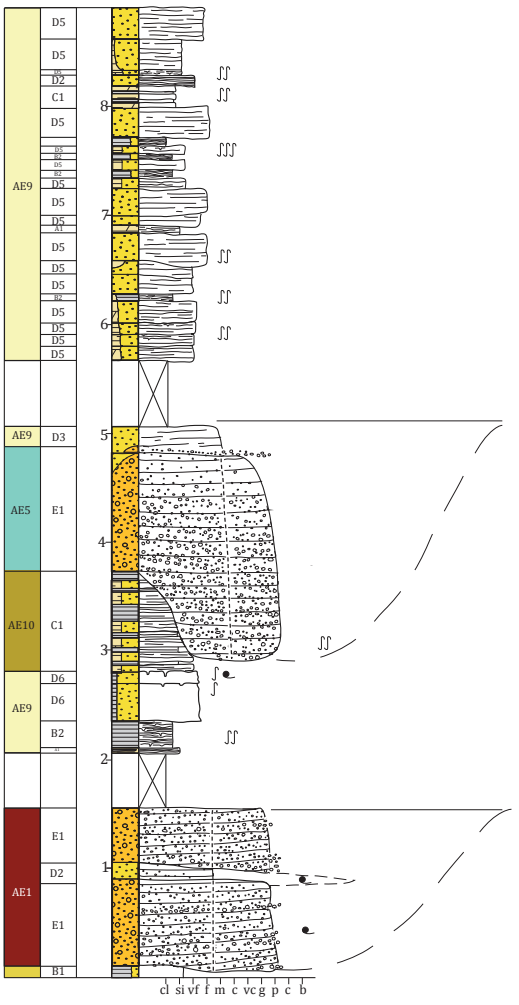

UTM Coordinates: 34S 637191.61 m E
4210663.23 m N

Metres above sea level: 329

Total logged metres: 8.90

Log 9

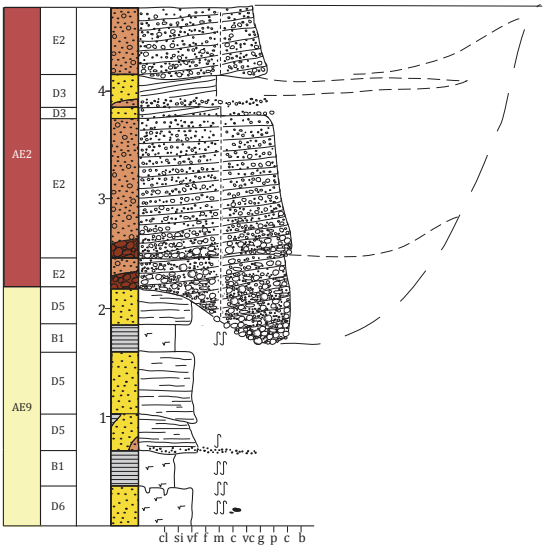

UTM Coordinates: 34S 636977.94 m E
4210598.26 m N

Metres above sea level: 338

Total logged metres: 4.80

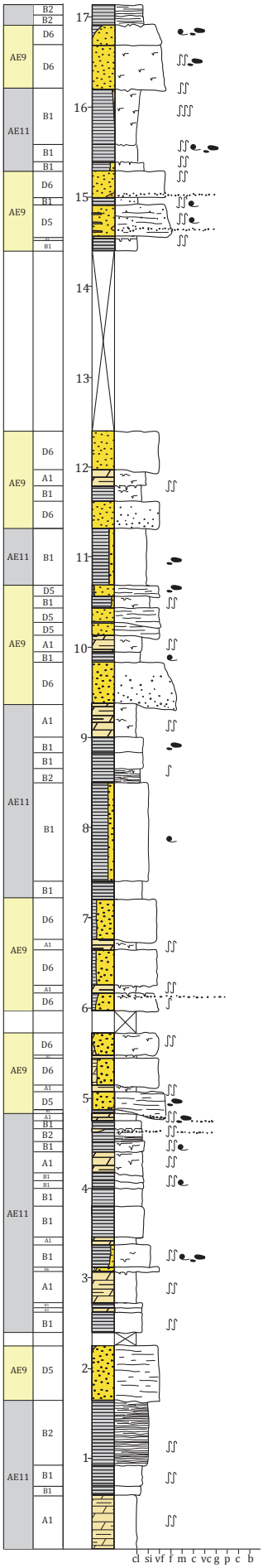

UTM Coordinates: 34S 636945,24 m E
4210636,45 m E

Metres above sea level: 356

Total logged meters: 23.30

Log 10

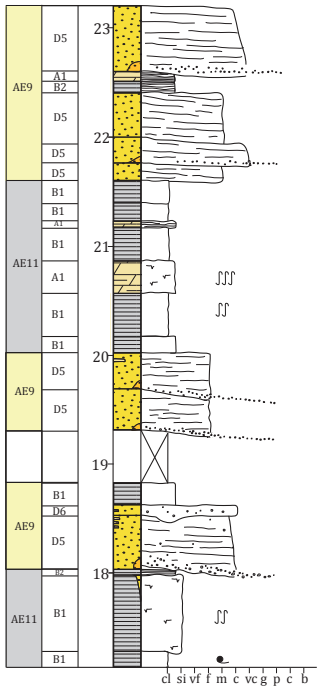

Log 11

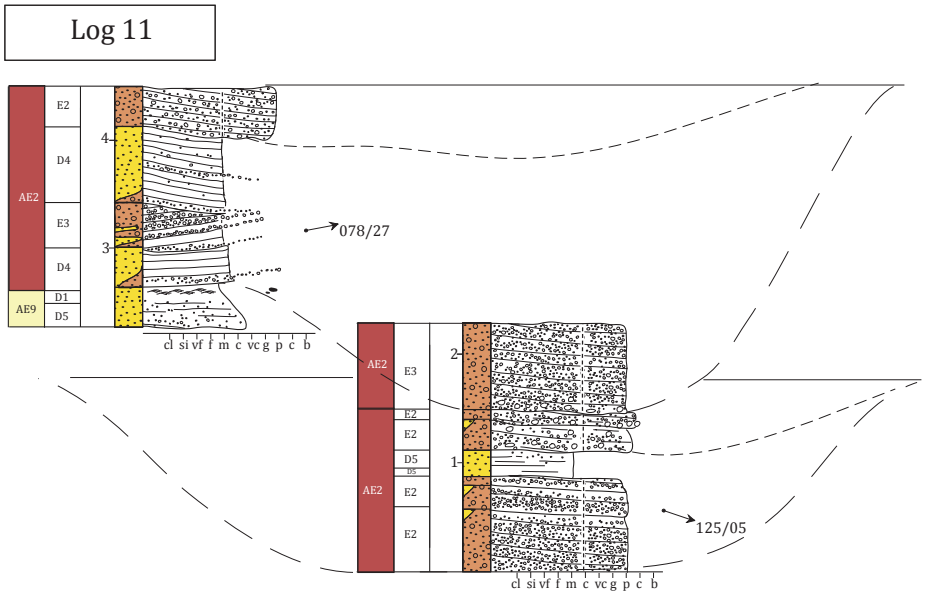

UTM Coordinates:	34S 636950.17 m E 4210639.31 m N
Metres above sea level:	358
Total logged metres:	4.50

Log 12

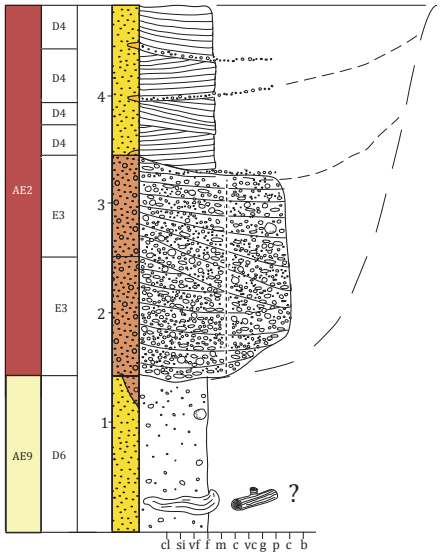

UTM Coordinates:	34S 637073.62 m E 4210872.66 m N
Metres above sea level:	386
Total logged metres:	4.90

Log 13

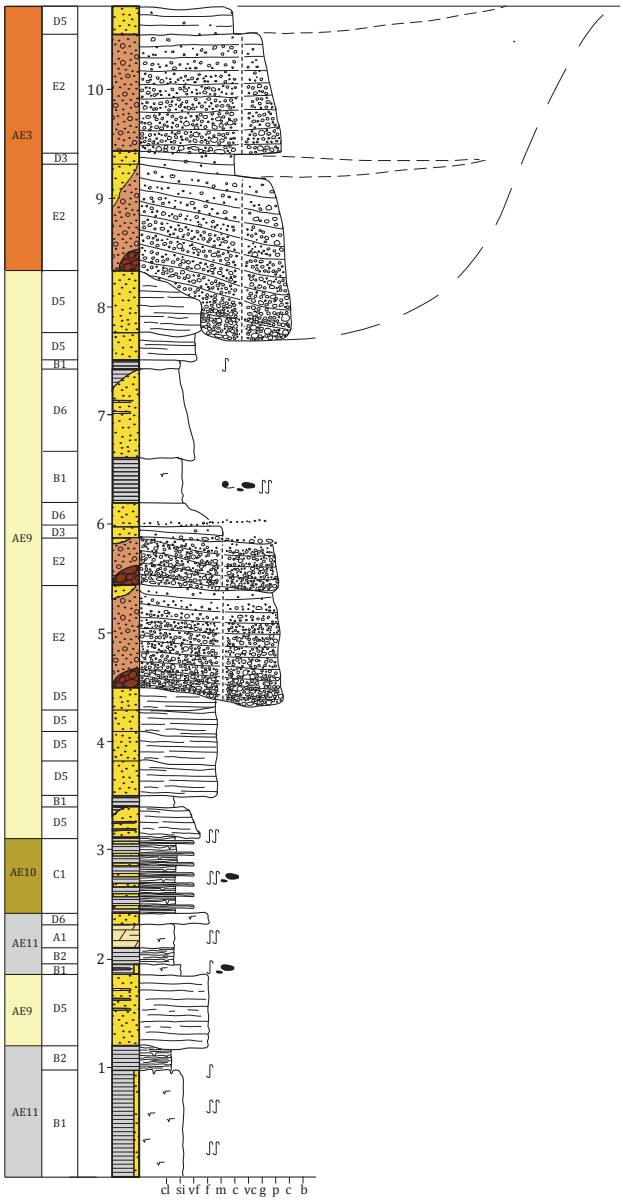

UTM Coordinates: 34S 636677.77 m E
4210672.26 m N

Metres above sea level: 380

Total logged metres: 10.80

Log 14

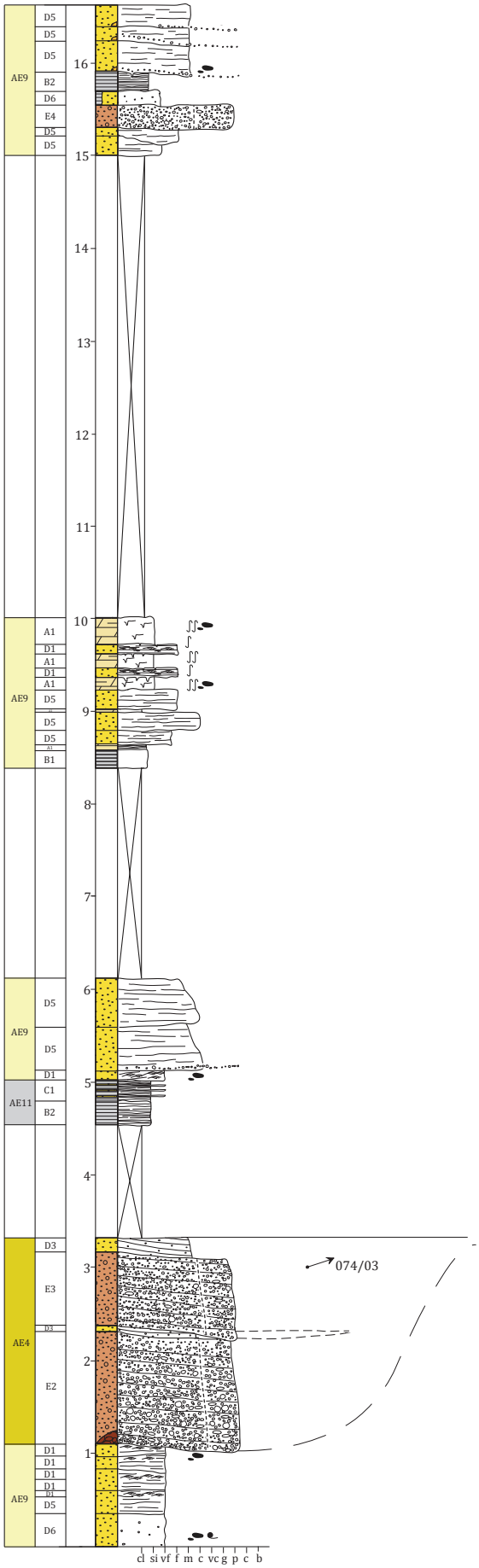

UTM Coordinates: 34S 636941.63 m E
4210703.63 m N

Metres above sea level: 382

Total logged metres: 16.60

Log 15

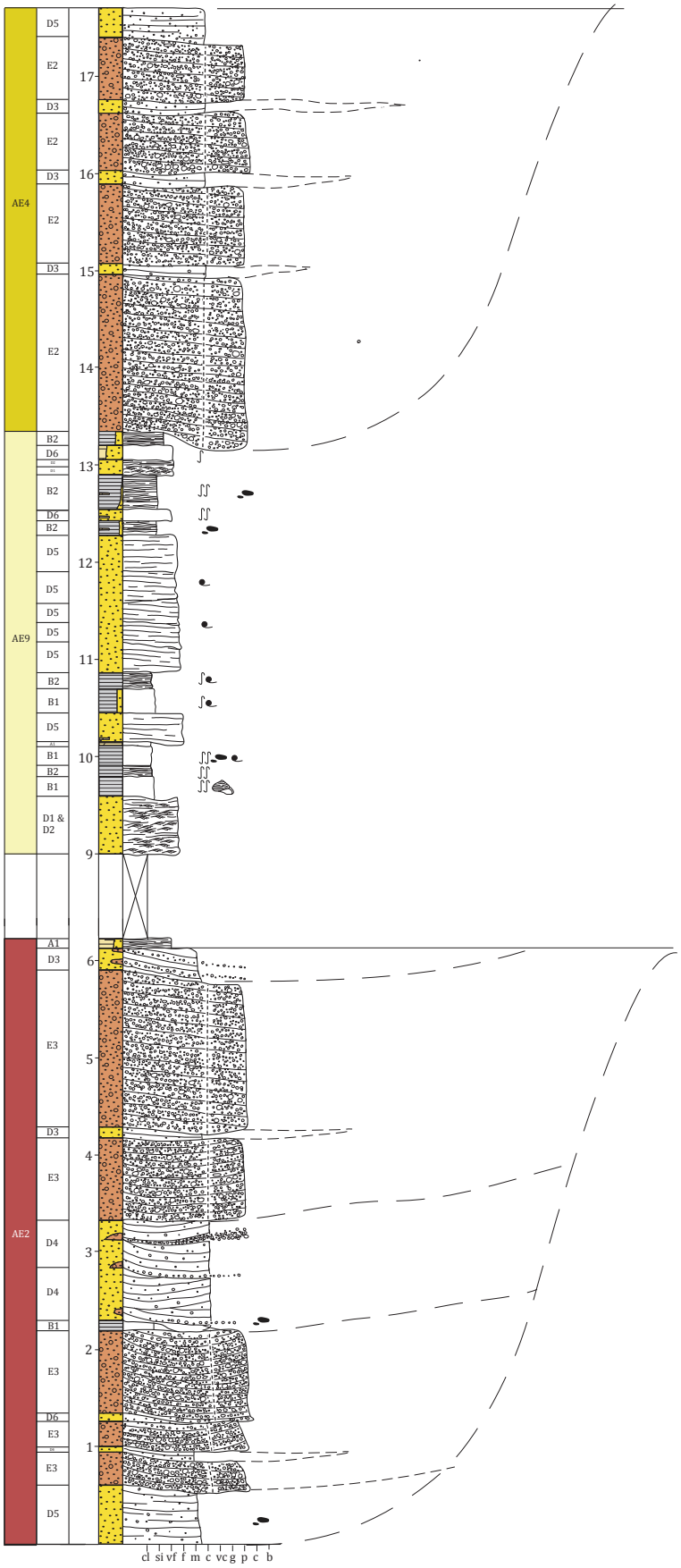

UTM Coordinates: 34S 636871.23 m E
4210761.52 m N

Metres above sea level: 410

Total logged metres: 17.80

Log 16

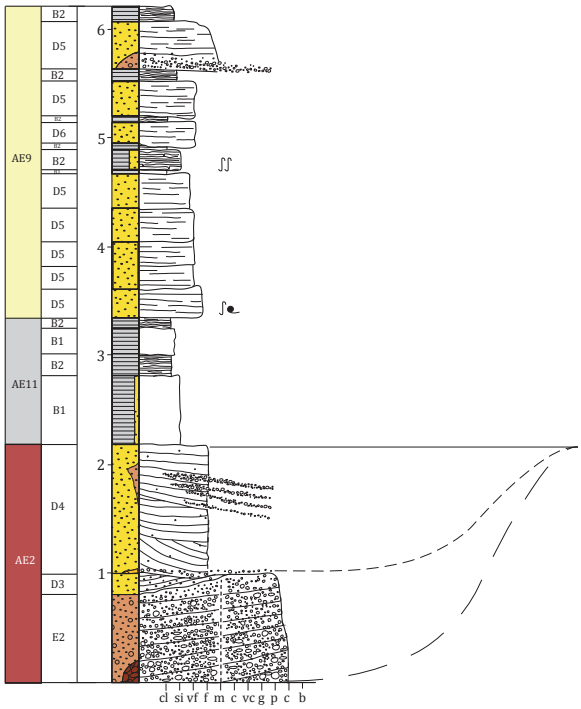

UTM Coordinates: 34S 636719.23 m E
4210739.50 m N

Metres above sea level: 425

Total logged metres: 6.20

Log 17

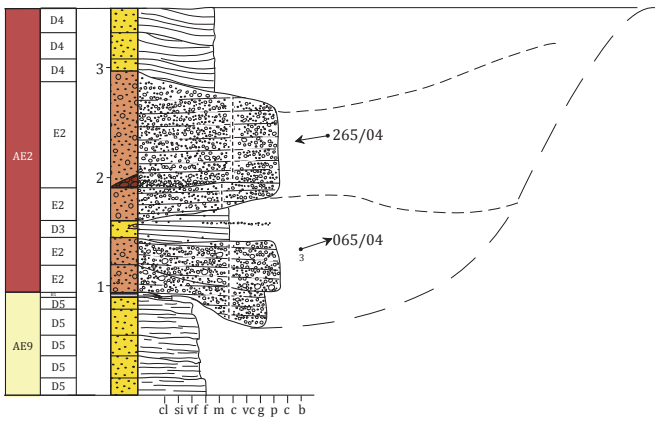

UTM Coordinates: 34S 636796.40 m E
4210778.36 m N

Metres above sea level: 431

Total logged metres: 3.50

Log 18

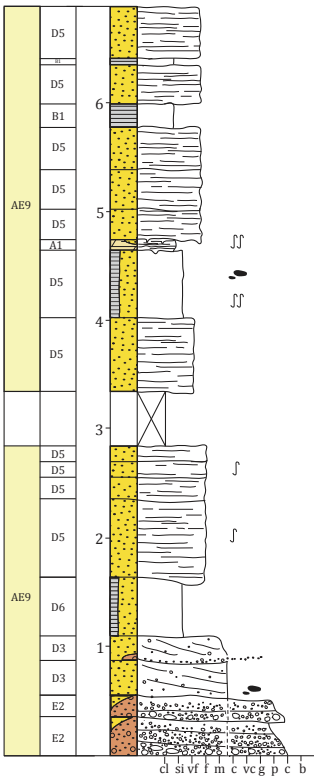

UTM Coordinates: 34S 636831.27 m E
4210798.98 m N

Metres above sea level: 437

Total logged metres: 6.90

Log 19

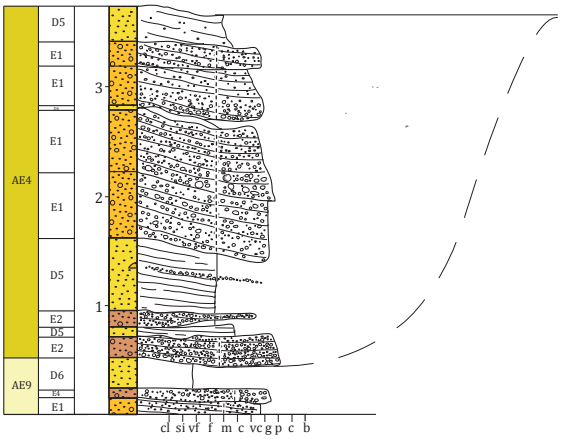

UTM Coordinates: 34S 637169.92 m E
4211226.80 m N

Metres above sea level: 392

Total logged metres: 3.80

Log 20

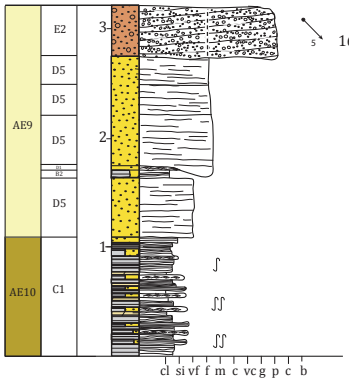

UTM Coordinates: 34S 636794.49 m E
4211072.28 m N

Metres above sea level: 519

Total logged metres: 3.20

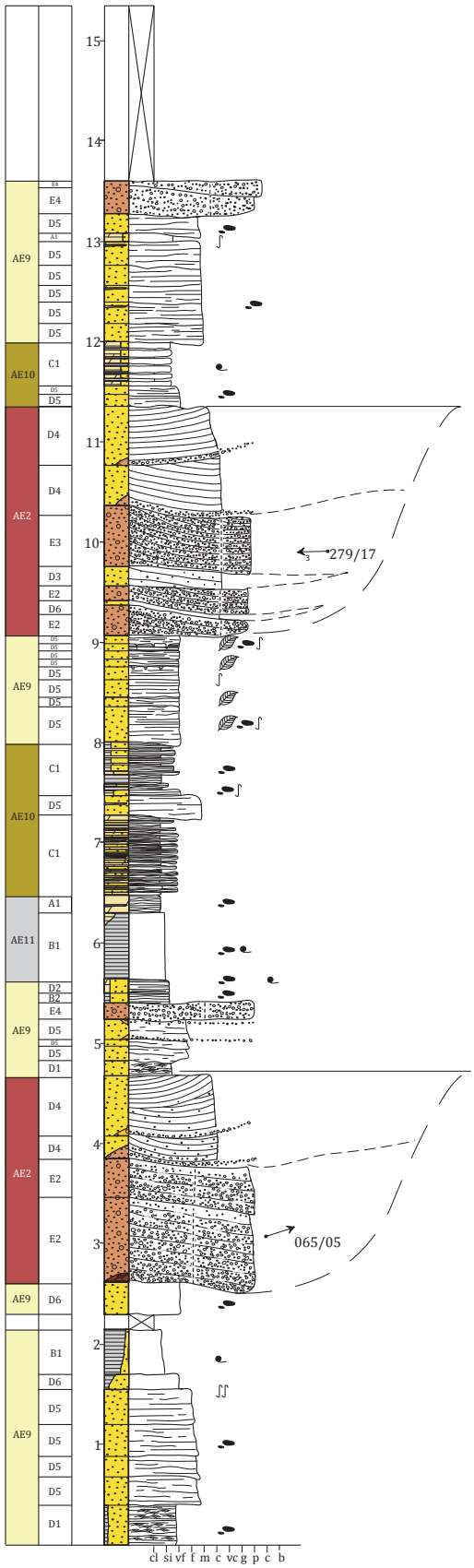

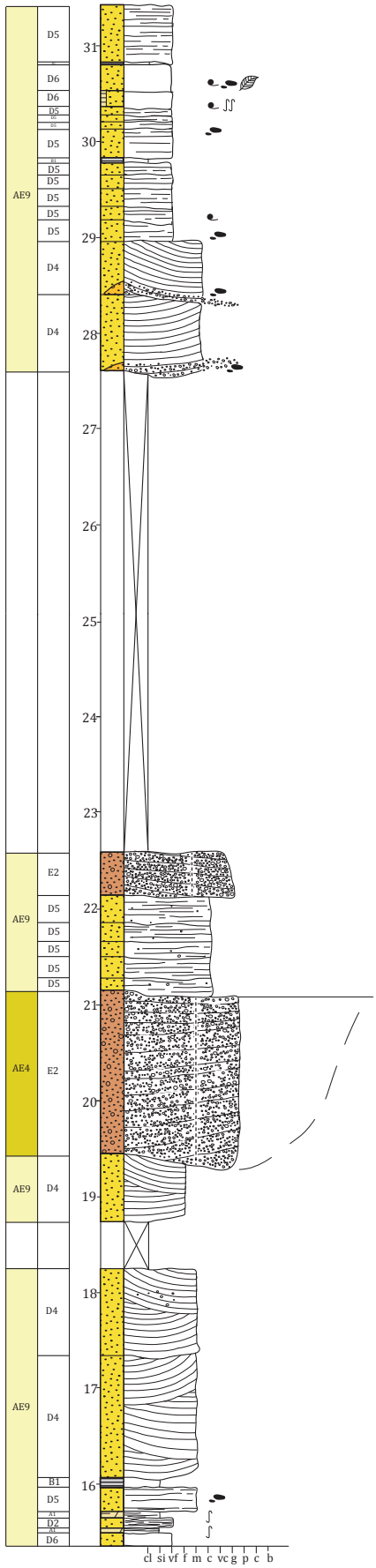

Log 21

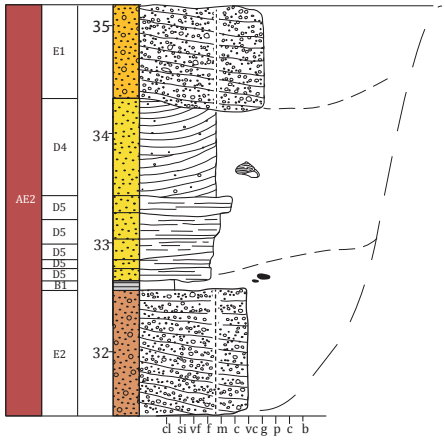

UTM Coordinates:	34S 636393.48 m E 4210781.47 m N
Metres above sea level:	528
Total logged metres:	35.20